NORTHWESTERN UNIVERSITY

A Coordination Chemistry Approach to Nano- and Supramolecular Material Design

A DISSERTATION

SUBMITTED TO THE GRADUATE SCHOOL

IN PARTIAL FULFILLMENT OF THE REQUIREMENTS

for the degree

DOCTOR OF PHILOSOPHY

Field of Chemistry

By

Benjamin Douglas Coleman

EVANSTON, ILLINOIS

September 2023

ABSTRACT

A Coordination Chemistry Approach to Nano- and Supramolecular Material Design

Benjamin Douglas Coleman

The need for complex and sophisticated materials continues to grow as society becomes more advanced. For many chemists, the design of these materials begins by looking towards model molecular systems for the identification of desirable properties and functions. As such, restricting oneself to C, H, N, O, and the other few elements of organic chemistry is inherently limiting to the types of materials that can be achieved. Coordination and organometallic chemistry takes advantage of nearly the entirety of the Periodic Table (e.g. transition metals, lanthanides, actinides, nonmetals) to form compounds with a wide variety of electronic, chemical, and physical properties. As such, coordination chemistry is an ideal platform for the bottom-up construction of next-generation nano- and supramolecular materials. This dissertation uses coordination chemistry to synthesize novel magnetic and stimuli-responsive materials, with a focus on the construction of new infinite coordination polymers.

Chapter 1 begins this work with a brief introduction to the core theory behind infinite coordination polymers, transition metal-based metal-organic magnets, and the dynamic Weak-Link Approach (WLA) to supramolecular chemistry. Chapter 2 describes the synthesis and characterization of a series of metal-organic framework magnets. These materials leverage antiferromagnetic coupling between unpaired electrons on transition metal centers and radical ligand-based electrons to engender strong magnetic coupling, leading to higher magnetic ordering temperatures in the subsequent materials. Chapters 3 and 4 of this dissertation explore the WLA for the design of stimuli-responsive coordination polymers and molecular tweezers. The WLA

leverages the well-developed coordination chemistry of d^8 transition metal ions with hemilabile ligands to construct nanoscale architectures that can be switched between a closed, structurally rigid state and more open, flexible state. In Chapter 3, the design and synthesis of the first series of crystalline, WLA-based coordination polymers is reported. Notably, by studying the response of one of the chains to Cl^- anions in solution, we demonstrate that crystalline chain assembly can be controlled via the structural state of imbedded WLA complex subunits. Next, we focus on further developing the chemistry at the core of the WLA and expanding it to include reversible structural switching in an aqueous environment; chapter 4 details initial attempts and challenges in understanding the chemistry of newly synthesized water-soluble WLA complexes. We see adapting the WLA to function within water as the first steps to integrating the WLA with biomacromolecules for the synthesis of novel dynamic, biomaterials. Finally, in chapter 6, future work to further build the WLA towards a platform that can be used to design dynamic inorganic and biomacromolecular materials at increasing length scales and complexity is detailed.

Thesis Advisor: Prof. Chad A. Mirkin

ACKNOWLEDGMENTS

"No man is an island entire of itself; every man is a piece of the continent, a part of the main …"

- John Donne

I have been fortunate that my work and my life has been filled with wonderful people that shaped the person I am today and the work I have accomplished. I thank my family for all the love and support they have given me throughout my life. To my brother, Josh Coleman, I thank you for your patience and your support. You were my first role model and will always be my big brother. To my sister, Sara Bryanne Coleman, I wish you could be here to see this work, to laugh and joke with me, and to get me into trouble. I know you would be proud, and I know you would be smiling. To my father, Tim Coleman, you promised me that you would be here when I finished this journey. I know you will be, and I know you would be proud. I think of you often. I miss you. To my mother, Theresa Coleman, words cannot express how much your love and support has meant to me. I would not be here without you. You gave me my moral compass, taught me the importance of kindness, and were there to pick me up when I fell. I am proud to be your son.

I thank my advisor, Professor Chad Mirkin. I do not know where I would be without your mentorship, but I do know this dissertation would not have been finished. You were there to support me during the hardest moment of my Ph.D. candidacy. You taught me much during my time in your research group, and I know it has made me a better scientist and professional. Like the best mentors, you knew when to push hard and when to provide a gentle nudge. Thank you for all the opportunities you gave me.

I thank my committee members, Prof. Mercouri Kanatzidis and Prof. Brian Hoffman, for their helpful feedback and discussion throughout my Ph.D. I also thank my undergraduate advisor, Prof. Michael Castellani. You saw my potential and believed in me. Your lab is where I learned to love chemistry and research.

I thank my friend and mentor, Dr. Ho Fung (Edmund) Cheng, for your patience and guidance. You taught me how to ask questions and chase answers. I learned how to be a successful graduate student from you, and I cannot wait to see the next steps in your journey. I would also like to thank my coauthors Dr. Andrea D'Aquino, Dr. Zachary Kean, Charlotte Stern, and Dr. Jenny Orbeck for all your contributions to the work reported herein. I thank Dr. Peter Smith, Prof. Benjamin Partridge, Prof. Yuwei Gu, Dr. Agnes Thorarinsdottir, Dr. David Zee, Dr. Chris Malliakas, and Dr. Yongbo Zhang for all our helpful conversations and discussions. Your feedback helped me see problems from new directions. I would also like to thank the Supramolecular Synthesis subgroup in the Mirkin group. It was a privilege to serve as your subgroup leader, and I will miss the scientific discussions that occurred during our meetings.

Some of the most rewarding experiences I had during my Ph.D. occurred while mentoring young students and junior colleagues, whether formally or informally. I would like to thank Adam Claman and Jenny Delgado for allowing me to be a part of your academic journey. I would also like to thank Yihan (Fiona) Wang. I no longer think of you as my mentee, but as my partner and collaborator. It has been humbling to see how much you have grown over the last several years, and I am proud to have been a small part of your story. I know you are going to have a wonderful career and impact on the world.

Finally, I thank my friends and colleagues Michael Evangelopoulos, Dr. Sergej Kudruk, Dr. Max Distler, Jungsoo Park, and Vinzenz Mayer and my friend and fellow comic book fan

Stewart Quarles. You were there to hear about my struggles, to give me advice, and to make me laugh. You made Chicago a home for me. I thank my companion and best cat friend, Gandalf. You were there as my cuddle partner, game partner, reading partner, stress partner, and as an endless source of happiness. I am glad you have been here through it all.

In sum, the following dissertation and my achievements would not be possible without the love, guidance, mentorship, collaboration, and friendship of so many people in my life. I am who I am because of our experiences together, and to all of you, I am eternally grateful.

For Bryanne. For Dad.

TABLE OF CONTENTS

LIST OF TABLES AND FIGURES

Chapter 1

Introduction

From the strength of vulcanized rubber to allosteric regulation in proteins to organic light-emitting diode (OLED) screens, molecular and electronic structure significantly impacts material properties. Indeed, structure/function relationship investigations are a key facet of modern chemical, supramolecular, and nanomaterial research. It's not surprising then that chemists and material scientists often turn towards a bottom-up approach, in which molecular subunits with desired properties are built upon to form a larger system, in the design of new functional materials. Excitingly, this increase in scale can lead to emergent properties in the newly synthesized materials. Coordination and organometallic chemistry are ideal platforms for the bottom-up design of next-generation supramolecular and nanomaterials as the subfields take advantage of the deserve chemical reactivity of elements spanning almost the entirety of the Periodic Table (e.g. transition metals, lanthanides, actinides, metalloids, nonmetals), and coordination complexes and their materials have been shown to display a wide variety of functions and properties. The work described herein employs coordination and organometallic chemistry for the design of novel higher-order materials, with an emphasis on the design of infinite coordination polymers (Chapters 2 and 3) and steps toward dynamic molecular tweezers that operate in water (Chapter 4).

As infinite coordination polymers (ICPs) are the basis of two of the chapters in this dissertation, we shall begin by providing a brief overview of their construction before continuing towards background on the dissertation topics. ICPs are a class of nanomaterials in which multidentate organic ligands are linked together through metal ions or clusters to form 1D, 2D, or 3D architectures, with the 3D congeners more commonly referred to as metal-organic frameworks (MOFs) (**Figure 1.1**).[1-4] ICPs have a high degree of tunability and can be rationally designed

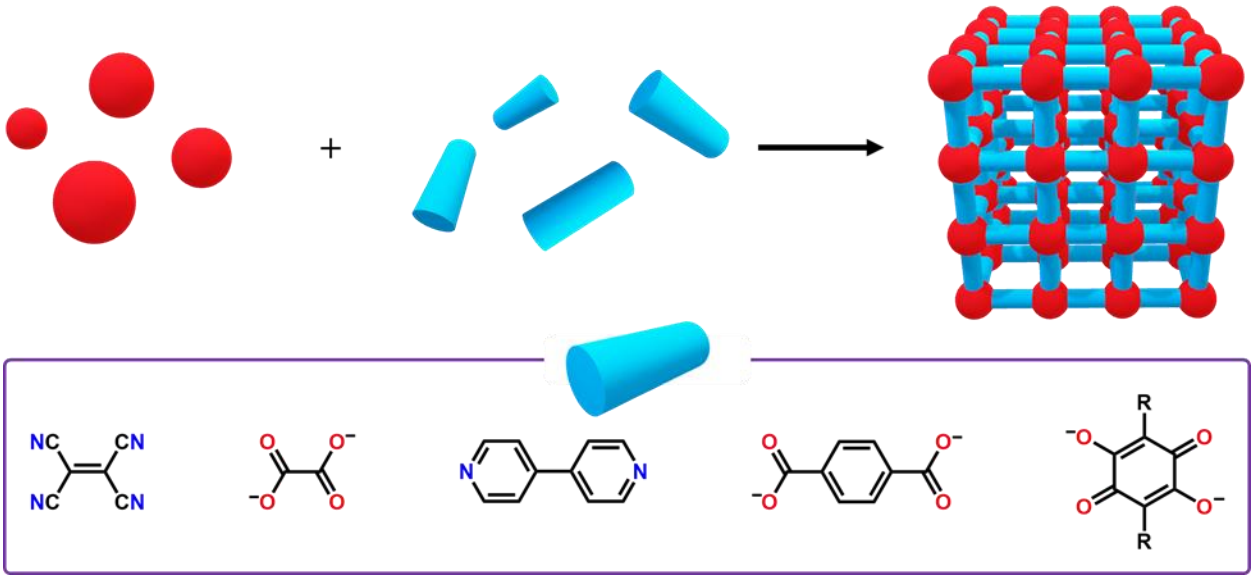

Figure 1.1. Infinite Coordination Polymers are assembled from transition metal ions or clusters (red spheres) with multidentate organic linkers (blue cylinders) to form 1D, 2D, or 3D structures. Examples of organic linkers are not limited to the ones presented here.

through judicious choice of metal ion or linkers. Furthermore, the porous nature of 2D and 3D ICPs and MOFs enable further modification post-synthesis via ligand or metal exchange reactions, permitting access to structures that could not be obtained through direct methods.[5] Due to their high degree of tunability, ICPs have shown exceptional promise in the areas of gas uptake and storage, chemical separations, lightweight permanent magnets, and as chemical sensors. [1-4, 6-10] Herein, we target MOFs as a platform for the investigation of substituent effects in a series of 2D iron-quinoid metal-organic magnets (Chapter 2) before designing a series of the stimuli-responsive ICPs employing the Weak-Link Approach to supramolecular chemistry (Chapter 3).

1.1 Metal-Organic Magnets

Metal-organic magnets are an emerging class of materials wherein the magnetic properties arise primarily from unpaired electrons on transition metal or lanthanide ions coordinated by organic ligands, and magnetic complexes featuring single metal ions or multinuclear metal species have been realized.[11-16] Foregoing the dense structure of traditional inorganic magnets wherein

chemical modification can be challenging, metal-organic magnets are infinitely tunable through changes to the paramagnetic metal ions or the organic coordinating groups and have potential applications in high density data storage, spintronic materials, and as lightweight permanent magnets. Unfortunately, for most metal-organic magnets, the magnetic ordering temperature (or blocking temperature), T_c (T_B), the temperature below which the materials display slow magnetic relaxation or permanent magnetism, is too low for practical use, often requiring liquid helium temperatures to operate. Indeed, single ion[17, 18] and dinuclear[19] metal-organic magnets that operate near liquid nitrogen temperatures have only recently been realized. One method to increase T_c in multinuclear metal-organic magnets is to increase the strength of magnetic coupling between the spin centers.

In traditional inorganic magnets, magnetic coupling occurs via direct metal-metal bonding[20, 21] or via the superexchange pathway[22-24], a coupling scheme mediated through closed-shelled, diamagnetic bridging units. For multi-nuclear metal-organic magnets, the superexchange pathway has been the most widely reported. Where inorganic magnets mediate this pathway through short monoatomic building units such as oxides, the promise of ligand tunability in metal-organic magnets necessitates the use of polyatomic organic bridging ligands. Unfortunately, the strength of magnetic coupling, and correspondingly T_c, possible via superexchange exponentially decreases with increasing number of bridging atoms.[25] As such, the feasibility of a room-temperature metal-organic magnet operating through a superexchange mechanism with a polyatomic organic linker is dubious. A promising alternative to superexchange, however, is magnetic coupling via direct exchange.

1.1.2 Increasing Magnetic Coupling Through Redox-Active Ligands

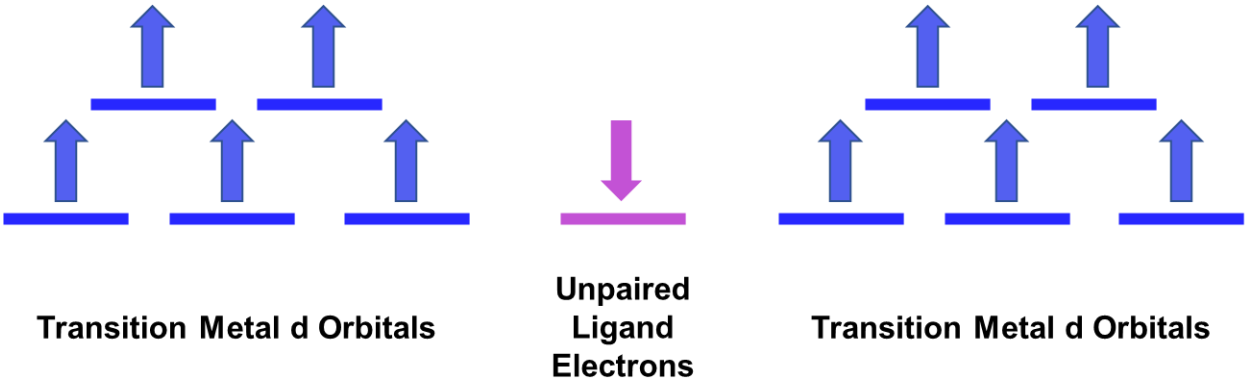

Figure 1.2. An unpaired electron residing in the organic ligand orbital mediates interactions between two high-spin transition metal ions, increasing magnetic coupling between the two metal centers.

Instead of coupling through closed-shell orbitals, one can imagine a system wherein coupling occurs through direct orbital-orbital overlap via open-shell metal- and ligand-based orbitals. This type of exchange interaction is referred to as direct exchange.[26-28] In direct exchange, an unpaired electron residing in the ligand-based orbital couples antiferromagnetically to the unpaired electrons residing in the metal-based orbitals. As the S = ½ unpaired electron is simultaneously interacting with both metal ions, this forces an overall ferrimagnetic interaction between the two metal ions according to the Pauli exclusion principle (**Figure 1.2**). Direct exchange can be achieved in coordination compounds using redox-active bridging ligands, wherein a one-electron oxidation or reduction of the ligand generates the unpaired electron. Indeed, metal-organic magnets featuring unprecedented strengths in magnetic coupling have been achieved via reduction of pyrazine,[29, 30] benzoquinoids,[31-34] organonitriles,[35-37] and dinitrogen,[38, 39] among others, making direct exchange a promising route for the generation of high-temperature metal-organic magnets.

1.1.2 ICP and MOF Magnets

Recently, there has been increased interest in the design and synthesis MOF-based magnets.[6, 7, 25] As permanent magnetic materials necessitate long range coupling interactions

between many spin centers, ICPs and MOFs represent an ideal platform for the design of metal-organic magnets with high-operating temperatures because of their near-infinite extended structure. Furthermore, unlike their dense inorganic counterparts, MOF magnets show promise for the synthesis of porous, lightweight magnets due to their high surface areas and open channel networks. Initial materials utilized closed-shell ligands, but the most successful MOF and ICP magnets to date have utilized redox-active bridging ligands. In fact, the few examples of room-temperature metal-organic magnets fall within this category.[29, 36, 37, 40] In addition to their ability to generate much higher T_c's than typically seen in their molecular counterparts, ICP and MOF magnets are excellent platforms for the investigation of the structure/function relationships for the generation of high T_c magnets because of their typical high-degree of crystallinity that permits structural analysis by X-ray crystallography. In Chapter 2, we take advantage of this to investigate the role substituents may play in impacting the magnetic ordering temperatures of MOF magnets.

1.2 Bioinspired Supramolecular Architectures

Nature's ability to use structure to control complex chemical processes is unparalleled. Where chemists have traditionally focused more on ionic or covalent bond formation, Nature takes advantage of both bonding and much weaker intermolecular interactions (e.g. hydrogen bonding, π-π stacking interactions, Van der Waal's forces, etc.) to control biological reactions such as molecular chaperoning, signal transduction, and catalysis.[41, 42] Paramount to all biological processes and catalysis is the ability to recognize and bind substrates with a high degree of specificity, and the aforementioned non-covalent interactions permit the flexibility and precision necessary to conduct many procedures.

One way Nature uses structure to control chemical reactivity in proteins and enzymes is through a process known as allosteric regulation.[43-45] In allosteric regulation, binding at a primary

chemical site is controlled through binding of an ionic or molecular species at a distal, secondary site within the structure (**Figure 1.3**). Upon coordination of an ionic or molecular trigger, referred to as an allosteric effector, to the target site, a structural transformation occurs within the protein that opens the primary site to target substrates. Allosteric regulation can be found in many biological processes, but as illustrative examples, we will focus on two: 1) transport of oxygen via cooperative binding to the heme unit of hemoglobin and 2) the production of pyruvate and adenosine triphosphate (ATP) via pyruvate kinase.

Hemoglobin is a tetrameric metalloprotein found in the red-blood cells of most mammals and is responsible for the transport of oxygen throughout the human body.[46, 47] Each of the four subunits of hemoglobin contains an iron-heme. Oxygen binding to the iron of one heme group induces a structural transformation throughout the entire protein that encourages binding of oxygen at the other heme units, a cooperative binding effect.[48] Upon transportation to an area of low pH or low concentrations of oxygen, oxygen is released from hemoglobin, and the protein returns to its original conformation. Notably, the allosteric regulation observed in hemoglobin allows for the transport of more oxygen than if there was no cooperative binding effect.

Another example of allosteric regulation in Nature can be found in pyruvate kinase, an enzyme active in the final step of glycolysis.[49, 50] Pyruvate kinase is activated by the glycolytic intermediate fructose-1,6-biphosphate.[51] In its active form, pyruvate kinase has a high substate

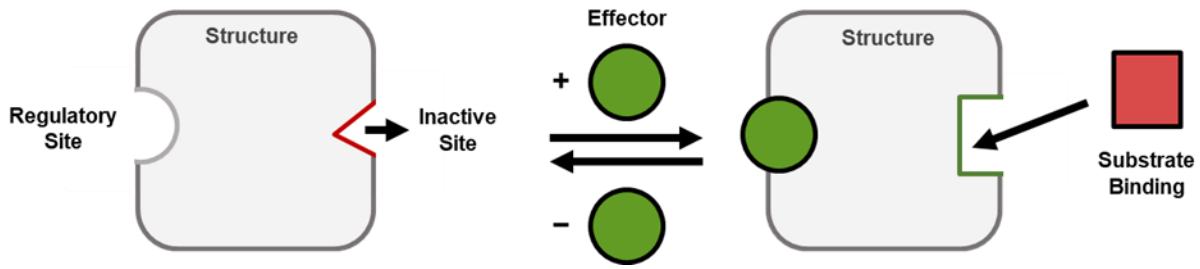

Figure 1.3. In allosteric regulation, binding of a chemical effector to a secondary, regulatory site induces a structural transformation, opening a once inactive site for substrate binding and further transformations.

affinity and catalyzes the transformation of phosphoenolpyruvate and adenosine diphosphate (ADP) to pyruvate and ATP. Pyruvate kinase is deactivated by ATP and alanine. The pyruvate that is produced continues toward other metabolic pathways, making the allosteric regulation found in pyruvate kinase a key component controlling cellular metabolism.

The elegant way Nature uses structure and non-covalent interactions to control substrate recognition and chemical reactivity led to the development of the field of supramolecular chemistry. Mimicking the intermolecular forces employed by Nature, supramolecular chemistry seeks to build larger assemblies of molecules through noncovalent interactions such as hydrogen bonding, π-π stacking, halogen bonding, cation-π, anion-π, hydrophilic/hydrophobic interactions, among others to assemble complex biomimetic and abiotic architectures. Since the initial synthesis of crown ethers that host alkali metal ions in solution,[52] coordination chemistry has been shown to be a particularly salient approach for the synthesis of bioinspired supramolecular architectures. This is in part due to the high modularity of coordination compounds, and the many diverse structure types that can be achieved. Furthermore, the coordination bond itself is dynamic, making metal, ligand, and substrate exchange facile. Methods for the synthesis of coordination-chemistry-based supramolecular constructs generally fall under one of three strategies: the Directional Bonding Approach (DBA),[53-55] the Symmetry-Interaction Approach (SIA),[56] and the Weak-Link Approach (WLA).[57, 58] We will briefly discuss the DBA and SIA before focusing the remainder of this section on the WLA.

1.2.1 Coordination Chemistry Based Approaches to Bioinspired Supramolecular Constructs

Of the many approaches for the construction of coordination-based supramolecular architectures, the DBA, SIA, and WLA represent three of the most well developed. Pioneered by

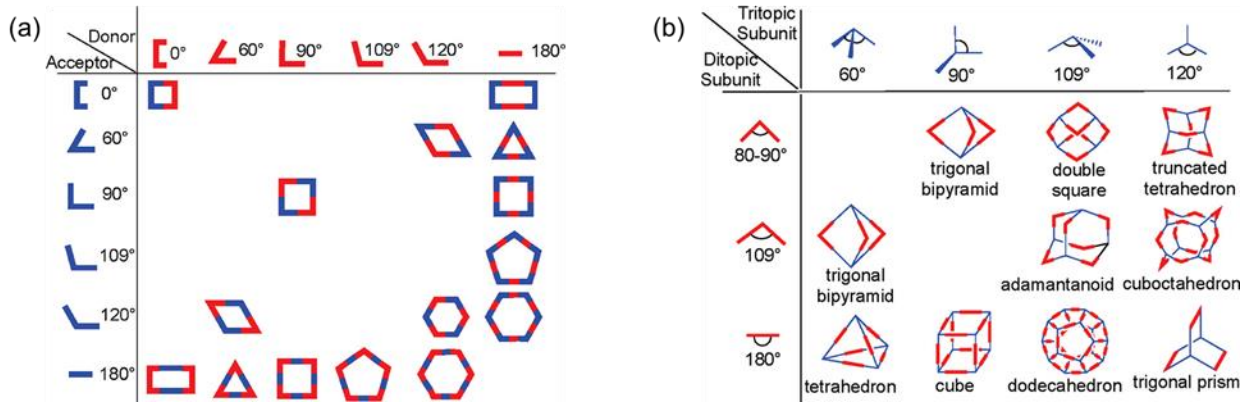

Figure 1.4. Examples of the (a) 2D and (b) 3D architectures that can by synthesized based on the coordination angles of the molecular subunits in the Directional Bonding Approach. Adapted with permission from Chakrabarty, R.; Mukherjee, P. S.; Stang, P. Supramolecular Coordination: Self-Assembly of Finite Two- and Three-Dimensional Ensembles. *Chem. Rev.* **2011**, *111*(11), 6810–6918. Copyright 2011 American Chemical Society.

the Fujita[59, 60] and Stang[61] groups, the DBA relies upon assembling complementary, rigid organic ligands with predefined angles to di- and tritopic metal precursors to achieve discreet 2D and 3D architectures (**Figure 1.4**). For example, if a discerning supramolecular chemist sought to synthesize a molecular square using this approach, he or she may react a metal precursor featuring a 90° coordination angle, such as that found in [1,3-bis(diphenylphosphino)propane]palladium(II) triflate, with an organic ligand featuring a 180° coordination angle, such 4,4'-bypridine in the appropriate stoichiometry (**Scheme 1.1**).[61] Similar to the DBA, the SIA relies upon the interactions between rigid organic linkers and transition metal or main group ions, but now focus on chelating ligands and the formation of chelate planes and the relationship of these planes to one another to

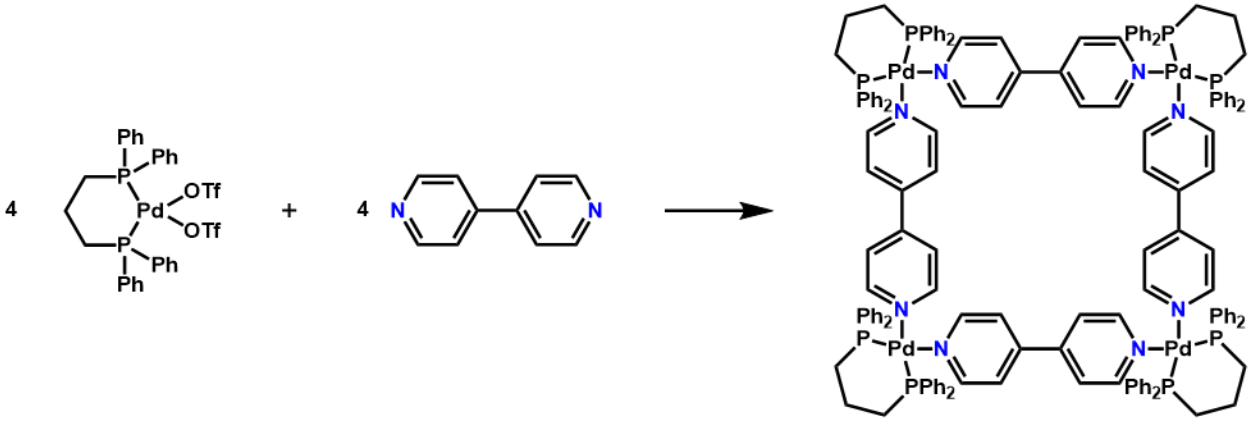

Scheme 1.1. Synthesis of a supramolecular square using the Directional Bonding Approach.

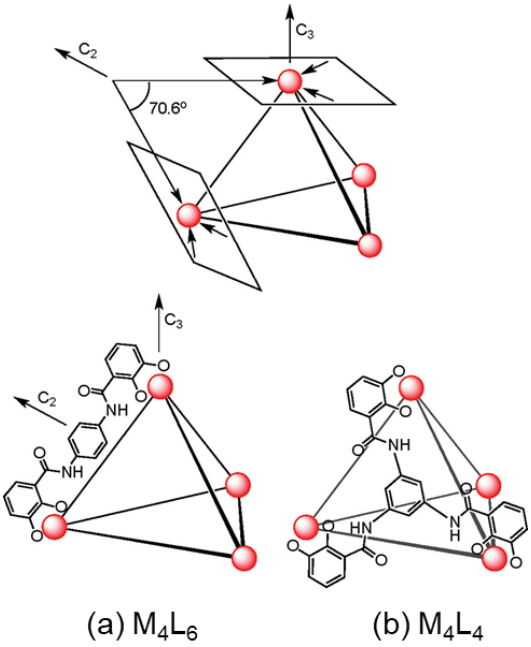

Figure 1.5. Example of the coordination planes and rotational axes considered when building an (a) M_4L_6 and (b) M_4L_4 tetrahedron by the Symmetry Interaction Approach. Reprinted with permission from Chakrabarty, R.; Mukherjee, P. S.; Stang, P. Supramolecular Coordination: Self-Assembly of Finite Two- and Three-Dimensional Ensembles. *Chem. Rev.* **2011**, *111*(11), 6810–6918. Copyright 2011 American Chemical Society.

assemble 3D materials.[62] The chelating plane in the SIA is the plane orthogonal to the major symmetry axis of the metal complex that forms a particular node, and it is the orientation of these planes in relation (i.e. dihedral angle or symmetry axes) that defines the molecular architecture that is formed (**Figure 1.5**). Importantly, the supramolecular cages and receptors synthesized using both approaches have been shown to facilitate chemical reactions within their pockets and pores that would be otherwise unfavorable, as important molecular capsules for host-guest interactions, and more recently been developed for biological applications such as nanocarriers for drug delivery.[55, 63, 64]

1.2.2 The Weak-Link Approach to Supramolecular Chemistry

To mimic the type of allosteric regulation found in proteins in an abiotic material, one must develop a platform that can be used to synthesize dynamic, flexible architectures. To address this challenge, the Mirkin group pioneered the WLA to supramolecular chemistry.[57, 58, 65, 66] Whereas the DBA and SIA utilize rigid organic linkers and metal precursors, the WLA employs flexible organic ligands with tailorable binding affinities to form dynamic supramolecular architectures. To achieve these materials, the WLA uses hemilabile ligands, multi-dentate organic ligands that feature binding moieties with different affinities for transition metal ions. A typical hemilabile ligand in the WLA features two binding moieties: a “strong” link that is coordinately inert (i.e.

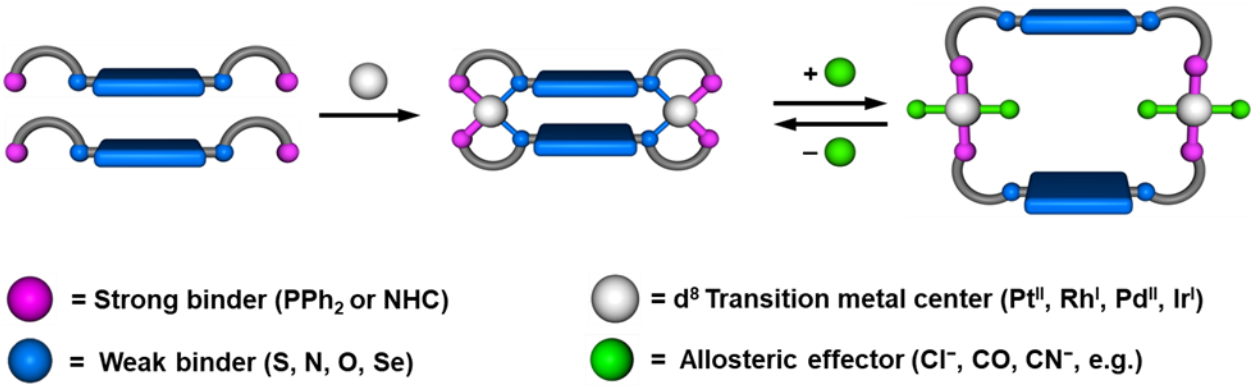

Figure 1.6. The Weak-Link Approach to supramolecular chemistry uses transition metal ions and hemilabile ligands, chelating ligands that feature moieties with two different binding strengths, to synthesize condensed structures that can be opened to a more flexible structure in the presence of small molecule or anionic chemical effectors and redox chemistry.

phosphino- or N-heterocyclic carbene) and a "weak" link that is coordinately labile (i.e. thioether, amine, or ether). When exposed to d^8 transition metal ions (e.g. Rh^{I},[65, 67-71] Ru^{I},[72] Ir^{I},[73] Ni^{II},[74] Pd^{II},[75] and Pt^{II},[76]), the hemilabile ligands chelate to form a rigid, closed, condensed structure that can be systematically opened upon exposure to small molecules (e.g. CO, CH_3CN, MeOH) or anions (e.g. halides or CN^-) (**Figure 1.6**). When added to the closed complexes, these small molecule and anion effectors preferentially displace the "weak" link and bind to the WLA metal center, forming a more flexible architecture. Due to the modular nature of the metal ions and hemilabile ligand utilized in the WLA, we have successfully synthesized a variety of supramolecular structures including molecular tweezers,[76-79] macrocycles,[70, 73, 75, 80-85] and triple-layer deckers,[86-89] and have shown the physical and chemical properties of the structures can be toggled based on the structural state of the materials. Indeed, we have been able to realize abiotic, enzyme mimics that function as stimuli-responsive catalysts,[86, 87] signal amplifiers,[80, 81] fluorescent probes,[78, 79] and light-harvesting materials[88, 89]. As illustrative examples of the chemical control afforded via the WLA, we will briefly discuss two examples of stimuli-responsive materials designed with the platform.

In 2008, our group published a polymerase chain reaction (PCR) mimic for the detection of acetate ions in solution.[81] In biochemistry and molecular biology, the PCR is a technique for the replication and enhancement of specific DNA sequences and has found ubiquitous use in diagnostic technologies, including recent tests for the virus that causes COVID-19. At the time of the publication, no PCR-like system for the detection of non-nucleic acid targets had been achieved. Building upon a previously reported system,[80] a Zn(II)-salen moiety was imbedded within a Rh^{I}-based WLA macrocycle. In its closed state, there is almost no catalytic activity. However, upon exposing the assembly to a small concentration of acetate ions, the macrocycle opens, exposing the Zn(II)-salen moiety, catalyzing an acyl transfer from acetic anhydride to pyridiylcarbonol, generating more acetate in the process (**Figure 1.7**). Over time, this leads to the formation of increasing concentrations of the open-catalytic form of the WLA complex and faster reaction times. Coupling this process to a pH-fluorescent probe allows for the detection of nanomoles of acetate within solution.

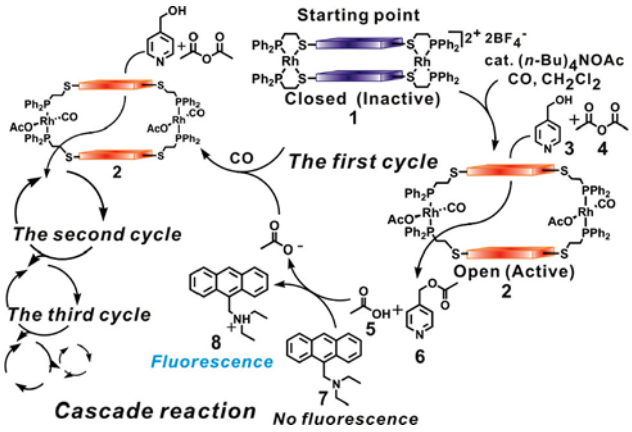

Figure 1.7. Proposed PCR-like mechanism for the detection of acetate ions in solution via a WLA supramolecular macrocycle. Reprinted with permission from Yoon, H. J.; Mirkin, C. A. PCR-like Cascade Reactions in the Context of an Allosteric Enzyme Mimic. *J. Am. Chem. Soc.* **2008**, *130*(35), 11590–11591. Copyright 2008 American Chemical Society.

In another example of the WLA's ability to synthesize allosteric enzyme mimics, our group reported the synthesis of a triple-layer structure for on/off catalysis. The heteroligated WLA complex featured a Al(III)-salen moiety – which can act as a ring-opening polymerization catalyst for the transformation of ε-caprolactone to polycaprolactone – within its center layer and bulky tertiary-amino ligands in its top and bottom layers.[86] When fully closed, the rigid architecture

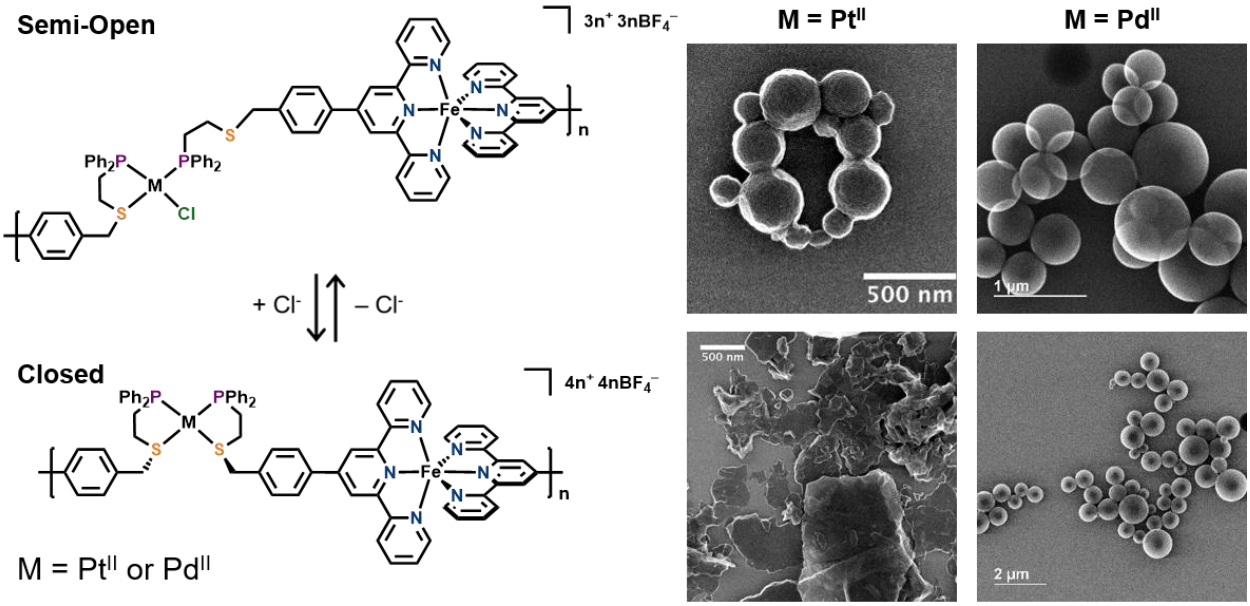

Figure 1.8. ICP particles composed of WLA molecular subunits polymerized via Fe^{II}. Proposed polymer structure (*left*) and STEM micrographs (*right*) of Pt^{II}-based and Pd^{II}-based ICP particles prepared from 8 mM solutions. Adapted with permission from d'Aquino, A. I.; Kean, Z. S.; Mirkin, C. A. Infinite Coordination Polymer Particles Composed of Stimuli Responsive Coordination Complex Subunits. *Chem. Mater.* **2017**, *29*(24), 10284–10288. Copyright 2017 American Chemical Society.

precluded an appreciable conversion of ε-caprolactone to polycaprolactone (~7% conversion after 100 hrs) by blocking the active site with the bulky tertiary amines. Upon opening the structure with Cl^- anions, near quantitative conversion occurs within 24 hrs at elevated temperatures. Notably, the activity of the catalyst can once again be turned off by using halide abstraction reagents to remove the Cl^- anions from solution.

While the above examples are just a small representation of the supramolecular constructs that can be achieved via the WLA, many of the investigations to date have focused on discrete molecular architectures. Therefore, we began to wonder if the WLA could be employed to realize stimuli-responsive architectures in the solid state, such as ICPs. To investigate, we synthesized a series of amorphous WLA-ICP particles. The ICP particles were composed of a WLA monomer complex featuring phosphino-thioether (P,S) hemilabile ligands with appended terpyridine (tpy) moieties.[90] Upon reaction of a Pt^{II} or Pd^{II} WLA complex bearing P,S-tpy ligands with Fe^{II}, WLA-

ICP particles were obtained (**Figure 1.8**). We found that the morphology of the particles could be regulated by the structural state of the embedded WLA monomers. While this work highlighted the WLA's ability to control the chemical and physical properties of an extended, infinite material, the amorphous nature of the particles precluded a complete crystallographic analysis of the structural transformation induced upon chemical effector binding. We, therefore, have sought to further probe the types of structural transformations that can be achieved in a WLA solid, extended material, and that work is reported within Chapter 3.

1.3 Introduction to Dissertation Topics

Coordination chemistry and the diverse structures and functions of its materials unite all the topics discussed within this dissertation. We begin by utilizing the electronic structure of transition metal coordination complexes to develop novel metal-organic framework magnets in the first chapter before focusing on the development of stimuli-responsive ICPs and molecular tweezers using the WLA.

1.3.1 Substituents Effects in a Series of 2D Iron-Quinoid Magnets

As aforementioned, metal-organic magnets have been touted for their potential as multifunctional materials but have not found practical use due, in part, to the low temperatures required for their function. Of the metal-organic magnets that display permanent magnetism at room temperature, most are extremely air-sensitive and their structures are poorly characterized. In an effort to help elicit future design principles for high-temperature metal-organic framework magnets, we have synthesized a series of isostructural 2D iron-quinoid framework with general formula $(Me_4N)_2Fe_2{}^{R}L_3$ ($H_2{}^{OMe}L$ = 2,5-dihydroxy-3,6-dimethoxy-1,4-benzoquinone; $H_2{}^{Cl}L$ = 2,5-dihydroxy-3,6-dichloro-1,4-benzoquinone; $H_2{}^{Br}L$ = 2,5-dihydroxy-3,6-dibromo-1,4-

benzoquinone; $Na_2^{NO2}L$ = sodium 2,5-dihydroxy-3,6-dinitro-1,4-benzoquinonate). X-ray crystallography and spectroscopic characterization reveal all the frameworks undergo spontaneous electron transfer from Fe^{II} to the bridging benzoquinoid ligand during synthesis, such that the final materials contain a ratio of dianionic $^{R}L^{2-}$ and radical trianionic $^{R}L^{3\bullet-}$ ligands, determined by the identity of the ligand functional group. Analysis of the magnetic properties of the materials reveal that the magnetic ordering temperatures are greatly affected by the nature of the ligand substituent, as the framework containing the highly electron-withdrawing nitro substituent orders the highest whereas the methoxy derivative orders much lower. These results are contributed to differences in the relative oxidation states of each framework.

1.3.2 Structurally Dynamic 1D Coordination Polymers Enabled via the Weak-Link Approach

Next, in Chapter 3, we use the WLA to design and synthesize crystalline, stimuli-responsive 1D coordination polymers. Specifically, the reaction of a closed, pyridine-functionalized WLA monomer complex with $Cu(BF_4)_2 \cdot 6H_2O$ in acetonitrile or *N*,*N*-dimethylformamide (DMF) yields three isostructural 1D zig-zag chains. One of the polymers was studied via single-crystal X-ray diffraction (SCXRD), nuclear magnetic resonance (NMR) spectroscopy, and mass spectrometry (MS), and its response to a chemical effector (halide ion, Cl^-) was investigated. Importantly, our investigation of one of the model chains revealed the characteristic structural switchability of the WLA complex from which it is comprised. Upon exposure to Cl^- anions, it disassembles into its molecular components, including the fully-opened congener of the initial WLA complex. Thus, one can control crystalline chain assembly via the structural state of the WLA monomer complex. Taken together, this work has demonstrates that the WLA represents a promising method for the construction of allosteric, stimuli-responsive

coordination polymers, including potentially higher-ordered structures like metal organic frameworks.

1.3.3 Efforts towards Reversible Water-Soluble Weak-Link Approach Tweezers

In Chapter 4, we detail efforts towards the development of WLA complexes that can operate reversibly in water. To date, most of the WLA literature has been conducted within organic media. This is largely because the water-soluble WLA complexes that have been synthesized can only be opened irreversibly by effectors such as CN^-. We hypothesize that weakening the chelate by exchanging the thioether moieties for ether functional groups will permit reversible toggling of the WLA structural state using weaker effectors such as halide anions. To investigate, we synthesized two new water-soluble WLA complexes, one featuring a thioether and the other an ether, and attempted to characterize their structure in solution.

Chapter 2

Substituent Effects in a Series of 2D Iron-Quinoid Metal-Organic Magnets

The work presented in this chapter is based upon the following unpublished work:

Coleman, B. D.; Wang, Y.; Hua, C.; DeGayner, J. A.; Harris, T. D. Substituent Effects in a Series of 2D Iron-Quinoid Metal-Organic Magnets. *Unpublished Results.*

The numbers, symbols, and other notations used to present chemical structures are self-contained in this chapter.

2.1 Introduction

Over the last several decades, metal-organic magnets have garnered intense interest due to their potential applications as lightweight permanent magnets, magnetic switches, and components in next generation energy and data storage materials.[91-93] One of the main figures of merit in the design and characterization of new magnet materials is the magnetic ordering temperature, T_c, the temperature below which a material displays spontaneous magnetization. Unfortunately, molecular magnets in which spontaneous magnetization occurs at ambient temperatures are exceedingly rare.[11, 12] In 1991, Miller and coworkers reported the first room-temperature metal-organic magnet, $V(TCNE)_x \bullet y CH_2Cl_2$ (TCNE = tetracyanoethylene).[36] The highly air-sensitive material was shown to display permanent magnetism up to 315 K, its thermal decomposition temperature. While it was shown via vibrational spectroscopy that $V(TCNE)_x \bullet y CH_2Cl_2$ undergoes a charge transfer process such that it contains $[TCNE]^{\bullet -}$, further structural characterization was not possible as the compound is amorphous. Three more room-temperature magnets were reported in 2007 by Hicks and coworkers incorporating TCNE, TCNQ (TCNQ = 7,7,8,8-tetracyanoquinodimethane), and DDQ (DDQ = 2,3-dichloro-5,6-dicyano-1,4-benzoquinone).[37] Spectroscopic studies indicated that the three magnets form from a charge transfer from Ni^{II} to the organic ligand, but structural characterization via X-ray diffraction techniques was not possible due to the amorphous nature of the compounds. Indeed, the lack of structural characterization via diffraction techniques is a reoccurring challenge within the reports of compounds displaying high T_c's, limiting an unambiguous assignment of design criteria for high magnetic ordering temperatures in metal-organic magnets.

Metal-organic frameworks (MOFs), in which metal nodes are linked by organic bridging ligands, are particularly well-suited to the study of structure-function relationships. MOFs are highly crystalline and readily characterized via X-ray diffraction techniques. Furthermore, their high degree of chemical tunability permits their rational design via judicious choice of metal cation and organic linkers.[1, 4] In addition, the porous nature of MOFs enables facile post-synthetic modification via metal exchange, ligand exchange, or redox chemistry.[5, 94] Importantly, MOFs have been shown to exhibit long-range magnetic ordering.[6, 25, 95] However, while magnetic MOFs have displayed T_c's above 100 K,[96-98] most order at temperatures below 77 K, limiting their practical use in materials. MOFs are typically constructed with closed-shell organic linkers, thus the strength of magnetic coupling between metal centers is considerably weaker via superexchange. As a material's T_c is strongly correlated to the strength of magnetic coupling between spin centers,[99] stronger exchange mechanisms between metal ions are necessary. One such solution is to employ paramagnetic bridging ligands to engender strong direct exchange between the metal center and organic radical.[100-103] The bis-bidentate derivatives of 2,5-dihydroxy-1,4-benzoquinone (DHBQ, **Figure 2.1**) are exceptional candidates for the construction of magnetic MOFs as they have been shown to readily form extended solids[104] and have three easily accessible

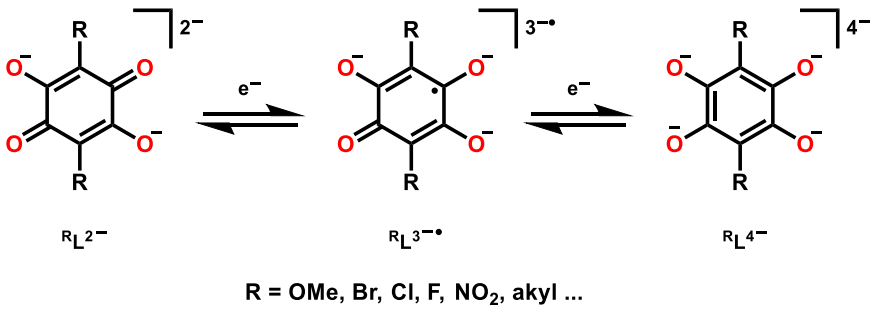

Figure 2.1. Redox series of benzoquinoid ligands based on DHBQ: $^{R}L^{2-}$(left), $^{R}L^{3-\bullet}$(center), and $^{R}L^{4-}$ (right).

oxidation states, including the radical $^{R}L^{3\bullet-}$ semiquinone redox isomer. In addition, dinuclear complexes incorporating radical semiquinone linkers have displayed strong magnetic coupling with various transition metal ions.[31, 32, 105, 106]

Previous work targeted a system shown to undergo *in situ* electron transfer from Fe^{II} to $^{Cl}L^{2-}$.[107] Reaction of $Fe(BF_4)_2 \bullet 6H_2O$ and chloranilic acid ($H_2{}^{Cl}L$) in DMF under solvothermal conditions yielded a 2D hexagonal structure in which honeycomb-like layers in the crystallographic *a*-*b* plane are eclipsed along the *c* axis (**Figure 2.2**).[108] Spectroscopic characterization showed that an *in situ* electron transfer does indeed occur during synthesis such that the final material can be formulated as $(Me_2NH_2)_2Fe^{III}{}_2(^{Cl}L^{3\bullet-})_2(^{Cl}L^{2-}) \bullet 2H_2O \bullet 6DMF$ (**1**). The as-synthesized, solvated framework displayed a magnetic ordering temperature of T_c = 80 K. Upon further one-electron reduction of the framework via soaking single-crystal in cobaltocene, an increase in the magnetic ordering temperature can be observed with T_c = 105 K.[94] Following this work, we sought to understand how modulating the electronic structure of the radical semiquinone ligand via substituent effects would impact the magnetic ordering temperature of 2D iron-quinoid MOF magnets.

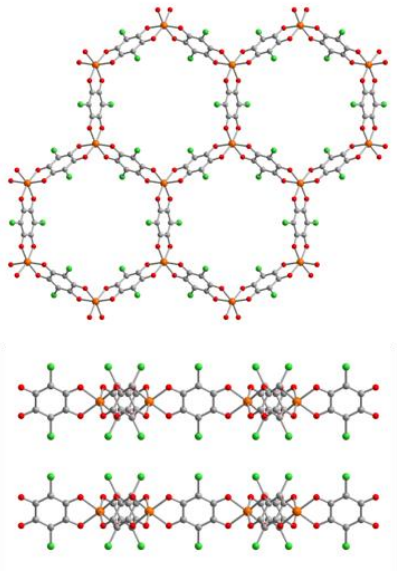

Figure 2.2. X-Ray crystal structure of **1** as viewed along the crystallographic *c* axis (upper) and *b* axis (lower). Orange, green, red, and gray spheres represent Fe, Cl, O, and C atoms, respectively. Cations and H_2O molecules are omitted for clarity. Reprinted with permission from Jeon, I.-R.; Negru, B.; Van Duyne, R. P.; Harris, T. D. A 2D Semiquinone Radical-Containing Microporous Magnet with Solvent-Induced Switching from T_c = 26 to 80 K. *J. Am. Chem. Soc.* **2015**, *137*(50), 15699–15702. Copyright 2015 American Chemical Society.

Herein, we have synthesized a series of four hexagonal, honeycomb-like frameworks with various substituents with the general formula $(Me_4N)_2Fe_2{}^{R}L_3$ (R = (**2**) OMe, (**3**) Br, (**4**) Cl, and (**5**) NO_2) that are isostructural to the previously reported $(Me_2NH_2)_2Fe_2{}^{Cl}L_3 \bullet 2H_2O \bullet 6DMF$[108]. We

hypothesized that modulating the electron density within the six-membered ring via resonance and induction effects would correspond to an elevation or depression of the observed T_c. Specifically, the use of stronger electron-withdrawing substituents on the semiquinone linker would afford a corresponding framework with a lower T_c due to the substituent's ability to lower the spin density on the donor O-atoms, similar to behavior observed in $Cr^{III;}$ [109, 110] and $Fe^{III;}$ [110] molecular complexes and Fe, Mn, and Cr frameworks[111] bridged by various dianionic quinoid ligands. DC and AC magnetometry of the series showed a surprising trend in magnetic ordering temperatures with T_c = 16 K, T_c = 22 K, T_c = 30 K, and T_c = 90 K for **2**–**5**, respectively. Spectroscopic investigations revealed differences in the overall oxidation states of the embedded semiquinone ligands, contributing to the observed trend in T_c as a higher degree of reduction would result in stronger magnetic coupling between metal centers, convoluting the inductive and resonance effects of substituents on the magnetic ordering temperature. Nevertheless, this work demonstrates that the functional group attached to the bridging-semiquinone ligand has a quantifiable effect on the observed magnetic properties of resulting framework materials and can be employed to tune the magnetic properties of future metal-organic compounds.

2.2 Results and Discussion

2.2.1 Synthesis and Structure of 2, 3, 4, and 5

In an effort to ensure that the series of frameworks only differed in the substituent group attached to the semiquinone ligand, we screened reaction conditions involving various benzoquinoid ligands with dimethyl-, tetramethyl-, and tetraethylammonium cations to produce a

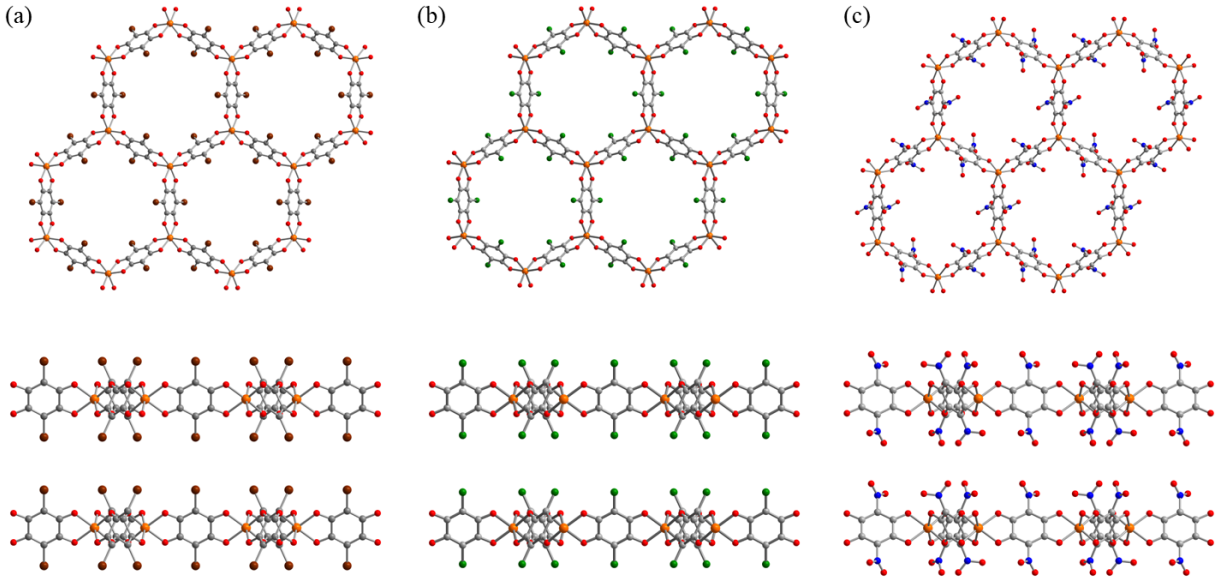

Figure 2.3. X-ray crystal structure of (a) **3** , (b) **4**, and (c) **5** along the crystallographic *c* axis (upper) and *b* axis (lower). Orange, brown, green, red, blue, and gray spheres represent Fe, Br, Cl, O, N, and C atoms, respectively. Cations have been removed for clarity.

series with near identical interlayer spacings between stacked honeycomb layers. Reaction of equimolar amounts of $Fe_2(BF_4)_2$•$6H_2O$ and the appropriate ligand precursor ($H_2^{OMe}L$, $H_2^{Cl}L$, $H_2^{Br}L$, or $Na_2^{NO_2}L$) in the presence of four equivalents of Me_4NBF_4 in DMF for two days at 130 °C under dinitrogen afforded shiny, green-black crystals of $(Me_4N)_2Fe_2^{OMe}L_3$ (**2**), $(Me_4N)_2Fe_2^{Br}L_3$ (**3**), $(Me_4N)_2Fe_2^{Cl}L_3$ (**4**), and $(Me_4N)_2Fe_2^{NO_2}L_3$ (**5**). The syntheses were found to be highly sensitive to dissolved water within the reaction medium. Phase-pure samples of **5** required 27 equivalents of deionized water to be added, whereas addition of water to the reaction media of **2**, **3**, and **4** resulted in amorphous green-black powders.

All the compounds were readily characterized by powder X-ray diffraction (PXRD) (**Figure 2.S1**). An indexing of their diffraction patterns at 298 K revealed compounds **2**–**5** crystalize in the trigonal $P\bar{3}1m$ space group. Compounds **2**–**5** have crystallographic *a* axes of 13.631(2), 13.620(4), 13.69(2), and 13.625(8) Å and *c*-axes of 10.247(2), 10.217(5), 10.33(3), and

10.147(5) Å, respectively. While the series displays statistically different lengths in both unit cell dimensions, inspection of their diffractograms indicate they are a family of isostructural compounds. Furthermore, compounds **3**, **4**, and **5** produced crystals suitable for structural characterization via single-crystal X-ray diffraction (SCXRD) techniques (**Figure 2.3, Table 2.S1**). The frameworks consist of 2D hexagonal, honeycomb-like layers formed from iron nodes bound by three $^{R}L^{n-}$ ligands, creating an overall anionic sheet. The sheets are eclipsed along the crystallographic *c* axis with charge balancing Me_4N^+ cations residing between the Fe of two adjacent layers. The eclipsed nature of the sheets creates hexagonal channels along the *c*-axis with a cross channel Fe···Fe distance of 15.7092(8), 15.671(2), and 15.6990(7) Å for **3**, **4**, and **5**, respectively. Disordered solvent molecules reside within these channels.

Previous studies of **1** illustrated that close analysis of the Fe–O, C–O, and C–C bond lengths can be used as an initial assessment of the electron transfer process between Fe^{II} and $^{R}L^{2-}$.[108] Frameworks **3**, **4**, and **5** have Fe–O bound lengths of 2.028(5), 2.018(6), and 2.008(3) Å, respectively. These distances are significantly shorter than those found within high-spin Fe^{II} complexes containing the dianionic $^{Cl}L^{2-}$ ligand[31] and can be assigned to high-spin Fe^{III} ions[112]. Furthermore, the C–O bond lengths within the ligands are 1.271(9), 1.275(9), and 1.288(6) Å, constituting an increase of 2.2, 2.5, and 3.5%, respectively, in comparison to the isostructural framework $(Me_2NH_2)_2Zn_2{}^{Cl}L_3$,[108] shown to contain exclusively $^{Cl}L^{2-}$. The observed increase in the bond lengths correlates to an overall lowering of the C−O bond order within the series of frameworks, with **5** exhibiting the lowest bond order. However, inspection of the mean C–C bond shows that they all fall within error of the mean C–C bond distances in the analogous Zn framework. Nevertheless, the increase and decrease of the C–O and Fe–O bond lengths, respectively, indicate that a spontaneous electron transfer process from Fe^{II} to $^{R}L^{2-}$ has occurred

within **3**, **4**, and **5**. Additionally, while pairs of C–O and Fe–O bond lengths between the frameworks fall within error, the subtle differences across the three compounds are indicative of different ratios of $^{R}L^{2-}$ and $^{R}L^{3\bullet-}$ present within each material.

2.2.2 Raman Spectroscopy

To more directly probe the ligand oxidation states and the relative ratios of $^{R}L^{2-}$ and $^{R}L^{3\bullet-}$ within the series, Raman spectra at ambient temperature with an excitation of 473 nm were collected for each framework (**Figure 2.4**). Due to the overlapping N-O vibrations, the Raman bands within **5** have not been assigned and will not be discussed. Although, it should be noted that the frequency range of the vibrations is consistent with the other members of the series. The vibrations at 1378, 1354, and 1383 cm^{-1} are assigned to the ν_{CC} bands within the ligands of **2**, **3**, and **4**, respectively. The corresponding vibration within the Zn analog occurs at 1360 cm^{-1}.[108] The significant shift observed in each framework is hypothesized to be due to the nature of the functional group attached to the ring, as the ν_{CC} band is expected to be susceptible to changes due to the substituent as suggested by vibrational spectra of related dinuclear complexes.[109, 110] Therefore, it is difficult to infer any information about the relative ratios of $^{R}L^{2-}$ and $^{R}L^{3\bullet-}$ from this vibration alone.

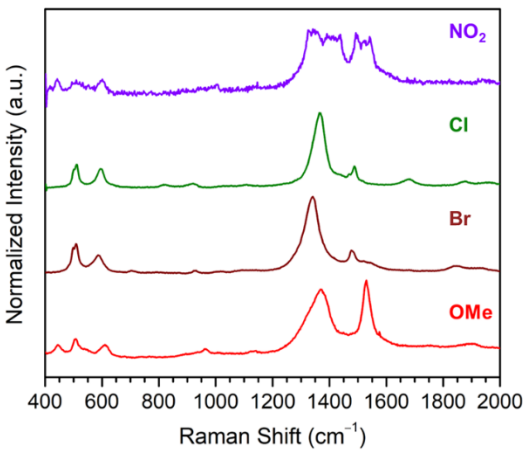

Figure 2.4. Raman spectra collected at ambient temperature for **2** (red), **3** (brown), **4** (green), and **5** (purple) following excitation at 473 nm.

Analysis of the ν_{CO} stretch reveals subtle differences between each framework. The Raman bands at 1537, 1486, and 1498 cm^{-1} are assigned as the ν_{CO} vibration of the bridging ligands in **2**, **3**, and **4**, respectively. These vibrations constitute a considerable red-shift in comparison to the ν_{CO} of

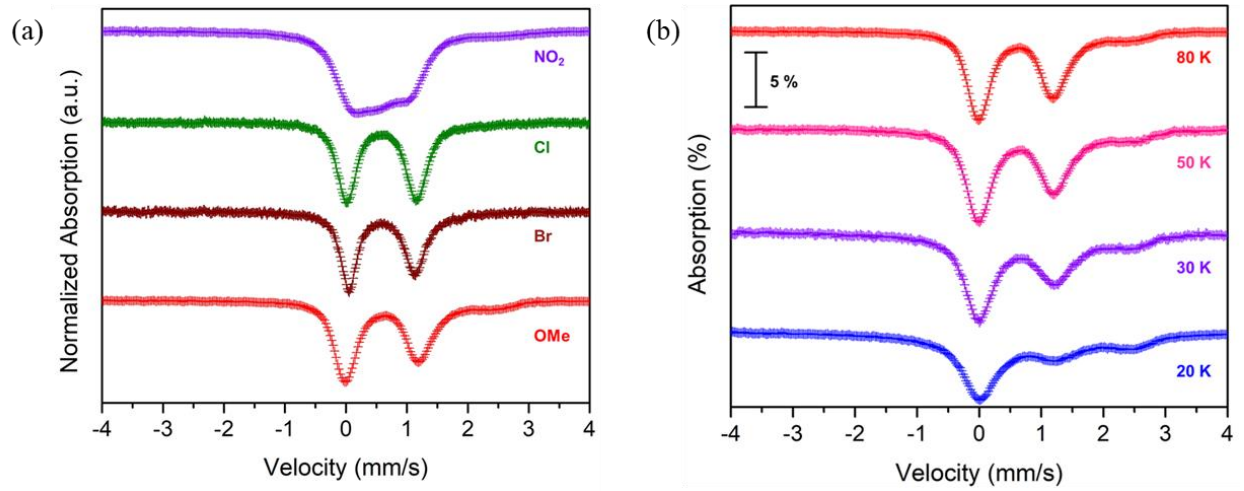

Figure 2.5. (a) Mössbauer spectra for **2** (red) at 80 K, **3** (brown) at 80 K, **4** (green) at 80 K, and **5** (purple) at 120 K. (b) Variable temperature Mössbauer spectra of **2** at 80 K (red), 50 K (magenta), 30 K (purple), and 20 K (blue).

1617 cm^{-1} observed within the Zn analog.[108] This suggests the presence of $^{R}L^{3\bullet-}$ within each framework, consistent with the previously discussed structural observations. Interestingly, compounds **3** and **4** possess vibrations in good agreement with the observed vibration of 1492 cm^{-1} for **1**,[108] whereas **2**'s vibration is considerably higher. While functionalization is expected to slightly alter the ν_{CO} of the ligands, the significant shift implies that **2** resides in a different overall oxidation state relative to the others. As the ligand reduction is expected to primarily occur via *in situ* one election transfer from Fe^{II} to the ligand, we turned to Mössbauer spectroscopy to further probe differences in oxidation state across the series of compounds.

2.2.3 Mössbauer Spectroscopy

Mössbauer spectra were collected for **2-5** to confirm the presence of Fe^{III} within the frameworks (**Figure 2.5a**). Frameworks **3** and **4** exhibit sharp quadrupole doublets, with fits of the data showing isomer shifts of δ = 0.594 mm/s and δ = 0.589 mm/s and quadrupole splittings of ΔE_Q = 1.090 mm/s and ΔE_Q = 1.149 mm/s, respectively, at 80 K. In both cases, these parameters can unambiguously be assigned as high-spin Fe^{III}. The similarity of their Mössbauer parameters,

the observation of solely high-spin Fe^{III}, and their similar Raman spectra indicate that **3** and **4** exist in similar oxidation states with a relatively equal ratio of $^{R}L^{2-}$ and $^{R}L^{3\bullet-}$ between frameworks (two $^{R}L^{3\bullet-}$ to one $^{R}L^{2-}$ based on the formula unit).

Due to the magnetic ordering temperature of **5** (discussed below), its Mössbauer spectrum was collected at 120 K and is markedly different. The broad, poorly defined doublet can be fit with two unique Fe centers having isomer shifts of δ = 0.544 mm/s and δ = 1.692 mm/s and quadrupole splittings of ΔE_Q = 0.770 mm/s and ΔE_Q = 2.324 mm/s, respectively. These parameters correlate to the presence of both high-spin Fe^{III} and high-spin Fe^{II} within **5**. The high-spin Fe^{II} species is tentatively assigned as a 7.0% contamination of $Fe(HCO_2)_2$ produced by the hydrolysis of DMF due to the addition of excess water necessary for synthesis. This is consistent with relative areas of the fits and elemental analysis of activated samples of **5**. Literature precedent has shown the formate anion is sufficient to reduce $^{Cl}L^{2-}$ to $^{Cl}L^{3\bullet-}$ *in situ*.[113] As $^{NO2}L^{2-}$ is predicted to have a more positive reduction potential due to its electron-withdrawing nature in comparison to the $^{Cl}L^{2-}$ ligand,[32, 109] we hypothesize that **5** contains a larger percentage of $^{R}L^{3\bullet-}$ relative to **2**, **3**, and **4**.

The Mössbauer spectrum of **2** collected at 80 K contains a sharp quadrupole doublet with an isomer shift of δ = 0.611 mm/s and quadrupole splitting of ΔE_Q = 1.134 mm/s and a broader quadrupole doublet with an isomer shift of δ = 1.243 mm/s and a quadrupole splitting of ΔE_Q = 2.217 mm/s. The two Fe centers can be unambiguously assigned to high-spin Fe^{III} and high-spin Fe^{II} with relative areas of 84.2% and 15.8%, respectively. Initially, we suspected this Fe^{II} species also arose from an $Fe(HCO_2)_2$ contamination, albeit in a much larger concentration. However, variable-temperature Mössbauer spectra obtained at 80, 50, and 20 K reveal that it arises a dynamic valence tautomerism within **2** (**Figure 2.5b**). Upon cooling to 20 K, the relative area of the high-spin Fe^{III} species decreases from 84.2% to 73.6%, and the relative area of the high-spin

Fe^{II} species increases from 15.8% to 26.4%. The interdependence of the areas of both Fe sites implies that the two species reside within the same material. As the electron transfer process arises from the oxidation of Fe^{II}, the ratio of $^{OMe}L^{3\bullet-}$ to $^{OMe}L^{2-}$ is dependent on the external temperature. A similar valence tautomerism has been discovered in related iron-benzoquinoid extended solids.[114, 115] Thus, from both spectroscopic techniques, **2** can be understood to contain a lower concentration of the radical semiquinone ligand versus the other members of the series.

2.2.4 Magnetic Properties

Variable-temperature dc susceptibility was utilized to investigate the magnetic properties of **2**–**5** **(Figure 2.6)** upon cooling samples under an applied field of 10 Oe. Each framework exhibits spontaneous magnetization upon cooling to temperatures below 100 K. This is determined by the abrupt increase in magnetization observed below 20 K for **2**, 30 K for **3**, 40 K for **4**, and 100 K for **5**. Intriguingly, **4** shows spontaneous magnetization at temperatures much lower than T_c = 80 K determined for **1**. This may indicate that not only does the nature of the substituent affect the magnetic properties of layered iron-quinoid magnets but also other variables such as inter-layer distance.

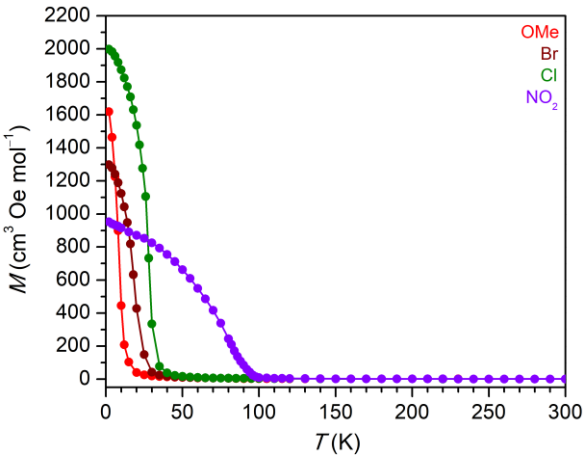

Figure 2.6. Variable-temperature field cooled magnetization data for **2** (red), **3** (brown), **4** (green), and **5** (purple) collected under an applied field of 10 Oe.

To more precisely determine the T_c, ac magnetic susceptibility in the absence of an applied dc field for **2**–**5** was collected (**Figure 2.S2**). Compounds **2**–**5** all display a frequency-dependent peak in both the in-phase (χ') and out-of-phase (χ'') susceptibilities that is consistent with glassy magnetic behavior.[116] This behavior most likely arises from magnetic frustration due to

the existence of both $^{R}L^{2-}$ and $^{R}L^{3\bullet-}$ within the materials. The magnetic ordering temperature was determined by the initial deviation from zero in the out-of-phase susceptibility for each framework. The compounds order at T_c = 16 K, T_c = 22 K, T_c = 30 K, and T_c = 90 K for **2**–**5**, respectively.

The observed trend in T_c is surprising as it stands in opposition to previous studies conducted on extended solids containing dianionic benzoquinoid ligands.[111] We hypothesize that the major factor affecting the magnetic ordering within **2**–**5** is the overall oxidation state of the framework. The large increase in T_c observed for **5** likely results from a higher concentration of $^{NO2}L^{3\bullet-}$ due to reduction of $^{NO2}L^{2-}$ via the HCO_2^- ion. This would lead to stronger, more homogenous coupling throughout the material, therefore raising its T_c. An inverse effect most likely operates within **2** as it contains a higher percentage of $^{OMe}L^{2-}$. Therefore, while these results demonstrate that the functional group attached to the bridging-semiquinone ligand has a quantifiable effect on the observed magnetic properties, further experiments are needed to separate the effect due to resonance and induction and the effect due to modulation of the overall oxidation state of the synthesized material.

2.3 Conclusions

We have reported the synthesis, characterization, and magnetic properties of a series of 2D iron-quinoid MOF magnets with the general formula $(Me_4N)_2Fe_2{}^{R}L_3$ (R = OMe, Br, Cl, or NO_2). All the materials have been shown to undergo *in situ* electron transfer from Fe^{II} to $^{R}L^{2-}$ such that they contain the radical semiquinone ligand $^{R}L^{3\bullet-}$ in varying amounts. DC magnetization and ac susceptibility showed that the magnetic ordering temperature of each framework can be tuned via changing the organic substituent on the semiquinone bridging ligand. However, the intrinsic effect of the ligand substituent on the observed T_c could not be deconvoluted from the difference in the

relative oxidation state of the frameworks. Nevertheless, the above work highlights the high degree of magnetic tunability that iron-quinoid magnets exhibit.

2.4 Experimental Method and Supplementary Materials

2.4.1 General Methods

Unless otherwise noted, all manipulations were conducted under a humid dinitrogen atmosphere in an MBraun LABstar or Vacuum Atmospheres Nexus II glovebox or using standard Schlenk techniques. All commercially available chemicals and reagents were purchased and used without further purification unless otherwise stated. DMF was dried using a commercial solvent purification system purchased from JC Meyer Solvent Systems and deoxygenated under a stream of argon prior to use, and Milli-Q water was deoxygenated via three cycles of freeze-pump-thaw degassing prior to use. Sodium nitranilate[117] and $(Me_2NH_2)_2[Zn_2{}^{Cl}L_3]\bullet 2H_2O\bullet 6DMF$[108] were synthesized according to previous methods. Powder X-ray diffraction (PXRD) was collected at room temperature on a STOE-STADI-P powder diffractometer equipped with an asymmetric curved Germanium monochromator (CuKα1 radiation, λ = 1.54056 Å) and one-dimensional silicon strip detector (MYTHEN 21K and DECTRIS). The line focused Cu X-ray tube was operated at 40 kV and 40 mA. Powder was packed in a 3-mm metallic disk purchased from STOE and sandwiched between two layers of polyimide tape. Diffraction data were collected from 5 to 55° 2θ over 10 min. The instrument was calibrated against a NIST silicon standard (640d) prior to measurement.

2.4.2 Syntheses

2.4.2.1 Frameworks $(Me_4N)_2Fe_2{}^{OMe}L_3$ (2), $(Me_4N)_2Fe_2{}^{Br}L_3$ (3), and $(Me_4N)_2Fe_2{}^{Cl}L_3$ (4)

$Fe(BF_4)_2 \cdot 6H_2O$ (24.2 mg, 0.0717 mmol, 1 eq), methoxanilic, chloranilic, or bromanilic acid precursor (0.0717 mmol, 1 eq), respectively, and tetramethylammonium tetrafluoroborate (46.2 mg, 0.287 mmol, 4 eq) were combined in DMF (2 mL) to afford green-black suspensions. The mixtures were heated to 130 °C to afford green-black, hexagonal plate crystals. After 2 days, the reaction mixtures were cooled to room temperature, and the mother liquor decanted via pipette. The crystals were then washed with DMF (4 x 5 mL) prior to being stored under 5 mL of DMF.

2.4.2.2 Frameworks $(Me_4N)_2Fe_2^{NO}{}_2L_3$ (5)

$Fe(BF_4)_2 \cdot 6H_2O$ (24.2 mg, 0.0717 mmol, 1 eq), sodium nitranilate (19.6 mg, 0.0717 mmol, 1 eq), and tetramethylammonium tetrafluoroborate (46.2 mg, 0.287 mmol, 4 eq) were combined in DMF (2 mL) and H_2O (25 μL) to afford a green-black suspensions. The mixture was heated to 130 °C for 2 days to afford green-black crystals suitable for X-ray crystallographic analysis. The reaction mixture was then cooled to room temperature. Once cool, the mother liquor was decanted from the crystals via pipette, and the crystals washed with DMF (4 x 5 mL) prior to being stored under 5 mL of DMF.

2.4.3 X-ray Structure Determination

Single crystals of **3**, **4**, and **5** suitable for X-ray analysis were coated with deoxygenated Paratone-N oil and mounted on a MicroMounts rod. The crystallographic data were collected at 250 K on a Bruker APEX II diffractometer equipped with a Cu Kα microsource. The temperature of the crystals was controlled with an Oxford Cryosystems low-temperature device. Data reduction was performed with the Bruker SAINT software package using a spherical adsorption correction. The structure was solved with the ShelXT[118] structure solution program using the Intrinsic Phasing

solution method and Olex2[119] as the graphical interface. The model was refined with ShelXL[120] using least squares minimization.

2.4.4 Raman Spectroscopy

Crystals of **2**–**5** were deposited onto a silicon oxide-coated silicon wafer and sealed in a Linkam THMS350 V microscope state. Raman spectra were collected using a Horiba LabRam HR evolution confocal microscope. Individual crystals were excited with a 473 nm continuous-wave diode laser at 263 μW power equipped with a long working distance 50X microscope objective (NA = 0.50; Nikon) and 1800 grooves/mm grating.

2.4.5 Mössbauer Spectroscopy

Mössbauer spectra for **2**–**5** were collected with a constant acceleration spectrometer and a cobalt-57 rhodium source. The spectrometer was calibrated at 295 K with α-iron foil. Samples were prepared in a dinitrogen-filled glovebox, covered in deoxygenated Paratone-N oil, and frozen in liquid nitrogen prior to handling in air. Spectra of **3** and **4** were collected at 80 K. Samples of **2** were collected at 20, 30, 50, and 80 K. Samples of **5** were collected at 120 K. All spectra were analyzed using the WMOSS Mössbauer Spectral Analysis Software (www.wmoss.org).

2.4.6 Magnetic Measurements

Magnetic measurements of **2**–**5** were performed on polycrystalline samples flamed-sealed within a quartz sample tube under 1 mL of degassed DMF. All data were collected using a Quantum Design MPMS-XL SQUID magnetometer from 1.8 to 300 K at applied dc fields ranging from 0 to +7 T. Ac magnetic susceptibility data were collected under an ac field of 4 Oe, oscillating at frequencies between 1–997 Hz. Dc susceptibility data were corrected for diamagnetic contributions from the core diamagnetism of each sample estimated using Pascal's constants.[121]

The magnetic ordering temperatures for **2**–**5** were determined from the initial deviation from the baseline within the χ_M'' as plotted versus temperature.

2.4.7 Powder X-ray Diffractograms

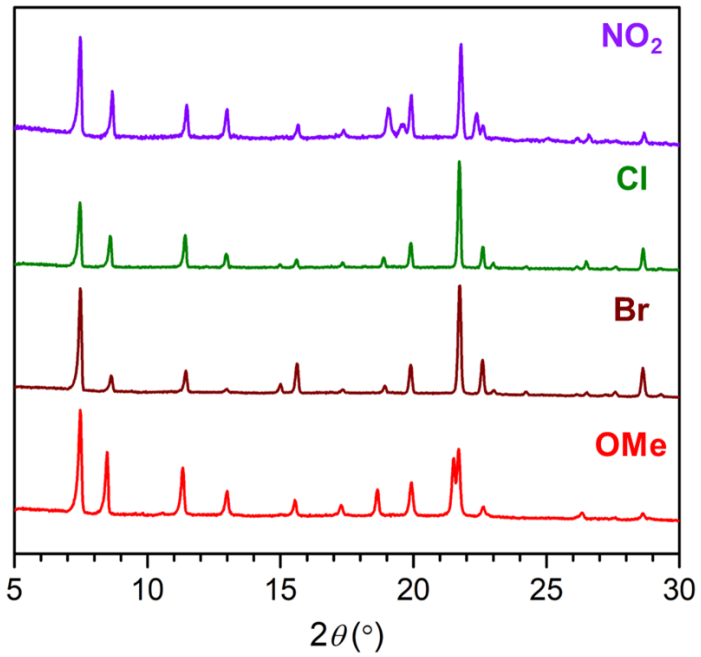

Figure 2.S1. Powder X-ray diffractograms of **2** (red), **3** (brown), **4** (green), and **5** (purple) between 5–30° 2θ.

2.4.8 Crystallographic Tables

Table 2.S2. Crystallographic Data for 3, 4, and 5

	3	*4*	*5*
Empirical Formula	$C_{13}H_{12}Br_3FeNO_6$	$C_{13}H_3Cl_3FeNO_6$	$C_{13}H_{12}FeN_4O_{12}$
Formula Weight	573.8	431.16	472.11
Temperature / K	250.0	250.0	249.99
Crystal System	trigonal	trigonal	trigonal
Space Group	P−31m	P−31m	P−31m
a / Å	13.6046(10)	13.5717(18)	13.5957(6)
b / Å	13.6046(10)	13.5717(18)	13.5957(6)
c / Å	10.100(10)	9.9759(18)	10.0513(5)
α / °	90	90	90
β / °	90	90	90
γ / °	120	120	120
Volume / Å^3	1618.9(3)	1591.3(9)	1609.00(16)
Z	2.00004	2	2.00004
ρ_{calc} / g cm^{-3}	1.177	0.900	0.974
μ / mm^{-1}	8.224	6.270	4.166

F(000)	552.0	426.0	480.0
Crystal size / mm^3	0.098 × 0.077 × 0.05	0.306 × 0.157 × 0.014	
Radiation	Cu Kα (λ = 1.54178)	Cu Kα (λ = 1.54178)	Cu Kα (λ = 1.54178)
2θ Range for Data Collection / °	8.754 to 101.006	7.522 to 100.716	7.508 to 111.48
Index Ranges	−13 ≤ h ≤ 13 −13 ≤ k ≤ 10 −10 ≤ l ≤ 10	−9 ≤ h ≤ 9 −7 ≤ k ≤ 13 −9 ≤ l ≤ 9	−6 ≤ h ≤ 12 −13 ≤ k ≤ 7 −10 ≤ l ≤ 10
Reflections Collected	8052	2207	3180
Independent Reflections	628 [R_{int} = 0.0375, R_{sigma} = 0.0184]	613 [R_{int} = 0.666, R_{sigma} = 0.0634]	756 [R_{int} = 0.0289, R_{sigma} = 0.0265]
Data/Restraints/Parameters	628/13/49	613/19/48	756/54/80
Goodness-of-fit on F^2	1.126	1.069	1.022
Final R indexes [I>=2σ (I)]	R_1 = 0.0712, wR_2 = 0.2406	R_1 = 0.0965, wR_2 = 0.2530	R_1 = 0.0670, wR_2 = 0.1946
Final R indexes [all data]	R_1 = 0.0751, wR_2 = 0.2480	R_1 = 0.0965, wR_2 = 0.2530	R_1 = 0.0740, wR_2 = 0.2025
Largest diff. peak/hole / e Å^{-3}	1.57/−0.90	0.75/−0.53	0.24/−0.29

2.4.9 Variable-Temperature Ac Magnetic Susceptibility

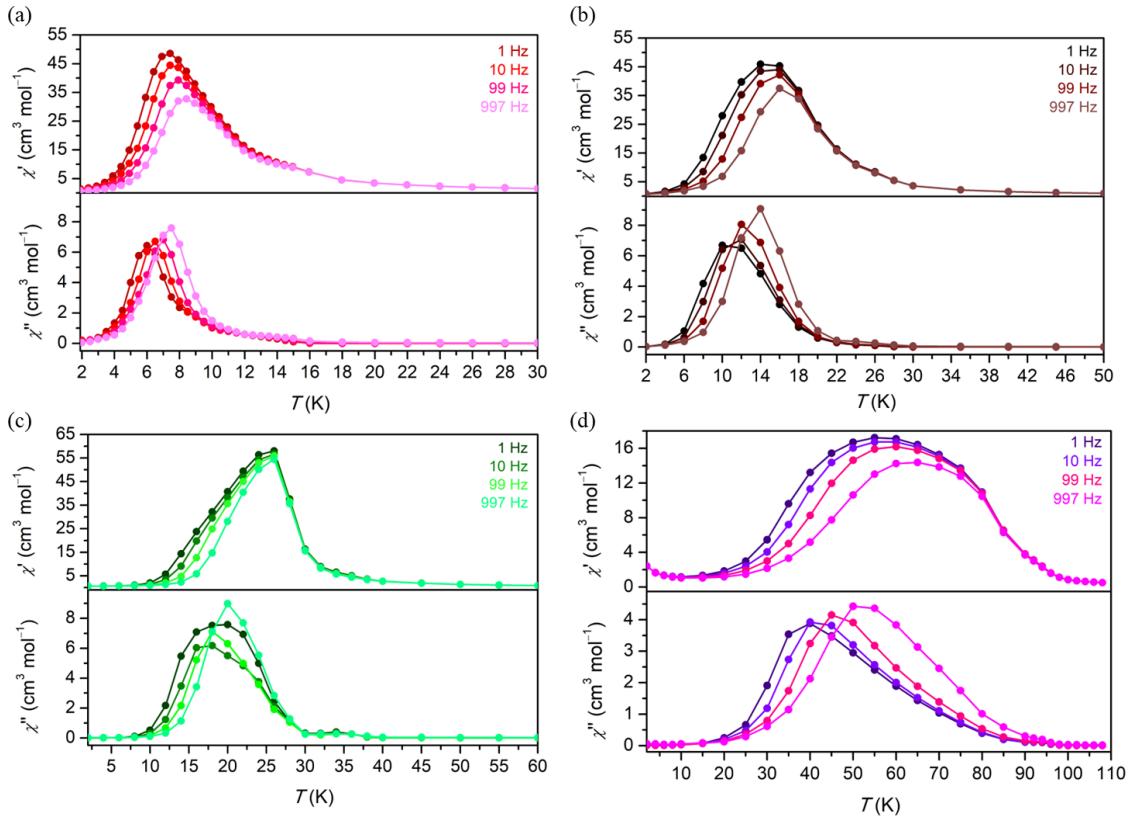

Figure 2.S2. Variable temperature in-phase (χ') and out-of-phase (χ'') ac magnetic susceptibility of (a) **2**, (b) **3**, (c) **4**, and (d) **5** collected at 1, 10, 99, and 997 Hz.

Chapter 3

Structurally Dynamic 1D Coordination Polymers Enabled via the Weak-Link Approach

The work presented in this chapter is based upon the following published work:

Coleman, B. D.; d'Aquino, A. I.; Kean, Z.; Wang, Y.; Hedlund Orbeck, J. K.; Stern, C. L. Mirkin, C. A. Structurally dynamic 1D coordination polymers enabled via the Weak-Link Approach. *Polyhedron* **2022**, *227*, 116116.

The numbers, symbols, and other notations used to present chemical structures are self-contained in this chapter.

3.1 Introduction

Supramolecular interactions are the basis for primary, secondary, and tertiary structures of many biological macromolecules (*e.g.*, proteins). These network interactions permit allosteric regulation, govern stimuli response (*e.g.*, from molecular effectors), and dictate molecular properties.[122-125] Drawing on design principles that occur in nature, researchers have sought to build abiotic architectures with similar features and use them as a basis for next-generation functional materials. To date, many approaches in the field of coordination-driven supramolecular chemistry have been pursued to prepare chemical moieties that vary in their synthetic complexity and applicability.[55, 56, 63, 126-140]

In the context of coordination chemistry, the Weak-Link Approach (WLA) has emerged as a powerful method to synthesize supramolecular structures that exhibit allosteric regulation.[58, 65, 141] The WLA relies on hemilabile bidentate ligands that feature two moieties with distinct coordination strengths—a coordinatively inert "strong link" (*e.g.*, phosphino- or *N*-heterocyclic carbenes) and a coordinatively labile "weak link" (*e.g.*, ether, amino, thioether). Upon reaction with a d^8 transition metal precursor (*e.g.*, Rh^I, Ir^I, Pd^{II}, Pt^{II}), a condensed, square-planar structure is formed. When the square planar complexes are exposed to halide[73, 76, 77, 84, 142] (*e.g.*, Cl^- and I^- anions), small molecule effectors[70, 75, 82, 83, 85] (*e.g.*, CO, CH_3CN, amines) or oxidizing/reducing

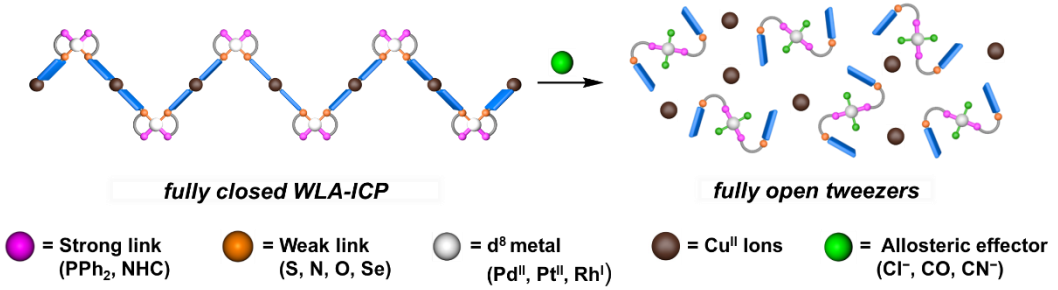

Figure 3.1. The Weak-Link Approach to Supramolecular Chemistry utilizes hemilabile ligands coordinated to d^8 transition metal ions to generate a toggleable structural node. Upon exposure to chemical and physical stimuli, small molecule or anionic effectors preferentially displace the more labile "weak-link", resulting in a more open, flexible structure.

pendant functionalities[68, 143-149] (*e.g.*, oxidation and reduction of appended ferrocene moieties), the "weak link" is preferentially displaced, allowing the structure to toggle between different structural states (e.g. fully closed, semi-open, and fully open) (**Figure 3.1**). Using the WLA, a variety of supramolecular structures can be accessed, including molecular tweezers,[76-79] macrocycles,[70, 73, 75, 80-85] and tri-layer structures[86-89]. The modularity, tailorability**,** and stimuli-responsiveness achieved through the WLA has enabled the design of stimuli-responsive catalysts,[86, 87] signal amplifiers,[80, 81] fluorescent probes,[78, 79] and light-harvesting materials[88, 89].

Infinite coordination polymers (ICPs), which consist of multidentate ligands interconnected via coordination to metal ions to form 1D, 2D, or 3D architectures, represent another promising class of supramolecular materials for the design of stimuli-responsive and abiotic allosteric systems due to their high degree of tunability and ability to be rationally designed.[126, 150-152] We hypothesized that by adding pendant functional groups onto the hemilabile ligands that allow for coordination to a secondary metal binding unit (SBU), a new type of WLA monomer complex could be synthesized and polymerized to form stimuli-responsive ICPs. Due to the modularity of the WLA platform, these monomer complexes could be easily adapted to respond to a range of stimuli or display a variety of functions in the resulting ICPs. Previously, we reported the design and synthesis of stimuli-responsive WLA-based ICP particles.[90] In this work, a WLA monomer complex featuring pendant terpyridine moieties was polymerized in the presence of Fe^{II} to form amorphous ICP particles. Importantly, this work demonstrates that localized changes to the structure of the embedded WLA monomers regulates the assembly of an extended solid, which can be applied to dictate the chemical and physical properties of an extended ICP material. However, the amorphous nature of the particles precluded a complete crystallographic analysis of the structural transformation induced upon chemical effector binding (*e.g.*, Cl^- anion), and the

extended structure of the material could only be investigated indirectly, thus limiting our ability to identify unambiguous design criterion for the synthesis and characterization of WLA-based ICPs (WLA-ICPs).

Herein, in order to permit further structure-function investigations, we designed, synthesized, and crystallographically characterized three WLA-ICPs. We hypothesized that exchanging the terpyridine moiety for a more coordinately labile functional group (*i.e.*, pyridine) would allow for the controlled assembly of a crystalline solid, while avoiding the formation of kinetically driven, amorphous ICP particles. The reaction of the Pd^{II}-phosphino-thioether(P,S)-based WLA monomer complex with a Cu^{II} precursor ($Cu(BF_4)_2 \bullet 6H_2O$) in a variety of solvents leads to the formation of three independent, but closely related, 1D zig-zag chain compounds, primarily differing in the bound solvent completing the Cu^{II} coordination sphere. We observe that these WLA-ICPs retain the characteristic stimuli-responsiveness of the WLA platform, even after the formation of an extended structure. When representative WLA-ICP crystals were exposed to a Cl^- anion solution, the extended structure disassembles as Cl^- binds to the Pd^{II} node of the embedded WLA monomer complex. In this way, one can control crystallization and assembly simply by toggling the structural state of the WLA monomer. Taken together, the three new WLA-ICP chain compounds pursued in this work expand the scope of supramolecular architectures accessible via the WLA platform, and also lay a foundation for a new class of allosteric, stimuli-responsive coordination polymers.

3.2 Results and Discussion

3.2.1 Synthesis and characterization of 3^{MeCN}, 3^{DMF}, and 3^{H_2O}

A primary goal of this work was to use the WLA to synthesize crystalline forms of ICPs, so their extended structures could be studied crystallographically. We view this as a first step

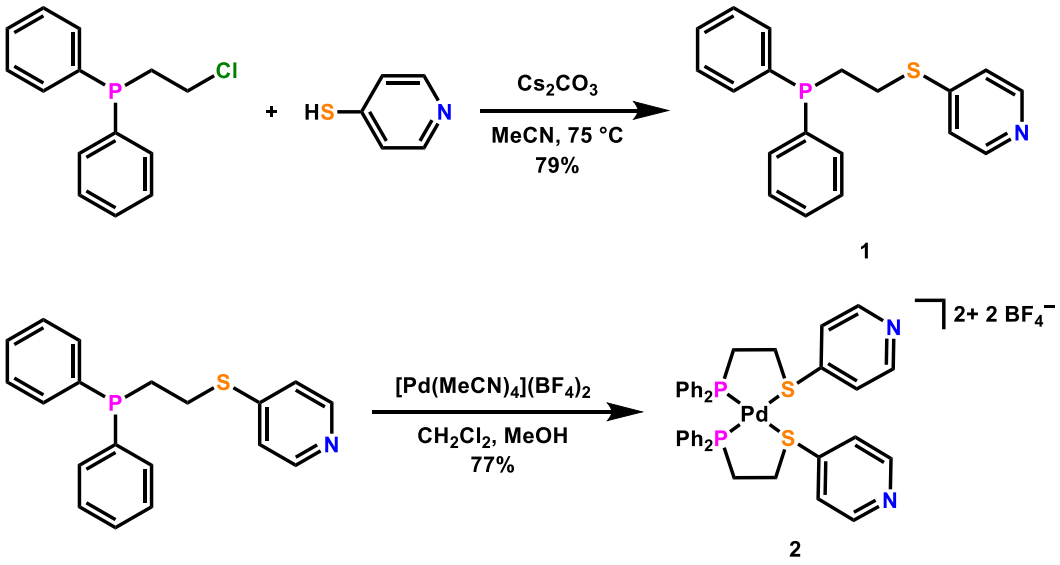

Scheme 3.1. The synthesis of molecular complex $[Pd(P,S\text{-}pyr)_2][BF_4)_2]$ (**2**).

toward understanding how to move the WLA system towards higher dimensional extended solids, including metal organic frameworks (MOFs). We hypothesized that, by utilizing a more coordinatively labile pyridine moiety (K_a ~ 10^4 to Cu^{II}),[153, 154] as opposed to the previously employed terpyridine moiety (K_a ~ 10^8 to Fe^{II}),[155] the formation of kinetically trapped amorphous ICP particles would be less likely and an extended, crystalline material could be obtained. To test this hypothesis, a Pd^{II}-based WLA coordination complex featuring a hemilabile P,S ligand appended with coordinating pyridine functionalities (P,S-pyr, **1**) was prepared, and characterized by NMR (**Scheme 3.1**).

Given the high affinity of Cu^{II} for pyridine and the variety of crystalline ICP structure-types accessible via Cu^{II}-pyridine coordination, we studied the interaction of Cu^{II} metal ions in the presence of monomer complex **2** (**Figure 3.2a**).[156-163] Single-crystal X-ray diffraction (SCXRD) was used to confirm that the WLA-based ICP $\mathbf{3}^{MeCN}$ crystallizes in the monoclinic centrosymmetric space group *P*2/n. Each WLA subunit is coordinated to one crystallographically unique Cu^{II} metal center to form an alternating 1D linear chain with a zig-zag-like crystal packing (**Figure 3.2b,**

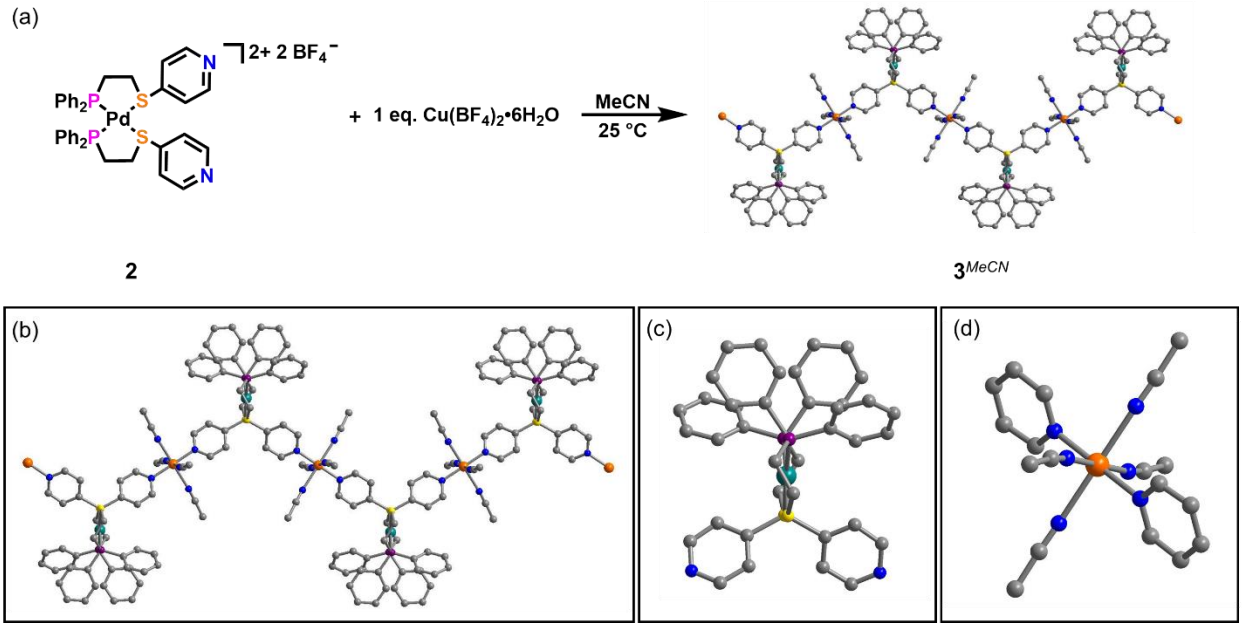

Figure 3.2. (a) Synthesis of coordination polymer $\mathbf{3}^{MeCN}$. X-ray crystal structure of $\mathbf{3}^{MeCN}$ highlighting (b) the full linear chain, (c) the closed WLA coordination node, and (d) the Cu^{II} coordination sphere. Orange, green, purple, yellow, blue, and grey spheres represent Cu, Pd, P, S, N, and C atoms, respectively. Charge balancing counter ions and H atoms have been omitted for clarity.

Table 3.S1, Figure 3.S1). The Pd^{II} node in each WLA subunit adopts a strained square planer geometry, and the bond angles are described in **Table 3.S2** (**Figure 3.2c**). The Pd1–S1–N1 bond angle of 105.83(5)° gives the compound a distinctive zig-zag structure. The Cu^{II} SBU assumes an octahedral geometry, where two pyridine moieties from independent WLA subunits adopt a *trans* configuration (**Figure 3.2d**), and the remaining Cu^{II} coordination sites are filled with bound MeCN solvent. As is common to many Cu^{II} octahedral compounds, the axially bound MeCN molecules are significantly tetragonally distorted (**Table 3.S3.**). Finally, the cationic ICPs are charge balanced by disordered $[BF_4]^-$ anions that reside in the limited interchain region. When DMF is substituted for MeCN as the solvent and Et_2O is allowed to subsequently diffuse into the reaction mixture, green, block crystals of WLA-ICP $\mathbf{3}^{DMF}$ are accessed (**Figure 3.3a–c, Table 3.S1–S3**). After solvent substitution and diffusion, $\mathbf{3}^{DMF}$ crystallizes in the *P*2/n space group, confirming that this system prefers to form 1D zig-zag chains.

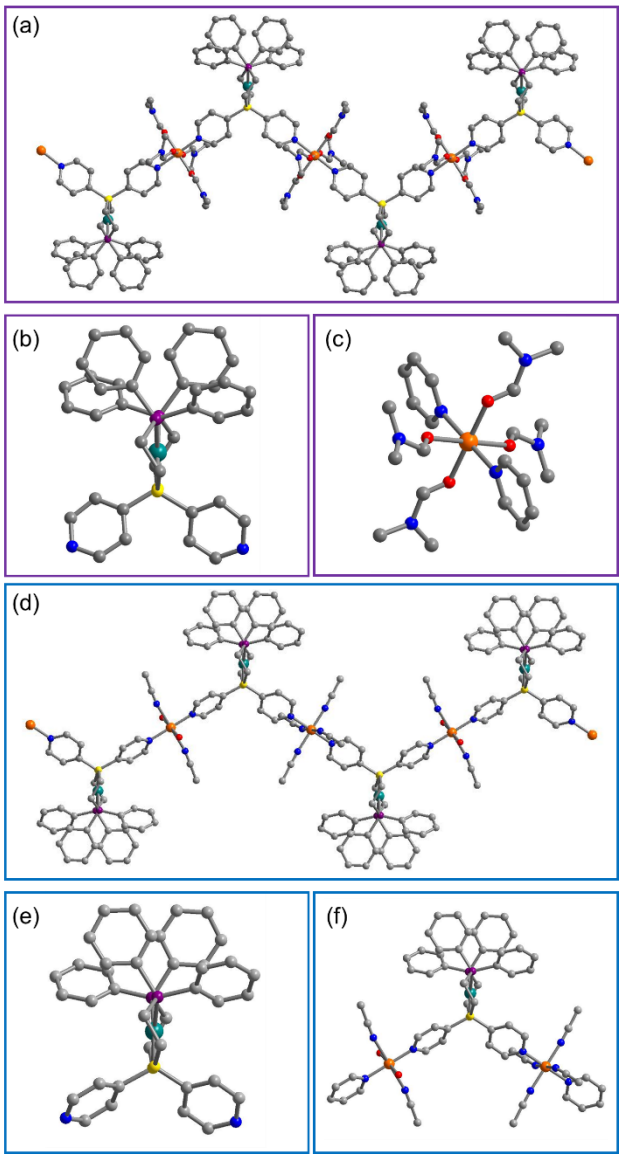

Figure 3.3. (a) X-ray crystal structure of $\mathbf{3}^{DMF}$ highlighting the full linear chain, (b) the closed WLA coordination node, and (c) the Cu^{II} coordination sphere. (d) X-ray crystal structure of $\mathbf{3}^{H2O}$ highlighting the full linear chain, (e) the closed WLA coordination node, and (f) the asymmetric unit including the complete coordination spheres of Pd^{II} and the two crystallographically unique Cu^{II} sites. Orange, green, purple, yellow, red, blue, and grey spheres represent Cu, Pd, P, S, O, N, and C atoms, respectively. Charge balancing counter ions, unbound solvent molecules, and H atoms have been omitted for clarity. Modelled rotational disorder of the bound DMF molecules has been omitted for clarity.

By simply changing the equivalents of Cu^{II} in the reaction mixture, a closely related, yet independent, structure was obtained. $\mathbf{3}^{H2O}$ crystallizes in the monoclinic centrosymmetric space group $P2_1/n$ and, consistent with $\mathbf{3}^{MeCN}$ and $\mathbf{3}^{DMF}$, forms 1D zig-zag chains (**Figure 3.3d, Table 3.S1**). Again, the WLA subunit displays a strained square-planar geometry around the Pd^{II} node (**Figure 3.3e, Table 3.S2**). However, unlike the other structures, $\mathbf{3}^{H2O}$ possesses two crystallographically independent octahedral Cu^{II} SBUs in its asymmetric unit (**Figure 3.3f**). The first Cu1 coordination sphere features two *trans* pyridine moieties, two *trans* water molecules, and *two axial, trans* acetonitrile molecules. As with $\mathbf{3}^{MeCN}$ and $\mathbf{3}^{DMF}$, $\mathbf{3}^{H2O}$ features a tetragonal distortion of the MeCN ligands (**Table 3.S3**). The second Cu2 coordination sphere features two *trans* pyridine moieties and MeCN completes its coordination sphere, and again, features a tetragonal distortion of the bound MeCN molecules. Together, these structures represent the first

three crystallographically characterized WLA-based ICPs and show that by carefully controlling the coordination strength of the pendant functionalities to transition-metal-based SBUs, closed WLA complexes can be assembled into crystalline extended structures.

3.2.2 Solvent Effects on the Structure of $\mathbf{3}^{MeCN}$

Next, the WLA subunit's ability to modulate the structure of an extended solid upon chemical effector binding was studied; specifically, the stimuli responsiveness of $\mathbf{3}^{MeCN}$ in solution was explored. To ensure that any structural transformations arose primarily from chemical changes to the WLA metal node and not from solvent effects, the solution structure and solvent stability of the synthesized crystals in MeCN was investigated. Due to challenges growing high quality crystals in bulk quantities for $\mathbf{3}^{DMF}$ and $\mathbf{3}^{H2O}$, we focused the remainder of our analysis on $\mathbf{3}^{MeCN}$ given the ease in which robust crystals of this compound could be grown.

To understand the size and length of the $\mathbf{3}^{MeCN}$ structure in solution, DOSY measurements were performed. The DOSY spectrum of monomer complex **2** revealed a diffusion coefficient range of D = 0.922–1.01×10^{-5} cm^2/sec by fitting to individual proton resonances (**Figure 3.4a, Figures 3.S3**–**3.S8**). Compound $\mathbf{3}^{MeCN}$ was found to have a smaller diffusion coefficient D = 6.75–7.17×10^{-6} cm^2/sec, consistent with $\mathbf{3}^{MeCN}$ having a larger oligomeric structure in comparison to **2** (**Figure 3.4b**, **Figure 3.S9**–**3.S12**). In agreement with the DOSY measurements, the ESI-MS spectrum of $\mathbf{3}^{MeCN}$ showed distinct peaks up to 2168.40 *m*/*z* (**Figure 3.S25).** These results indicate $\mathbf{3}^{MeCN}$ is a distinct species from **2** and, while an ICP in the solid state, is oligomeric (*i.e.*, dimers, trimers) when dissolved into solution via sonication for NMR analysis.

In order to distinguish the solvent contributions from chemical effector (Cl^- anion) exposure, the long-term stability (*i.e.*, over several days) of single crystals of $\mathbf{3}^{MeCN}$ in MeCN was investigated. The first $^{31}P\{^1H\}$ NMR spectrum obtained during this study was consistent with the

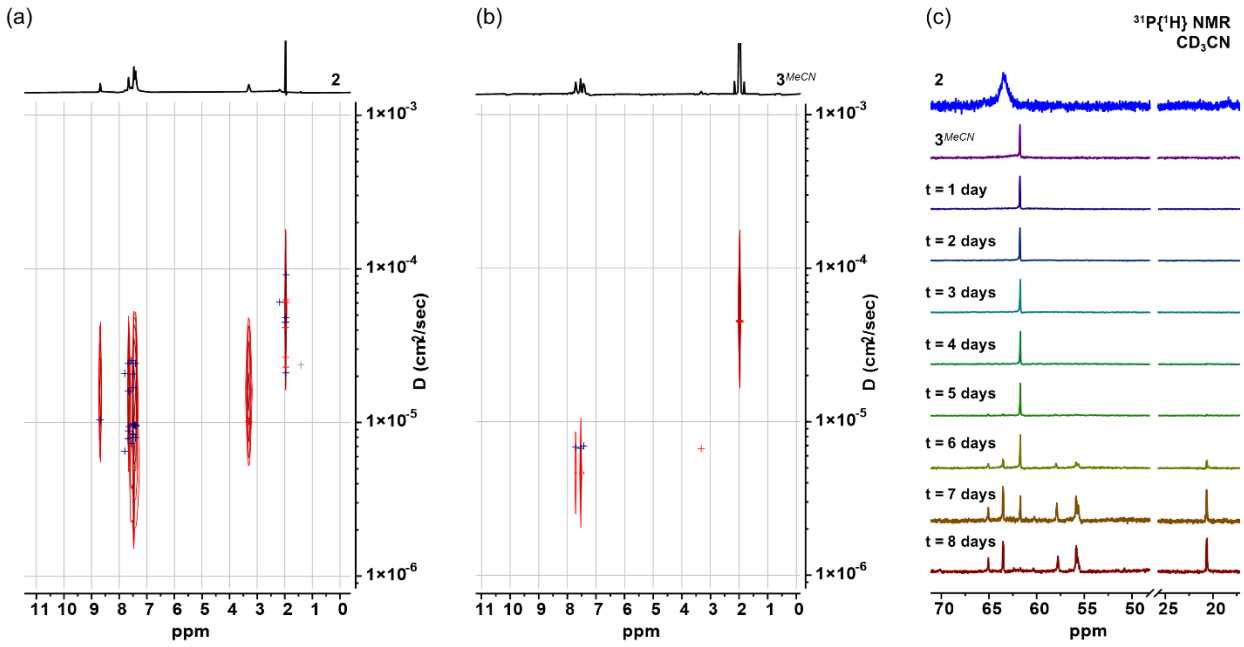

Figure 3.4. Psuedo-2D DOSY NMR of (a) **2** and (b) **3**^{MeCN}. (c) $^{31}P\{^{1}H\}$ NMR spectra of a mixture containing crystals of **3**^{MeCN} soaked in 1 gram of solvent in an air-tight NMR tube over the course of 8 days, showing the degradation of the coordination polymer in solution. All spectra were collected in CD_3CN.

initial spectrum observed during the characterization of the solution structure of **3**^{MeCN} (**Figure 3.4c, Figure 3.S13**, **3.S14**). After 4 days, the crystals of **3**^{MeCN} fully dissolved into the deuterated MeCN solution and the first signs of degradation were observable in the $^{31}P\{^{1}H\}$ spectrum on the fifth day. This degradation continues over the course of the next three days (8 days in total) as **3**^{MeCN} fully degrades into a combination of products. The DOSY and degradation experiments illustrate two important behaviors of **3**^{MeCN} that are relevant to subsequent studies: (1) **3**^{MeCN} is an oligomer in solution, and (2) single crystals of **3**^{MeCN} do not degrade sufficiently or quickly enough that changes in structure during the reaction with Cl^- anions can be attributed to solvent effects alone.

3.2.3 Structural Dynamics in the Presence of Cl^-

A key feature of the WLA is its ability to be used to induce structural transformations in supramolecular materials upon small molecule or halide effector binding. After establishing the

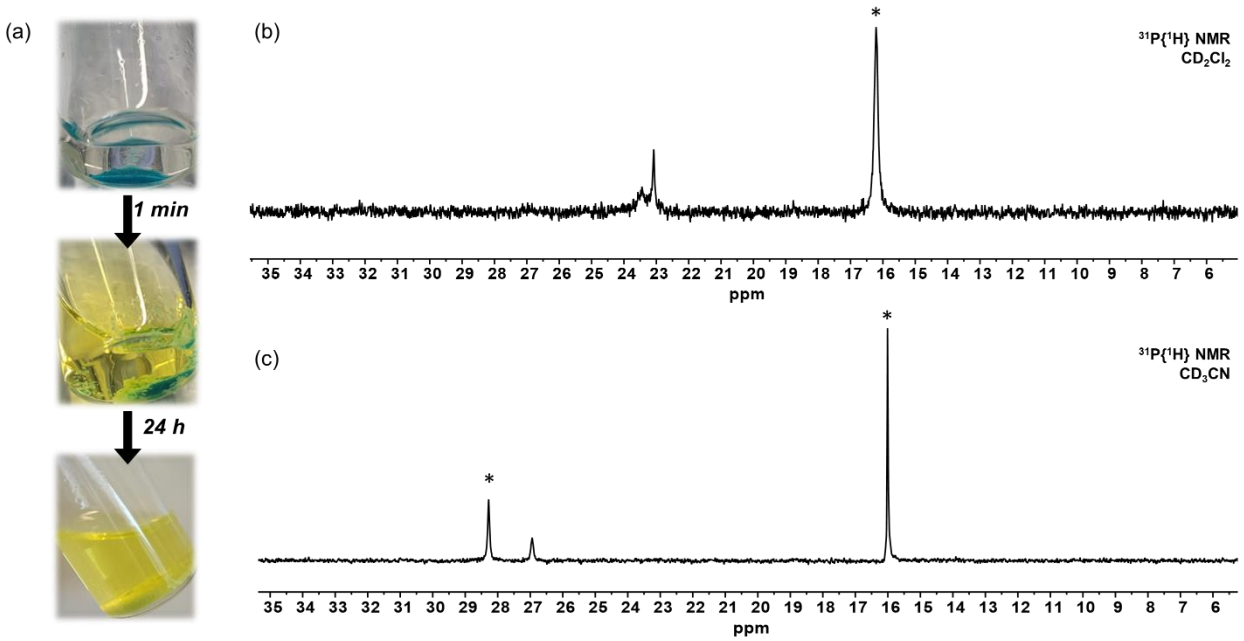

Figure 3.5. Crystals of $\mathbf{3}^{MeCN}$ were exposed to excess Cl^- ions to induce a structural transformation of the WLA complex node, resulting in disassembly of the linear coordination polymer. (a) Within one minute of exposure to a Cl^- ion solution, crystals of $\mathbf{3}^{MeCN}$ begin to swell and transform into a white powder. Allowing this mixture to stand for 24 hours results in complete reaction of $\mathbf{3}^{MeCN}$. (b) $^{31}P\{^{1}H\}$ NMR spectrum of the white solid obtained after 24 hours. (c)$^{31}P\{^{1}H\}$ NMR spectrum of the yellow supernate showing a mixture of $\mathbf{2}^{2Cl}$,$\mathbf{2}^{2MeCN}$, and other products in CD_3CN. Asterisks denote assigned species.

stability of $\mathbf{3}^{MeCN}$ crystals in MeCN, we investigated their response to Cl^- anion exposure. Upon exposure to the Cl^- solution, the mother liquor turned from colorless to yellow, and within one minute, the blue-green crystals began to expand and turn into an amorphous white powder, consistent with the lack of signal in the PXRD diffractogram (**Figure 3.5a**, **Figure 2.S2**); the transformation was complete after 24 hours, as determined by the disappearance of the $^{31}P\{^{1}H\}$ NMR resonance of the chain compound in solution. The two products (*i.e.*, yellow supernatant, and white powder) were both analyzed by ^{1}H and $^{31}P\{^{1}H\}$ NMR spectroscopy. In the $^{31}P\{^{1}H\}$ NMR spectrum of the crude white powder, the signal at approx. 16 ppm is assigned to the fully open complex $\mathbf{2}^{2Cl}$ (**Figure 3.5b, 3.6**), which is consistent with data from isoelectronic model compounds.[28, 33, 74] The resonance at approx. 16 ppm in the $^{31}P\{^{1}H\}$ NMR spectrum of the yellow

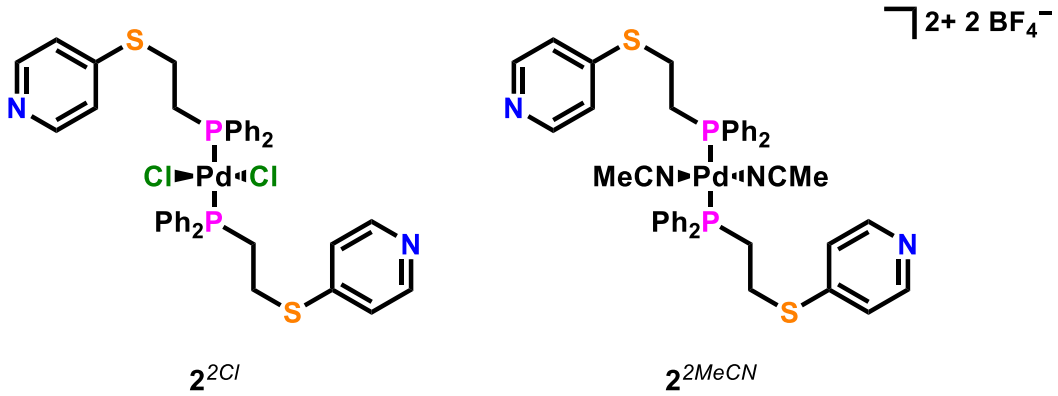

Figure 3.6. Fully open congeners of 2, 2^{2Cl} and 2^{2MeCN}.

solution is assigned to the fully open congener of complex $\mathbf{2}^{2Cl}$, and the resonance at approx. 28 ppm is assigned to a related fully open species in which the complex is coordinated by two MeCN solvent molecules ($\mathbf{2}^{2MeCN}$, **Figure 3.5c, 3.6**), consistent with model complexes from the literature.[75, 77, 164] Given that the crude reaction mixtures were analyzed *in situ* to capture all reaction products, these analyses resulted in signals in the NMR spectra that we were unable to fully assign (**Figure 3.5b**,**c**, **3.S15–3.S18**). Attempts to grow crystals suitable for structure determination from the reaction mixtures were unsuccessful. Nevertheless, the *in situ* NMR experiments suggest that upon exposure to Cl^- anion, the embedded WLA subunits of $\mathbf{3}^{MeCN}$ begin to open as the halide binds to the Pd^{II} metal centers and along the chain backbone. This structure of the sample transforms from crystalline to amorphous, leading to the complete consumption of the chain crystals, and yielding a mixture of fully open WLA complexes and other products. These experiments demonstrate that even in a rigid, crystalline system, the WLA can be used to impart stimuli-responsiveness into supramolecular structures and control the assembly and switching of metalloligands between an extended structure and molecular monomers.

From this data, coupled with SCXRD structures, we postulate a design criterion for next-generation WLA-ICPs: increasing the coordination strength between the WLA monomer and the transition metal SBU will yield materials that maintain crystallinity through the structural

transformation. Moving forward, one could envision a WLA-based ICP that could be switched between two crystalline phases to permit the development of design rules for next generation stimuli-responsive materials.

3.3 Conclusions

We have reported the first three crystallographically characterized WLA-ICPs. Importantly, we have demonstrated that in their closed state and in the absence of chemical effectors, WLA coordination complexes are rigid enough to form extended crystalline solids. The subsequent introduction of WLA chemical effectors to the crystals allows for their disassembly to molecular components. Thus, one can control macro-scale molecular assembly via the structural state of the nanoscale WLA monomer complex. The structural insight gained through X-ray diffraction will permit the design and synthesis of future WLA-ICP materials, and our structural and chemical analysis has highlighted that appropriate coordination strength should be considered when using WLA complexes to prepare stimuli-responsive extended structures.

3.4 Experimental Methods and Supplementary Materials

3.4.1 General Methods

Unless otherwise noted, all reactions and procedures were performed under a dinitrogen atmosphere in a Vacuum Atmospheres Nexus II glovebox or using standard Schlenk techniques. All commercially available chemicals and reagents were purchased and used without further purification, unless otherwise stated. 1,2-Dichloroethane, 0.5 M potassium diphenylphosphide solution in tetrahydrofuran, and tetra(*n*-butyl)ammonium chloride were purchased from Millipore-Sigma. 4-Mercaptopyridine was purchased from TCI America. Tetrakis(acetonitrile)palladium(II) tetrafluoroborate was purchased from Strem Chemical, and copper(II) tetrafluoroborate

hexahydrate was purchased from Alfa Aesar. Tetrahydrofuran (THF), diethyl ether (Et_2O), and dichloromethane (DCM) were dried using a commercial solvent purification system purchased from JC Meyer Solvent Systems and deoxygenated under a stream of argon prior to use. Anhydrous acetonitrile (MeCN) and anhydrous *N*,*N*-dimethylformamide (DMF) were purchased from Millipore-Sigma. Anhydrous methanol (MeOH) was purchased from Thermo Scientific. (2-Chloroethyl)diphenylphosphine was synthesized according to literature methods.[165] Filtrations were performed by gravity through a Whatman medium to fine mesh filter paper using a Büchner funnel. Flash chromatography was performed using a silica gel column (60 Å pore size, 230–400 mesh ASTM, 0.040–0.063 mm; Fluka). Vapor diffusion for crystal growth was conducted by sealing a culture tube containing 300 μL of the growth solution in a 20-mL scintillation vial containing approx. 4 mL of Et_2O. The sealed vial was allowed to stand in the glovebox at 25 °C during crystal growth. Sample sonication for NMR experiments were performed in a 25 °C water bath in a Branson Ultrasonic M2800 sonicator. Deuterated solvents (CD_2Cl_2, CD_3CN) were purchased from Cambridge Isotope Laboratories. ^1H, $^{31}P\{^1H\}$, and DOSY NMR spectra were collected on a Bruker Advance 400 MHz NMR spectrometer at 298 K under ambient conditions unless otherwise stated, and chemical shifts (δ) are given in parts per million (ppm). ^1H NMR spectra were referenced to residual solvent proton resonances (CD_2Cl_2 = δ 5.32; CD_3CN = δ 1.94), and $^{31}P\{^1H\}$ NMR spectra were indirectly referenced via ^{31}P gyromagnetic ratio. Electron-spray ionization mass spectrometry (ESI-MS) data were collected using a Bruker amaZon SL equipped with Hystar Version 3.2 data acquisition software. ESI-MS data were subsequently processed and analyzed using Compass Version 4.4. The mass spectrometer was configured with an Agilent 1100 Series HPLC module with an ESI source and 3D ion trap mass analyzer. The samples were analyzed with a 3-μL injection volume, and the mobile phase composition was 100% MeCN. Data

were collected in positive ion mode. High resolution mass spectra were obtained on an Agilent 6230 Time of Flight Mass Spectrometer attached to an Agilent 1200 series HPLC stack. Data were acquired on Agilent Mass Hunter Acquisition software and analyzed on Agilent Mass Hunter Qualitative Analysis software. Powder X-ray diffraction (PXRD) data were collected at room temperature on a STOE-STADI-P powder diffractometer equipped with an asymmetric curved Germanium monochromator (CuKα1 radiation, λ = 1.54056 Å) and one-dimensional silicon strip detector (MYTHEN 21K and DECTRIS). The line focused Cu X-ray tube was operated at 40 kV and 40 mA. Powder was packed in a 3-mm metallic disk purchased from STOE and sandwiched between two layers of polyimide tape. Diffraction data were collected from 5–55° 2θ over 10 min. The instrument was calibrated against a NIST silicon standard (640d) prior to measurement. CHN analysis was conducted by Midwest Microlab, LLC (Indianapolis, IN).

3.4.2 Syntheses

3.4.2.1 Hemilabile P,S-pyridine(pyr) Ligand (1).

Diphenyl((4-pyridyl)thioethyl)phosphine was synthesized via modification of literature procedures for previously reported analogous compounds.[58, 88, 166-168] In a glovebox under an inert atmosphere, (2-chloroethyl)diphenylphosphine (294.5 mg, 1.184 mmol), 4-mercaptopyridine (117.3 mg, 1.055 mmol), and cesium carbonate (674.3 mg, 2.070 mmol) were combined in 5 mL of MeCN in a 10-mL scintillation vial equipped with a magnetic stir bar. The vial was sealed with a cap and electrical tape, removed from the glovebox, and stirred at 75 °C overnight. Purification was then conducted under aerobic conditions. The reaction mixture was cooled to room temperature, filtered to remove cesium chloride and excess cesium carbonate, and the solvent was removed *in vacuo* to afford a yellow oil. The oil was purified by column chromatography on a silica gel using a 0–100% DCM/MeOH gradient, and the solvent was removed *in vacuo* to afford

the desired hemilabile ligand **1** as an off-white solid (268.6 mg, 79% yield). ^{1}H NMR (400 MHz, CD_2Cl_2) δ 8.33 (d, *J* = 5.4 Hz, 2H), δ 7.55–7.35 (m, 10H), δ 7.06–6.95 (m, 2H), δ 3.15–3.02 (m, 2H), δ 2.50–2.40 (m, 2H). ^{31}P{^{1}H} NMR (162 MHz, CD_2Cl_2) δ −17.32. MS (ESI+) *m*/*z* Calculated for [**1**+H]$^{+}$ $C_{19}H_{19}N_1P_1S_1$: 324.0976. Found: 324.10.

3.4.2.2 WLA Monomer Complex [Pd(P,S-pyr)$_2$][(BF$_4$)$_2$] (2).

Hemilabile ligand **1** (333.9 mg, 1.032 mmol) was dissolved in 2 mL of DCM and was added dropwise to a stirring slurry of tetrakis(acetonitrile)palladium(II) tetrafluoroborate (230.4 mg, 0.5186 mmol) in 2 mL of MeOH in a 10-mL scintillation vial. During the addition, a yellow precipitate was observed within minutes. The reaction was stirred overnight, and then the solution was removed from the glovebox and filtered, yielding a homogenous orange solution. Et_2O was added to the solution to precipitate a pale-yellow solid. The solid was collected via filtration, washed three times with excess Et_2O, and dried *in vacuo* resulting in the desired metal complex as a pale-yellow solid (375.5 mg, 77% yield). ^{1}H NMR (400 MHz, CD_3CN) δ 8.70 (s, 5H), δ 7.68–7.38 (m, br, 27H), δ 3.32 (s, br, 8H). ^{31}P{^{1}H} NMR (162 MHz, CD_3CN) δ 63.64. HR-MS (ESI+) *m*/*z* Calculated for [**2**−BF_4^-]$^{+}$ $C_{38}H_{36}BF_4N_2P_2PdS_2$: 839.0859. Found: 839.0893.

3.4.2.3 [Cu(Pd(P,S-pyr)$_2$)(MeCN)$_4$][(BF$_4$)$_4$] (3^{MeCN}).

WLA monomer complex **2** (201.0 mg, 0.217 mmol) and $Cu(BF_4)_2$•$6H_2O$ (74.0 mg, 0.214 mmol) were combined in 4 mL of MeCN in a 10-mL scintillation vial, and a dark- green homogenous solution formed. This solution was left to stand at 25 °C for 3 days in the glovebox, during which blue-green, block crystals, suitable for X-ray crystallographic characterization, grew upon the walls of the vial. After the 3 days, the mother liquor was decanted via pipette, and the crystals were washed with MeCN (3 × 1 mL) before being stored under a minimal amount of

MeCN (approx. 250 μL) (99.5 mg, 26%). Anal. Calcd. for $C_{46}H_{48}B_4CuF_{16}N_6P_2PdS_2$: C 41.6, H 3.64, N 6.33 %. Found: C 36.7±0.187, H 3.44±0.085, N 2.96±0.116 %. The lower CHN percentages observed for **3**^{MeCN} versus the calculated are attributed to partial loss of bound MeCN solvent molecules during high vacuum drying. The crystals were dissolved in 1 g CD_3CN for NMR analysis via sonication at 25 °C. Due to the coordination of paramagnetic d^9 Cu^{II} ions, ^1H NMR resonances corresponding to the protons in the pyridine moiety have shifted outside the spectral window and could not be observed upon expanding to 100 ppm. ^1H NMR (400 MHz, CD_3CN) δ 7.66–7.36 (m, br, 20H), δ 3.23 (s, br, 8H). $^{31}P\{^1H\}$ NMR (162 MHz, CD_3CN) δ 61.76.

3.4.2.4 [Cu(Pd(P,S-pyr)$_2$)(H$_2$O)(MeCN)$_3$][(BF$_4$)$_4$]•H$_2$O•MeCN (3^{H2O}).

WLA monomer complex **2** (46.9 mg, 0.0506 mmol) and $Cu(BF_4)_2$•$6H_2O$ (39.0 mg, 0.113 mmol) were each separately dissolved in 1 mL of MeCN, before combining them to form a 2-mL dark-green solution that was left to stand in the glovebox at 25 °C overnight. Then, Et_2O was allowed to slowly diffuse into the solution. After 24 hours, yellow, plate-like crystals suitable for single crystal X-ray analysis were obtained. The resulting crystals were stored in their growth solution.

3.4.2.5 [Cu(Pd(P,S-pyr)$_2$)(DMF)$_4$][(BF$_4$)$_4$] (3^{DMF}).

Analogous to the preparation of **3**^{MeCN}, WLA complex **2** (119.0 mg, 0.129 mmol) and $Cu(BF_4)_2$•$6H_2O$ (46.9 mg, 0.136 mmol) were combined in 3 mL of DMF in a 10-mL scintillation vial, and a yellow, homogenous solution formed. After allowing this solution to stand at 25 °C for 6 days in the glovebox in which it was prepared, Et_2O was allowed to slowly diffuse into solution. After 2 weeks, green, block crystals suitable for single crystal X-ray analysis were obtained. The resulting crystals were stored in their growth solution.

3.4.3 *In Situ* Reaction of Cl^- anion with $\mathbf{3}^{MeCN}$.

To a slurry consisting of crystals of $\mathbf{3}^{MeCN}$ (39.0 mg, 0.0294 mmol) in 1 g of CD_3CN, a solution of tetra(*n*-butyl)ammonium chloride (49.2 mg, 0.177 mmol) in 1 g of CD_3CN was added at 25 °C. Immediately upon addition, the supernatant turned from colorless to yellow, and the blue-green crystals of $\mathbf{3}^{MeCN}$ expanded and changed into a white powder. The reaction mixture was allowed to stand overnight at 25 °C in the glovebox in which it was prepared, at which point all of the crystals were consumed and transformed into an off-white solid in a yellow solution. An aliquot of the crude reaction solution was transferred to an air-free NMR tube and analyzed by ^1H and $^{31}P\{^1H\}$ NMR spectroscopy. Accurate integration of the ^1H NMR resonances is not possible due to the large excess of tetra(*n*-butyl)ammonium cations in the crude reaction solution. ^1H NMR (400 MHz, CD_3CN) δ 7.81–7.36 (m), δ 3.31–3.25 (m), δ 3.18–3.05 (m), δ 2.95–2.88 (m), δ 1.63 (tt, J = 8.2, 6.1 Hz), δ 1.38 (h, J = 7.4 Hz), δ 1.00 (t, J = 7.3 Hz). $^{31}P\{^1H\}$ NMR (162 MHz, CD_3CN) δ 28.28, δ 26.94, δ 16.01. Under aerobic conditions, the crude white solid was collected via filtration, washed with excess Et_2O, and dried *in vacuo*. ^1H NMR (400 MHz, CD_2Cl_2) δ 7.74–7.57 (m, br, 28H), δ 2.83 (s, br, 8H). $^{31}P\{^1H\}$ NMR (162 MHz, CD_2Cl_2) δ 23.08, δ 16.21.

3.4.4 X-Ray Structure Determination

Single crystals of $\mathbf{3}^{MeCN}$ and $\mathbf{3}^{DMF}$ were mounted on a MiTeGen loop, respectively, with paratone oil on a XtaLAB Synergy diffractometer equipped with a micro-focus sealed X-ray tube PhotonJet (Mo) X-ray source and a Hybrid Pixel Array Detector (HyPix) detector. The temperature of the crystals was controlled with an Oxford Cryosystems low-temperature device. Data reduction was performed with the CrysAlisPro Software using a numerical ($\mathbf{3}^{MeCN}$) or spherical ($\mathbf{3}^{DMF}$) adsorption correction. The structures were solved with the ShelXT[118] structure solution program

using the Intrinsic Phasing solution method and Olex2[119] as the graphical interface. The model was refined with ShelXL[120] using least squares minimization.

Single crystals of $\mathbf{3}^{H2O}$ were mounted on a glass fiber with paratone oil on a Kappa Apex 2 diffractometer. The temperature of the crystals was controlled with an Oxford Cryosystems low-temperature device. Data reduction was performed with the Bruker SAINT software package using a numerical adsorption correction. The structure was solved with the ShelXT[118] structure solution program using Direct Methods and Olex2[119] as the graphical interface. The model was refined with ShelXL[120] using least squares minimization.

3.4.5 Diffusion Ordered Spectroscopy Investigation of 2 and $\mathbf{3}^{MeCN}$

A 9.4 mg sample of **2** and $\mathbf{3}^{MeCN}$ were dissolved in 1 g CD_3CN, respectively, for data collection. The samples of $\mathbf{3}^{MeCN}$ were sonicated until a homogenous solution was obtained. Diffusion coefficients were obtained from a peak-by-peak fit to a three-component exponential of the Stejskal-Tanner equation for each proton resonance using the Mestrelab Research MestReNova v14.2.3. software package and reported as a range for each compound.

2.5. NMR Degradation Investigation of $\mathbf{3}^{\mathrm{MeCN}}$

Inside a glovebox under an inert atmosphere, single crystals of $\mathbf{3}^{MeCN}$ (4.5 mg, 0.0034 mmol) were sealed in an air-free NMR tube under 1 g CD_3CN. ^{1}H and $^{31}P\{^{1}H\}$ NMR spectra were obtained approximately every 24 h for 14 days. Prior to data collection, the NMR solution was mixed by inverting the NMR tube 3 times before allowing the crystals to settle to the bottom. After 4 days, the $\mathbf{3}^{MeCN}$ crystals were fully dissolved.

3.4.6 Crystallographic Data Tables

Table 3.S1. Crystallographic Data for $\mathbf{3}^{MeCN}$, $\mathbf{3}^{DMF}$, and $\mathbf{3}^{H_2O}$.

	3^{MeCN}	3^{DMF}	3^{H_2O}
Empirical Formula	$C_{46}H_{48}B_4CuF_{16}N_6P_2PdS_2$	$C_{50}H_{64}B_4CuF_{16}N_6O_4P_2PdS_2$	$C_{46}H_{50}B_4CuF_{16}N_6O_2P_2PdS_2$
Formula Weight	1328.14	1456.31	1362.16
Temperature / K	100.0(2)	200(2)	100.09
Crystal System	monoclinic	monoclinic	monoclinic
Space Group	P2/n	P2/n	$P2_1/n$
a / Å	13.3938(3)	13.6114(2)	13.3903(4)
b / Å	15.4971(3)	16.1404(2)	30.8825(9)
c / Å	14.5948(4)	14.6275(3)	14.3575(4)
α / °	90	90	90
β / °	106.664(3)	103.577(2)	106.5840(15)
γ / °	90	90	90
Volume / Å^3	2902.15(12)	3123.76(9)	5690.2(3)
Z	2	2	4
ρ_{calc} / g cm^{-3}	1.520	1.548	1.590
μ / mm^{-1}	0.893	0.841	0.915
F(000)	1334.0	1478.0	2740.0
Crystal size / mm^3	0.119 × 0.096 × 0.081	0.229 × 0.14 × 0.05	0.181 × 0.067 × 0.024
Radiation	Mo Kα (λ = 0.71073)	Mo Kα (λ = 0.71073)	Mo Kα (λ = 0.71073)
2θ Range for Data Collection / °	3.924 to 67.768	3.98 to 67.746	3.24 to 56.822
Index Ranges	−17 ≤ h ≤ 20 −23 ≤ k ≤ 23 −21 ≤ l ≤ 22	−19 ≤ h ≤ 20 −22 ≤ k ≤ 24 −22 ≤ l ≤ 22	−17 ≤ h ≤ 17 −35 ≤ k ≤ 41 −19 ≤ l ≤ 19
Reflections Collected	49265	110820	76641
Independent Reflections	10356 [R_{int} = 0.0522, R_{sigma} = 0.0403]	11665 [R_{int} = 0.0395, R_{sigma} = 0.0268]	14219 [R_{int} = 0.0565, R_{sigma} = 0.1230]
Data/Restraints/Parameters	10356/98/438	11665/519/544	14219/141/741
Goodness-of-fit on F^2	1.084	1.040	1.050
Final R indexes [I>=2σ (I)]	R_1 = 0.0661, wR_2 = 0.1827	R_1 = 0.0498, wR_2 = 0.1349	R_1 = 0.0720, wR_2 = 0.1879
Final R indexes [all data]	R_1 = 0.0785, wR_2 = 0.1901	R_1 = 0.0712, wR_2 = 0.1504	R_1 = 0.1164, wR_2 = 0.2033
Largest diff. peak/hole / e Å^{-3}	1.86/−1.27	1.71/−0.79	1.33/−1.15

Table 3.S2. Selected Bond Angles (°) for **3**^{MeCN}, **3**^{DMF}, and **3**^{H_2O}.

	3^{MeCN}	3^{DMF}	3^{H_2O}
P1–Pd1–S1	86.02(3)	85.93(2)	85.39(5)
S1–Pd1–S1	92.50(5)	91.68(3)	
P1–Pd1–P1	95.48(5)	96.49(3)	
Pd1–S1–N1	105.83(5)	110.44(4)	
P2–Pd1–S2			85.51(5)
P1–Pd1–P2			95.38(6)
S1–Pd1–S2			93.82(5)
Pd1–S1–N1			110.89(7)
Pd1–S2–N4			102.86(7)

Table 3.S3. Selected Bond Angles (°) for $\mathbf{3}^{MeCN}$, $\mathbf{3}^{DMF}$, and $\mathbf{3}^{H2O}$.

	3^{MeCN}	3^{DMF}	3^{H_2O}
Cu1–N1	2.003(3)	2.049(2)	1.990(4)
Cu1–N2	2.367(5)		2.440(7)
Cu1–N3	2.025(4)		
Cu1–O1		2.246(4)	1.997(5)
Cu1–O2		1.974(3)	
Cu2–N4			1.997(4)
Cu2–N5			2.021(7)
Cu2–N6			2.399(7)

3.4.7 Powder X-Ray Diffraction Characterization

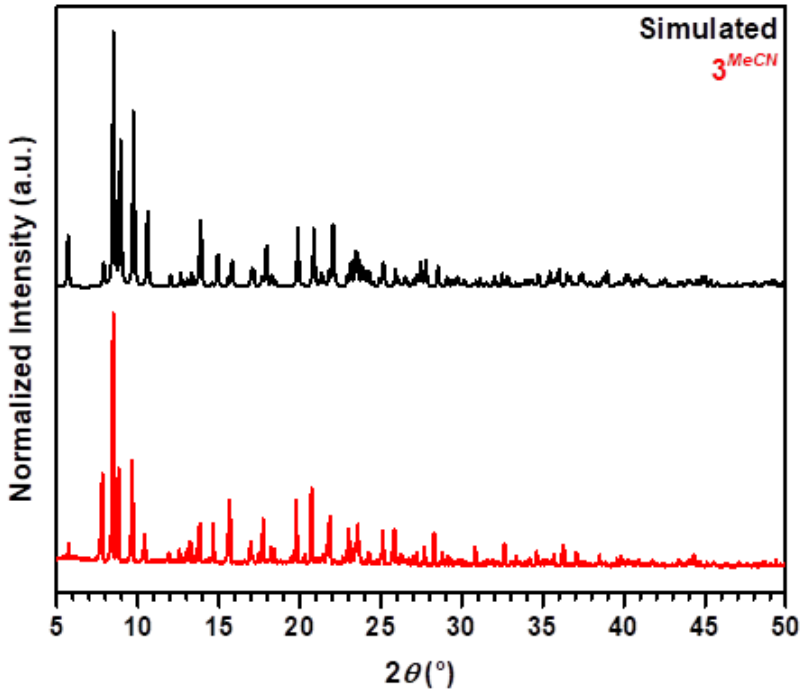

Figure 3.S1. Powder X-ray diffractogram comparing bulk crystals of **3**^{MeCN} (red, bottom) to the simulation from the single crystal X-ray structure (black, top).

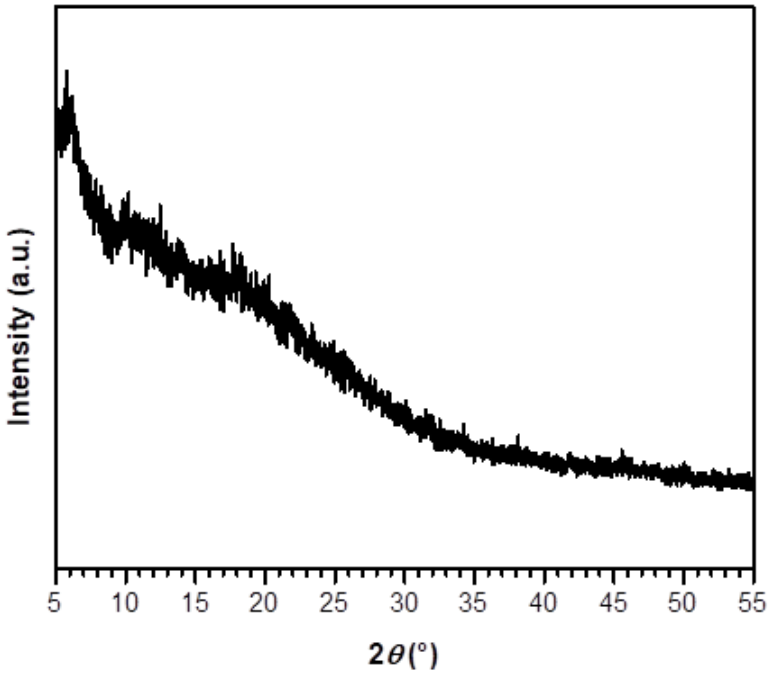

Figure 3.S2. Powder X-ray diffractogram of the white powder obtained upon exposing crystals of $\boldsymbol{3}^{MeCN}$ to Cl^- anion solutions.

3.4.8 ^{1}H DOSY NMR Characterization of 2 and 3^{MeCN}

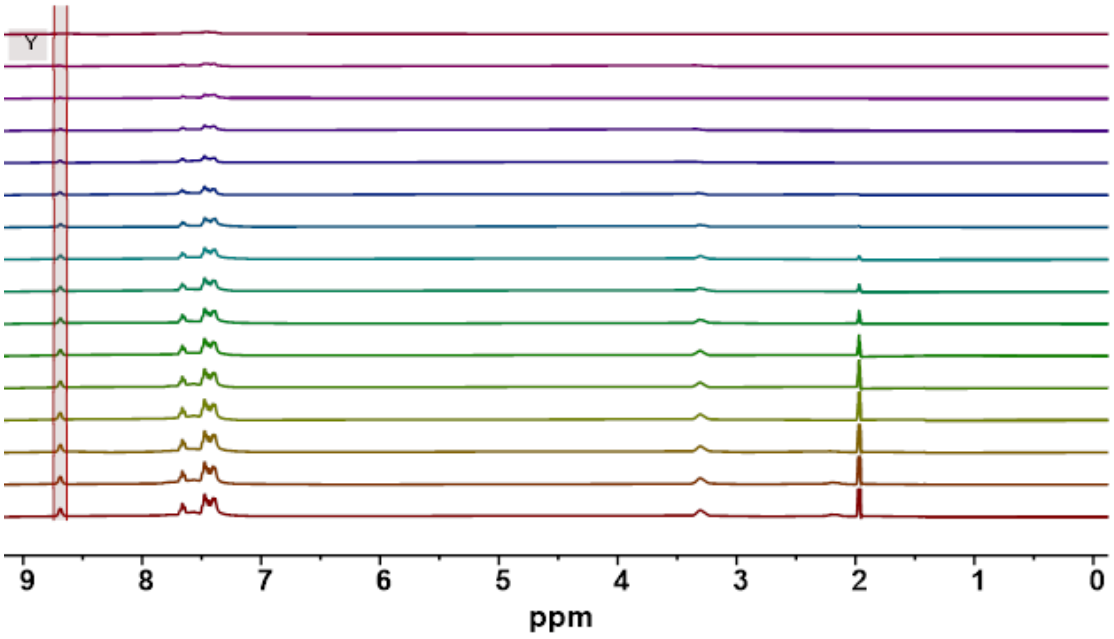

Figure 3.S3. ^{1}H NMR (400 MHz, CD_3CN, 298 K) spectra of **2** collected at decreasing gradient field strengths. The Y highlight denotes integral peak fit in **Figure 3.S4.**

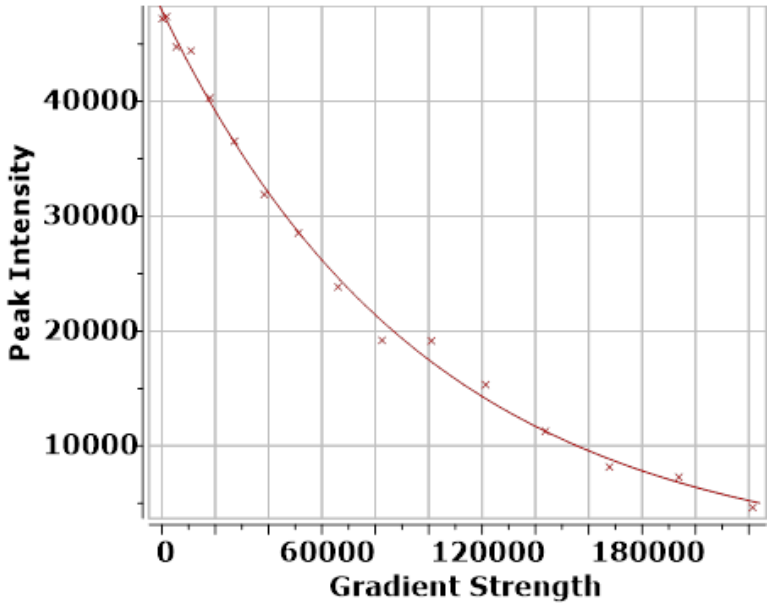

Figure 3.S4. Three-component exponential fit to the Stejskal-Tanner equation for the proton resonance highlighted in **Figure 3.S3** for **2** (D=1.01×10^{-5}).

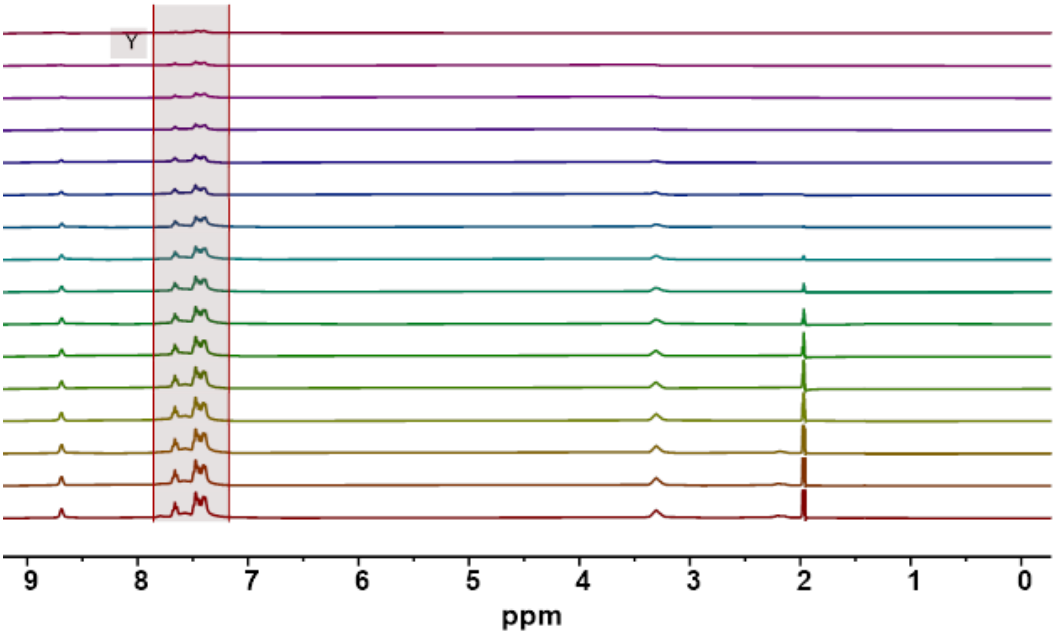

Figure 3.S5. ^{1}H NMR (400 MHz, CD_3CN, 298 K) spectra of **2** collected at decreasing gradient field strengths. The Y highlight denotes integral peak fit in **Figure 3.S6.**

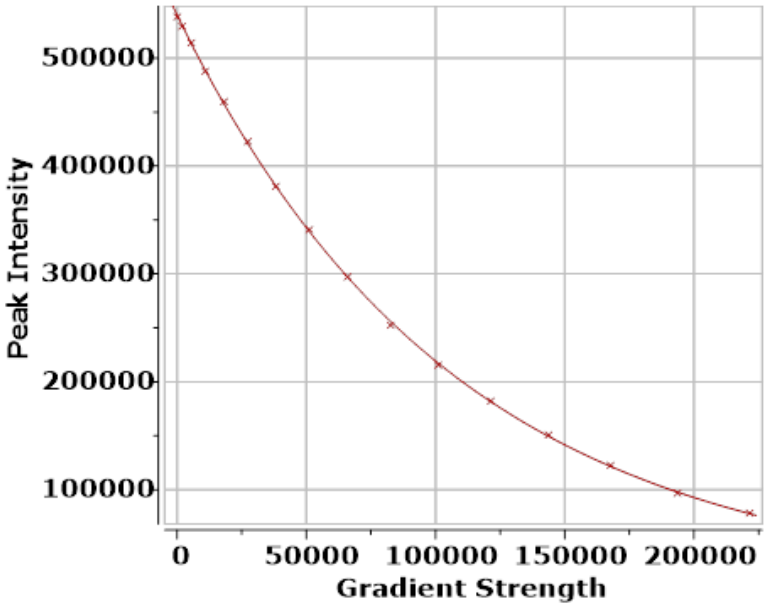

Figure 3.S6. Three-component exponential fit to the Stejskal-Tanner equation for the proton resonance highlighted in **Figure 3.S5** for **2** (D=0.930×10^{-5}).

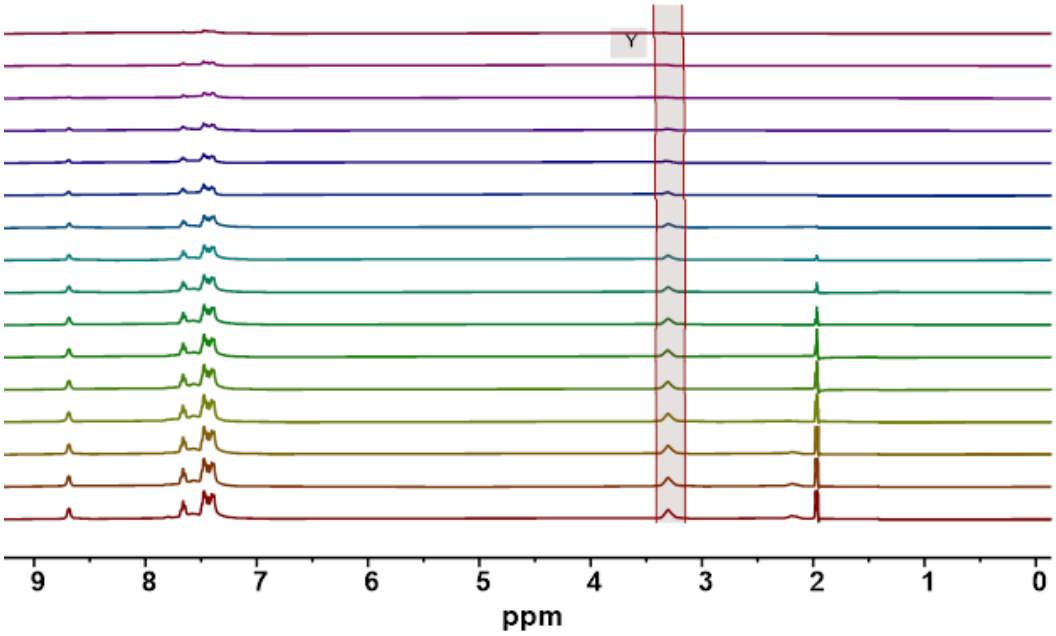

Figure 3.S7. ^{1}H NMR (400 MHz, CD_3CN, 298 K) spectra of **2** collected at decreasing gradient field strengths. The Y highlight denotes integral peak fit in **Figure 3.S8**.

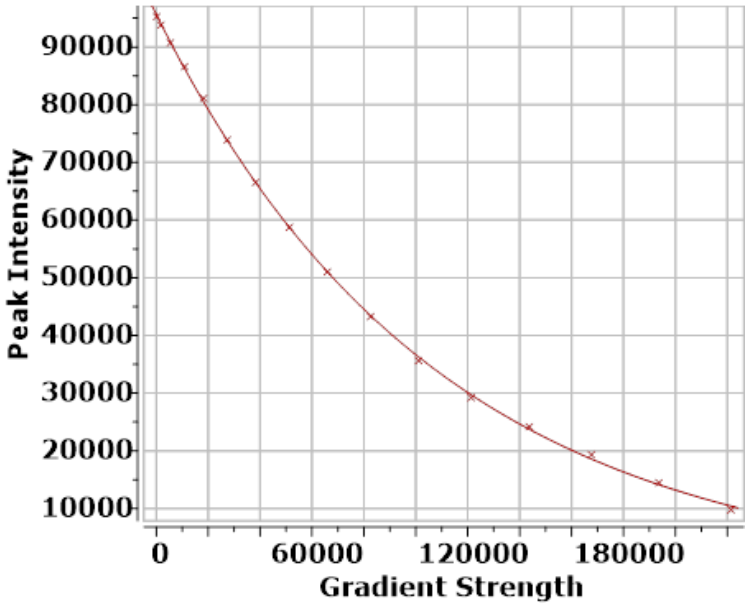

Figure 3.S8. Three-component exponential fit to the Stejskal-Tanner equation for the proton resonance highlighted in **Figure 3.S7** for **2** (D=0.922×10^{-5}).

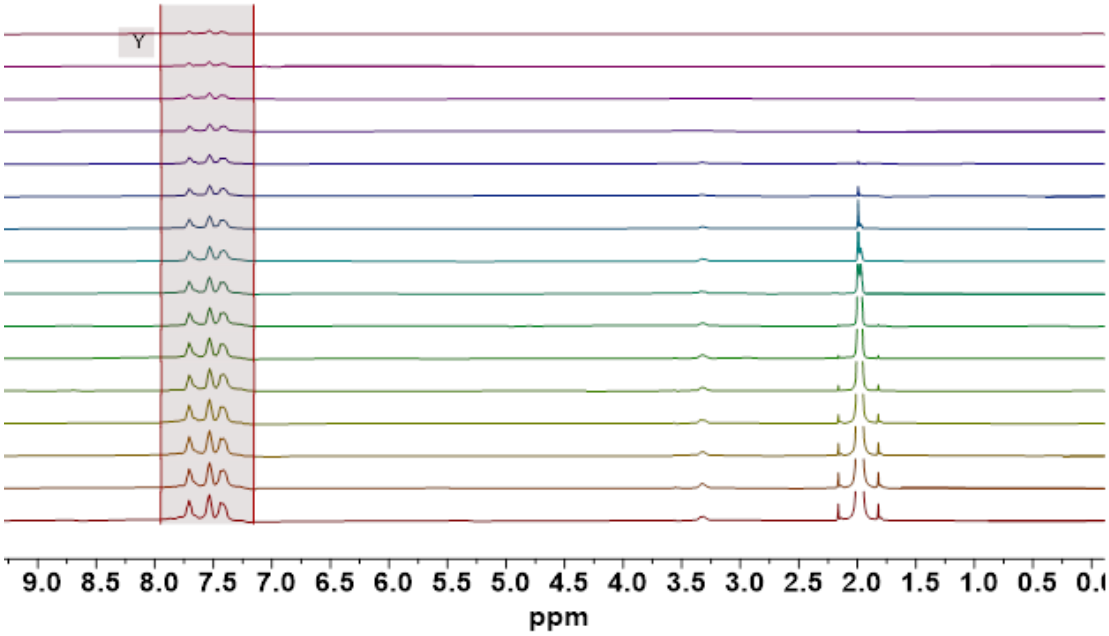

Figure 3.S9. ^{1}H NMR (400 MHz, CD_3CN, 298 K) spectra of $\mathbf{3}^{MeCN}$ collected at decreasing gradient field strengths. The Y highlight denotes integral peak fit in **Figure 3.S10.**

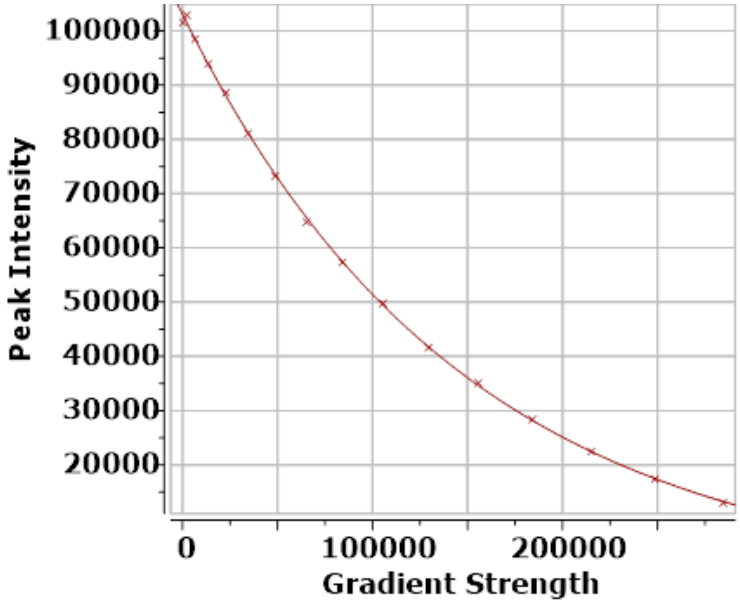

Figure 3.S10. Three-component exponential fit to the Stejskal-Tanner equation for the proton resonance highlighted in **Figure 3.S9** for $\mathbf{3}^{MeCN}$ (D=6.75×10^{-6}).

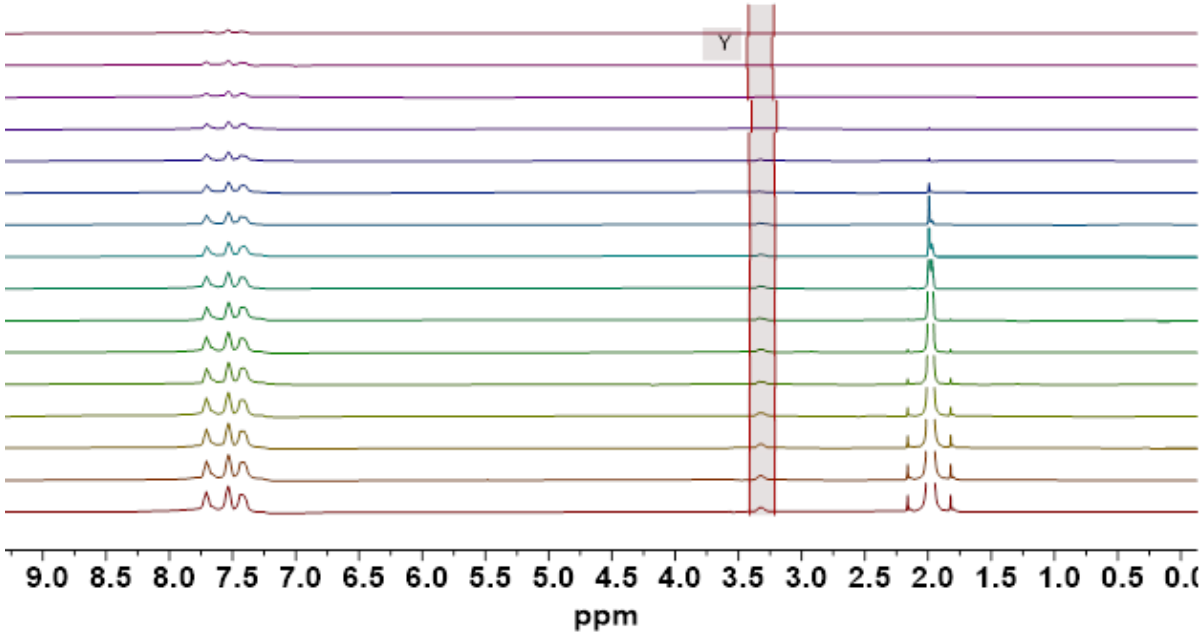

Figure 3.S11. ^{1}H NMR (400 MHz, CD_3CN, 298 K) spectra of $\mathbf{3}^{MeCN}$ collected at decreasing gradient field strengths. The Y highlight denotes integral peak fit in **Figure 3.S12.**

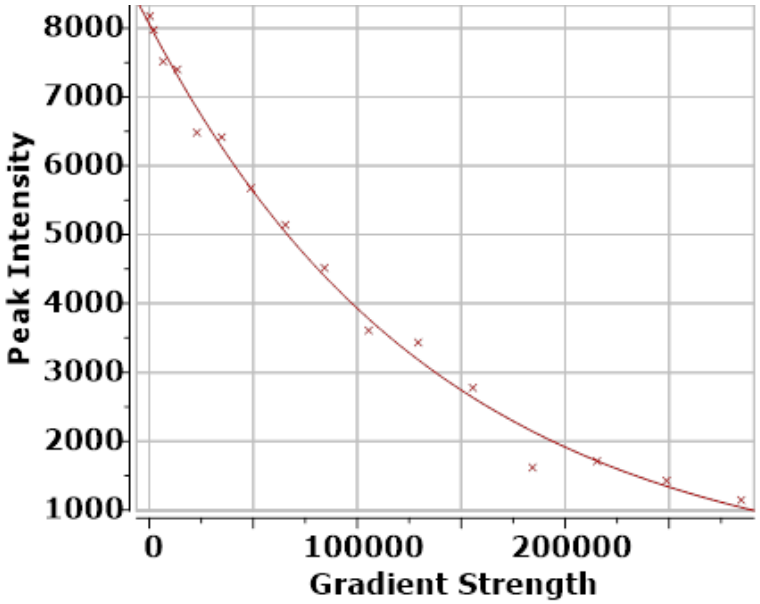

Figure 3.S12. Three-component exponential fit to the Stejskal-Tanner equation for the proton resonance highlighted in **Figure 3.S11** for $\mathbf{3}^{MeCN}$ (D=7.17×10^{-6}).

3.4.9 NMR Degradation Investigation of 3^{MeCN}

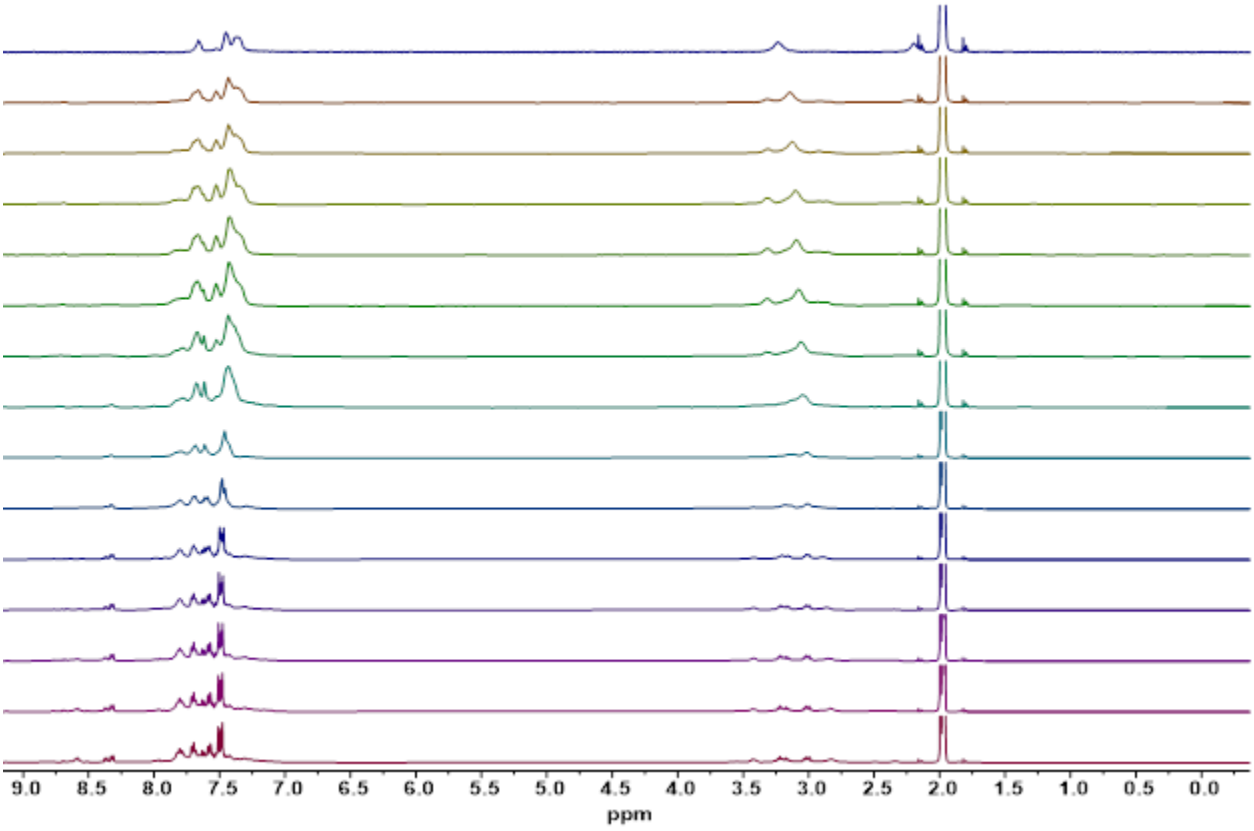

Figure 3.S13. ^{1}H NMR (400 MHz, CD_3CN, 298 K) spectra of $\mathbf{3}^{MeCN}$ showing its degradation in solution. Spectra were collected approx. every 24 h for 0 (top) to 14 (bottom) days.

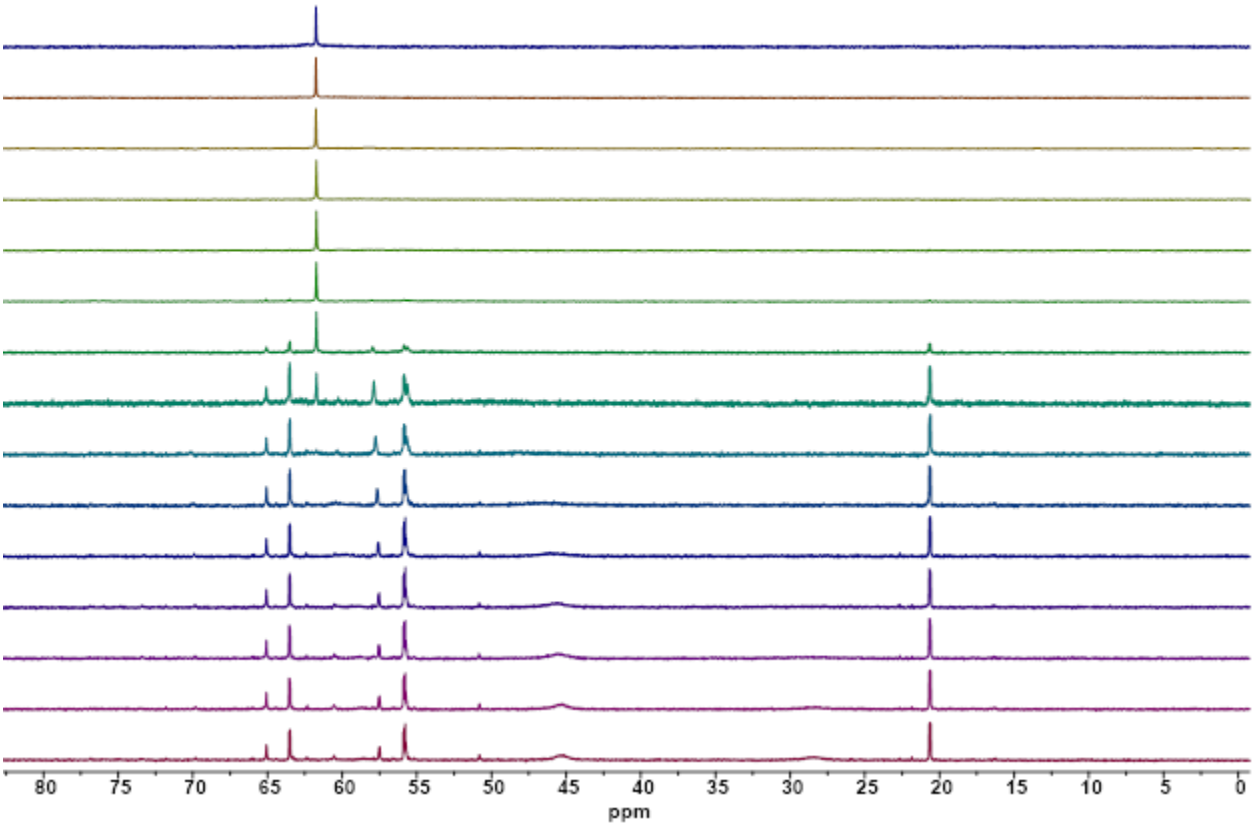

Figure 3.S14. $^{31}P\{^{1}H\}$ NMR (400 MHz, CD_3CN, 298 K) spectra of **3**^{MeCN} showing its degradation in solution. Spectra were collected approx. every 24 h for 0 (top) to 14 (bottom) days.

3.4.10 NMR Spectra

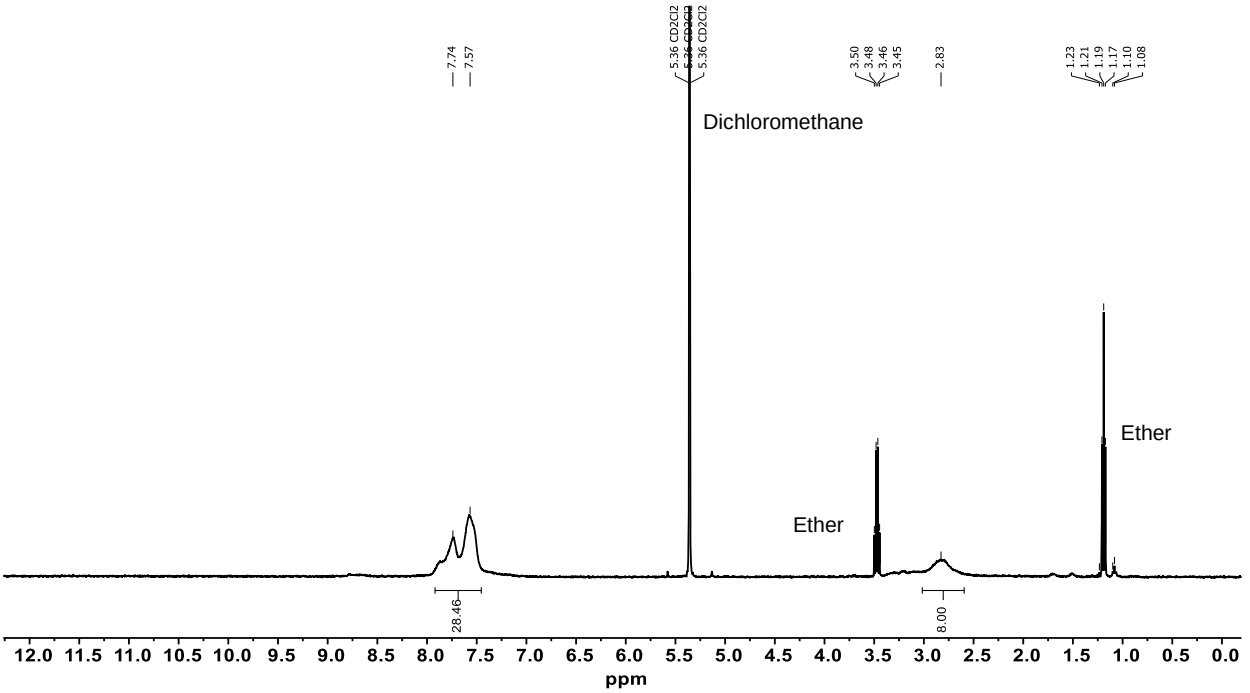

Figure 3.S15. ^{1}H NMR (400 MHz, CD_2Cl_2, 298 K) spectrum of the white powder collected following exposure of $\mathbf{3}^{MeCN}$ to excess Cl^- anions assigned to open congener $\mathbf{2}^{2Cl}$. Note the presence of Et_2O that does not affect assignments.

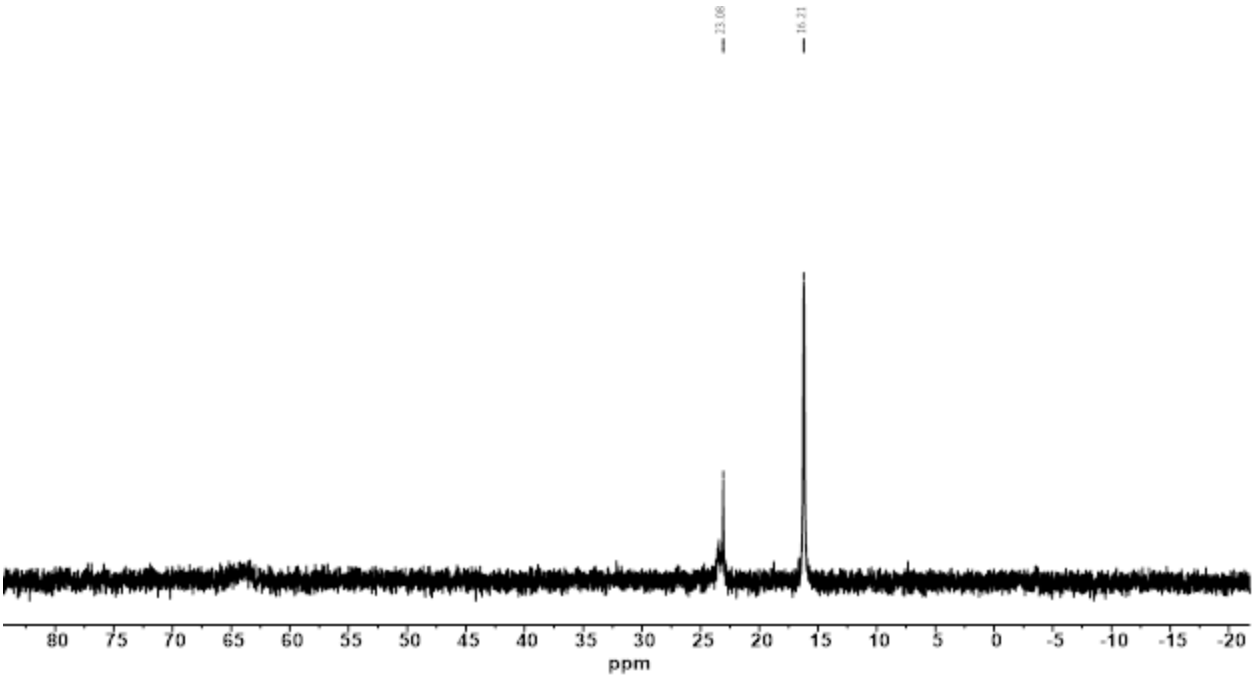

Figure 3.S16. ^{31}P{^{1}H} NMR (162 MHz, CD_3CN, 298 K) spectrum of the white powder collected following exposure of $\mathbf{3}^{MeCN}$ to excess Cl^- anions assigned to open congener $\mathbf{2}^{2Cl}$.

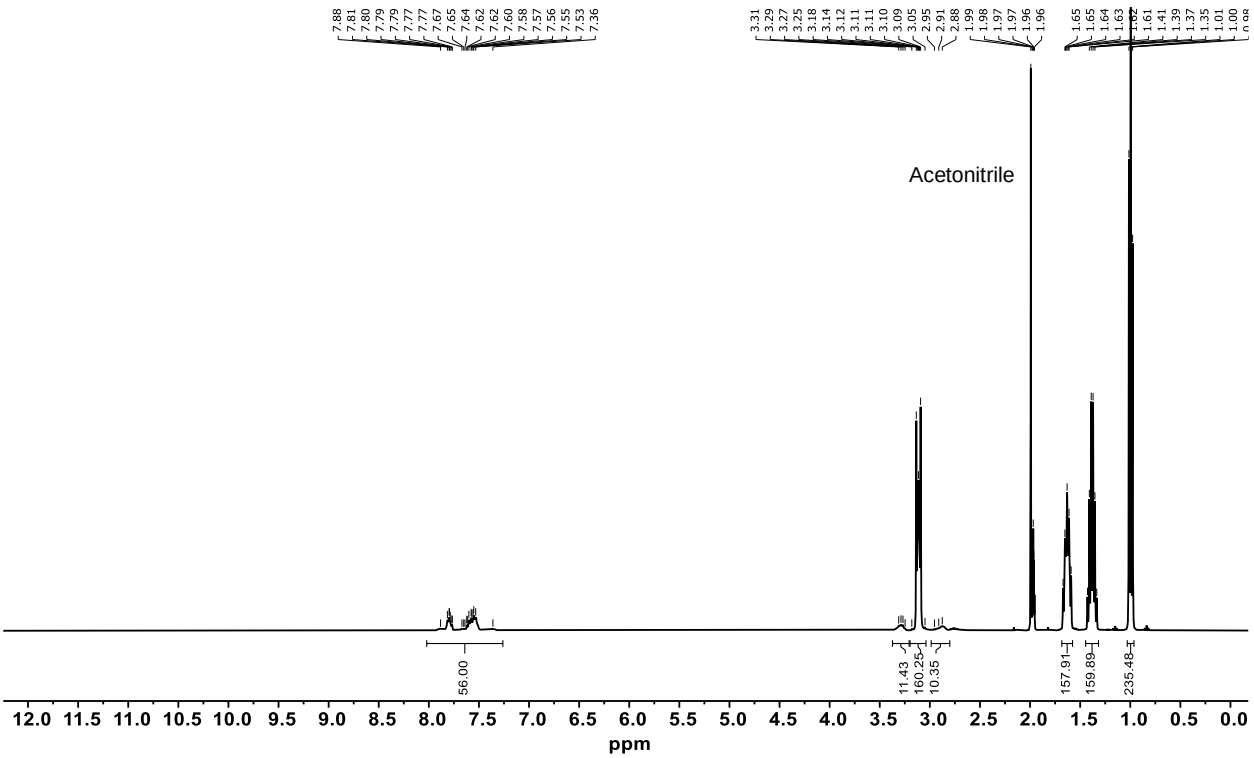

Figure 3.S17. *In situ* ^{1}H NMR (400 MHz, CD_3CN, 298 K) spectrum of the crude reaction mixture following exposure of **3**^{MeCN} to excess Cl^- anions showing a mixture of WLA complexes and tetra(*n*-butyl)ammonium cations.

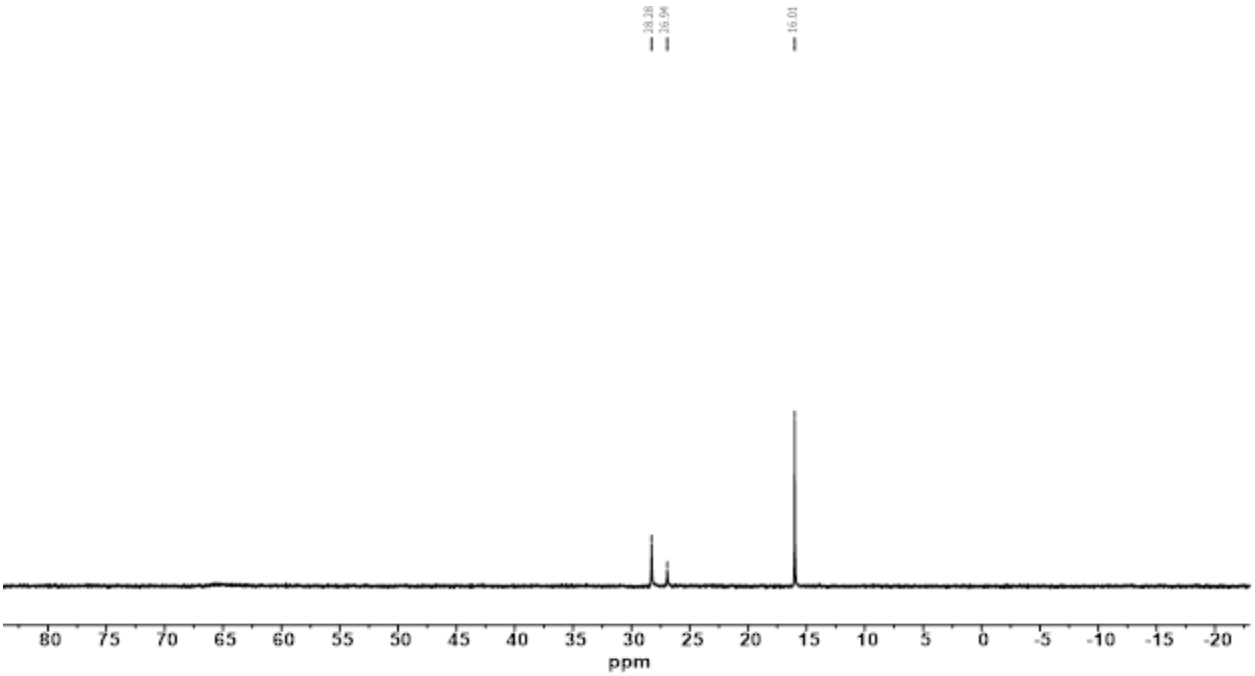

Figure 3.S18. *In situ* $^{31}P\{^{1}H\}$ NMR (162 MHz, CD_3CN, 298 K) spectra of the crude reaction mixture following exposure of **3**^{MeCN} to excess Cl^- anions.

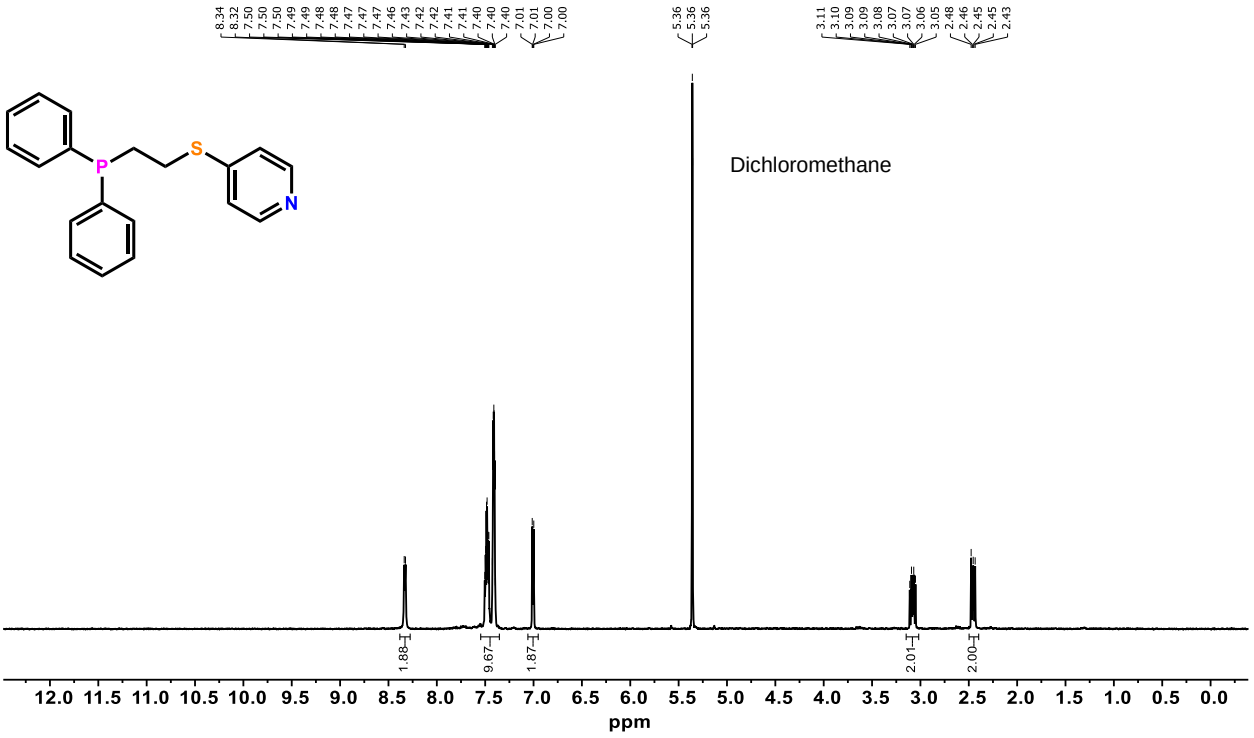

Figure 3.S19. ^{1}H NMR (400 MHz, CD_2Cl_2, 298 K) spectrum of hemilabile ligand **1**.

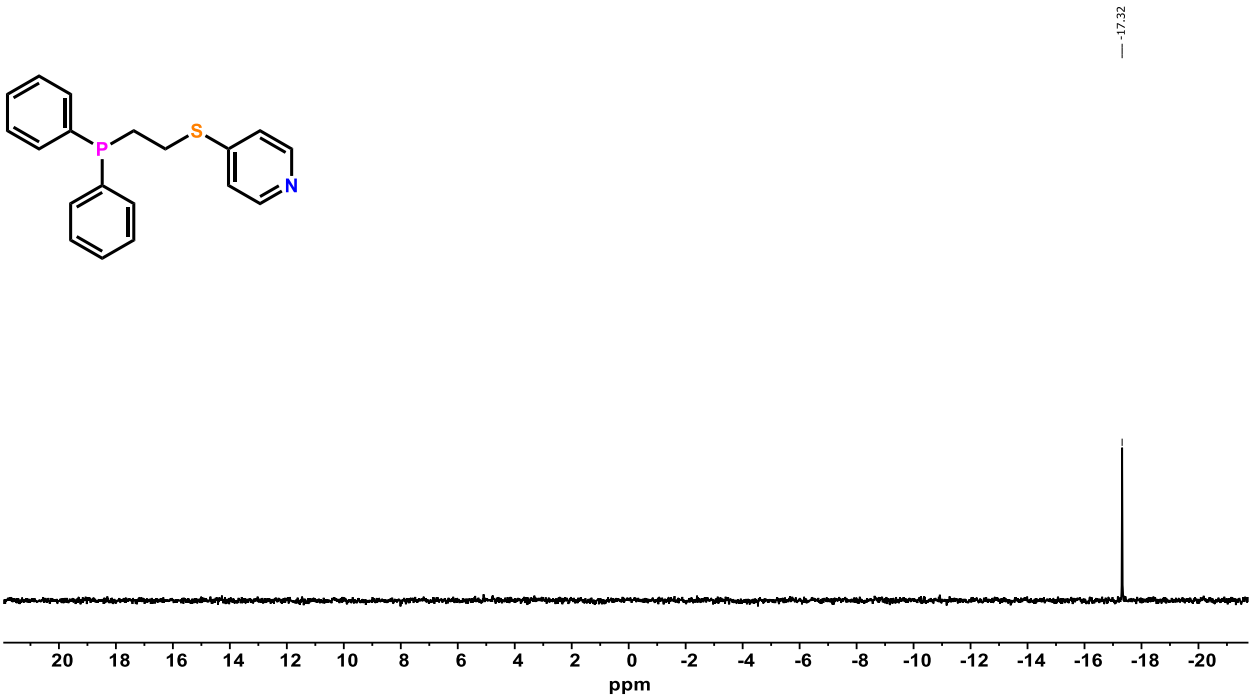

Figure 3.S20. $^{31}P\{^{1}H\}$ NMR (162 MHz, CD_2Cl_2, 298 K) spectrum of hemilabile ligand **1**

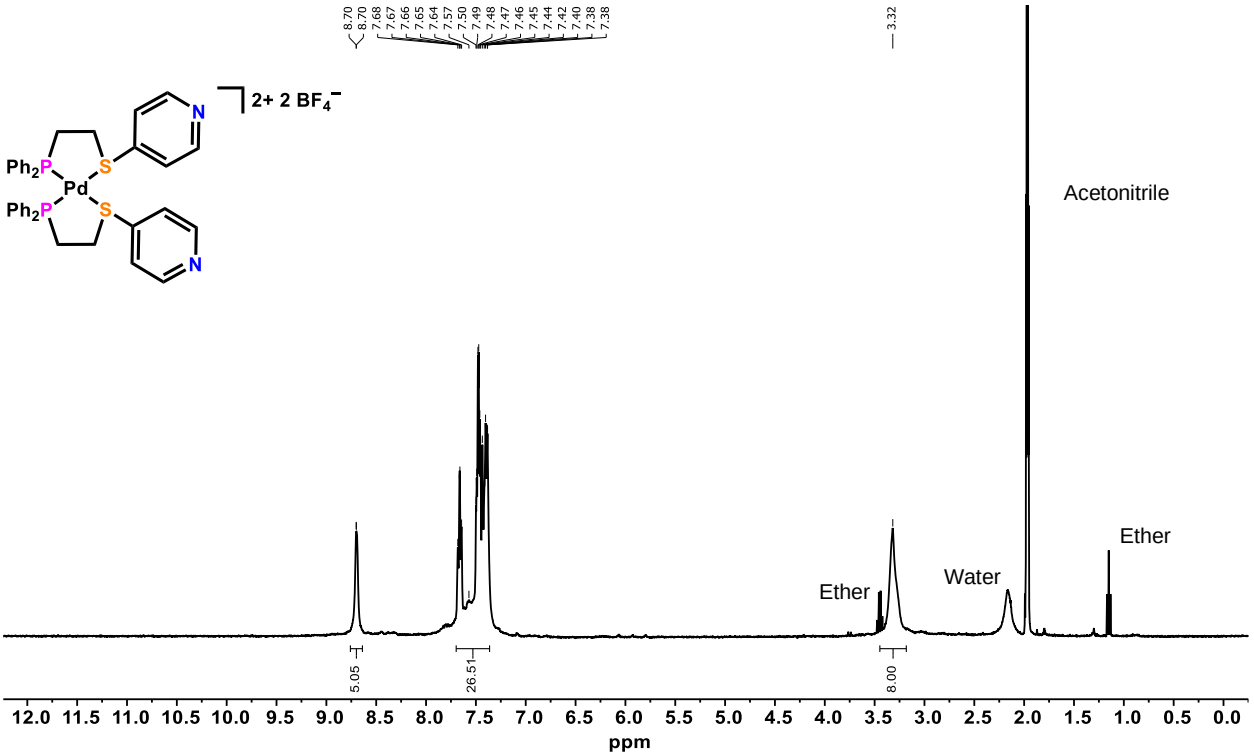

Figure 3.S21. ^{1}H NMR (400 MHz, CD_3CN, 298 K) spectrum of WLA monomer complex $[Pd(P,S\text{-}pyr)_2][(BF_4)_2]$ (**2**). Note the trace presence of water and Et_2O that does not affect assignments.

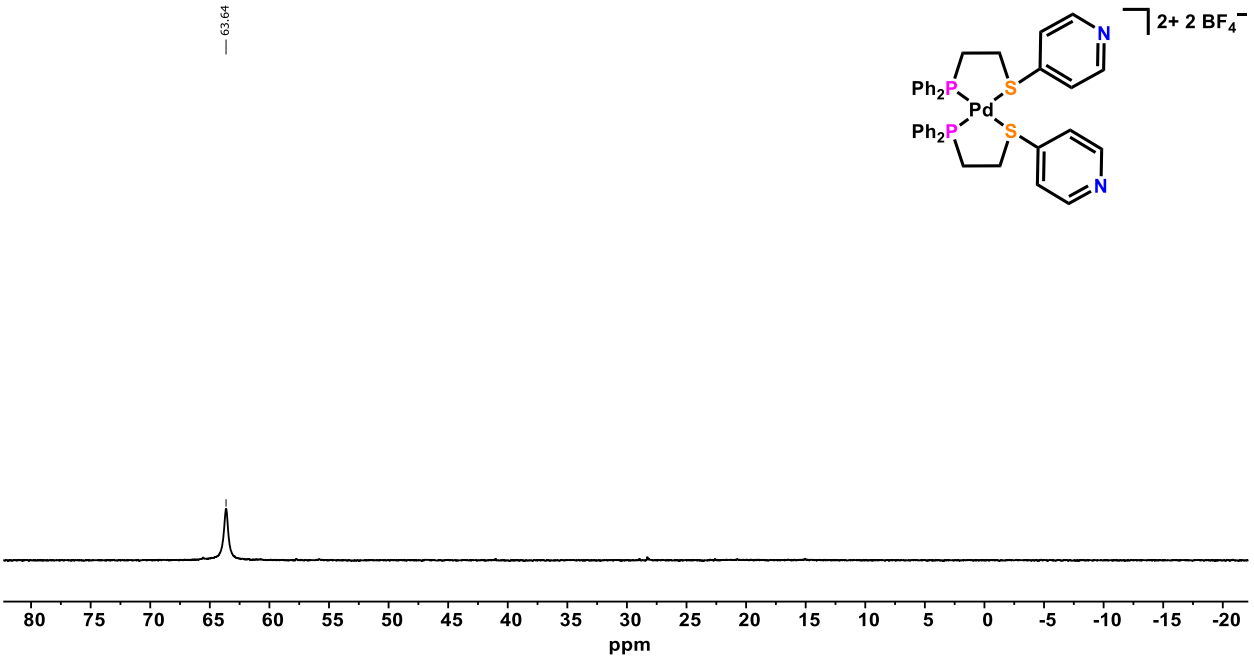

Figure 3.S22. $^{31}P\{^{1}H\}$ NMR (162 MHz, CD_3CN, 298 K) spectrum of WLA monomer complex $[Pd(P,S\text{-}pyr)_2][(BF_4)_2]$ (**2**).

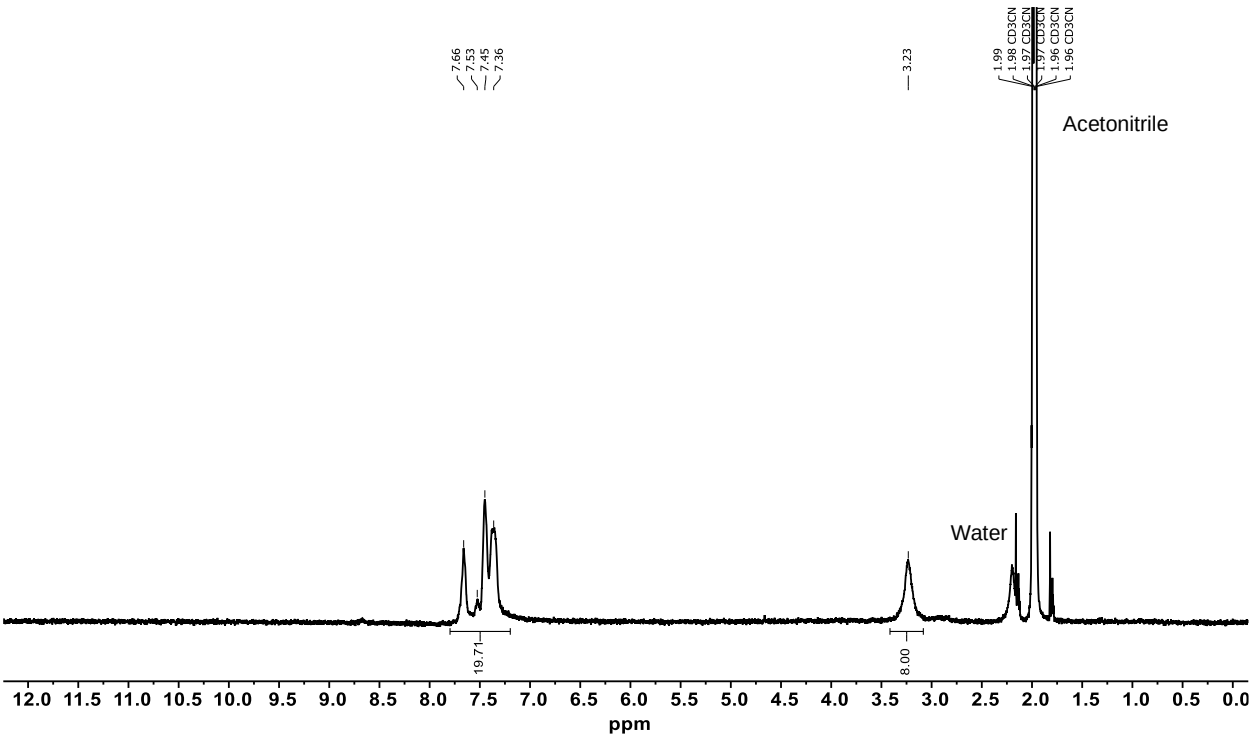

Figure 3.S23. ^{1}H NMR (400 MHz, CD_3CN, 298 K) spectrum of **3**^{MeCN} following sonication.

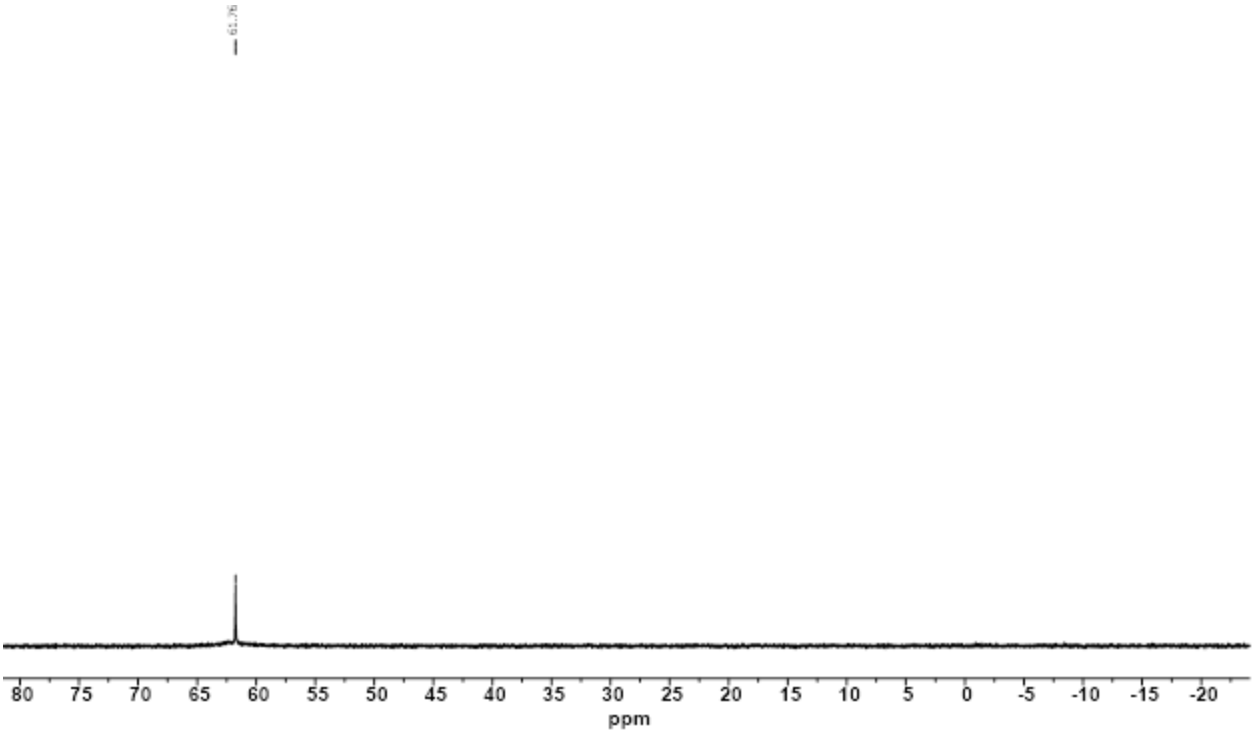

Figure 3.S24. ^{31}P{^{1}H} NMR (162 MHz, CD_3CN, 298 K) spectrum of **3**^{MeCN} following sonication.

3.4.11 MS Spectra

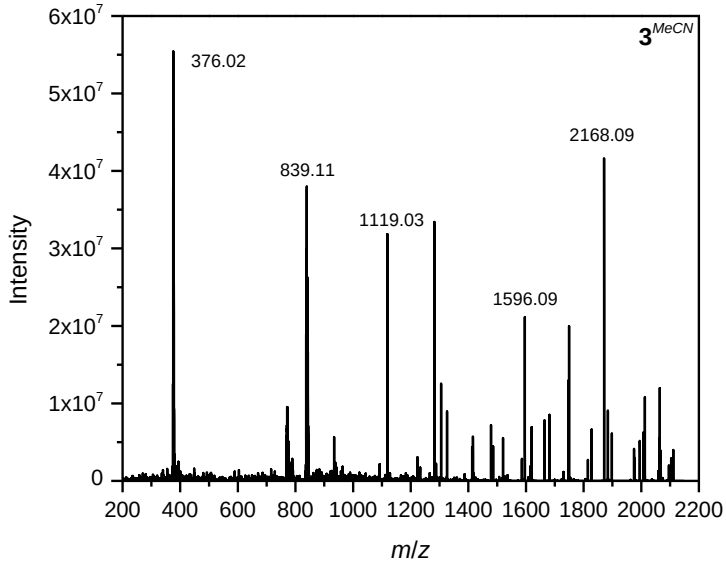

Figure 3.S25. ESI-MS (ESI+) spectrum of 3^{MeCN}.

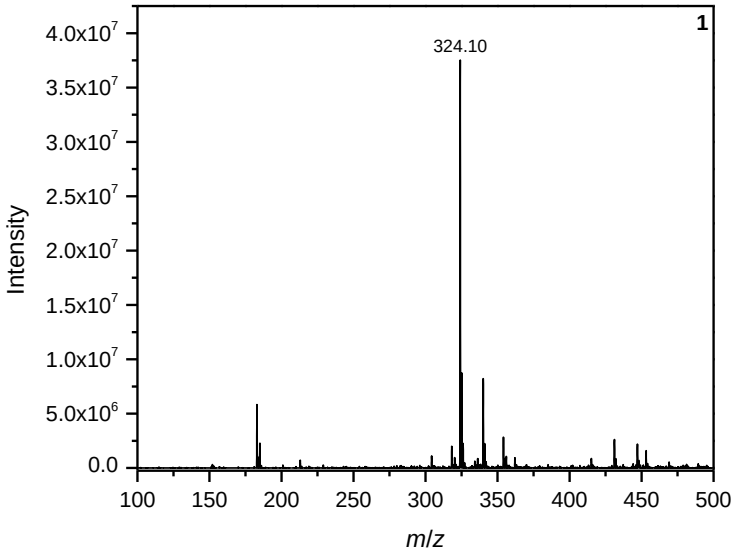

Figure 3.S26. ESI-MS (ESI+) spectrum of 1.

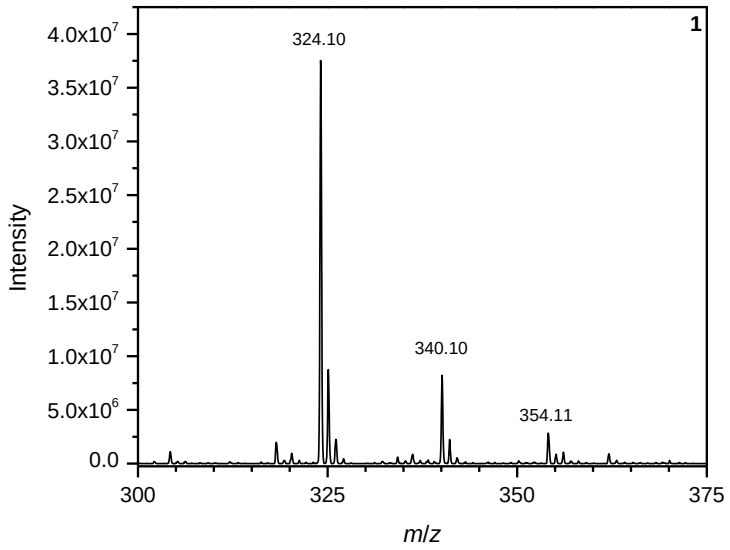

Figure 3.S27. ESI-MS (ESI+) spectrum of **1** showing the isotopic distribution of the signal at 324.10 *m*/*z*.

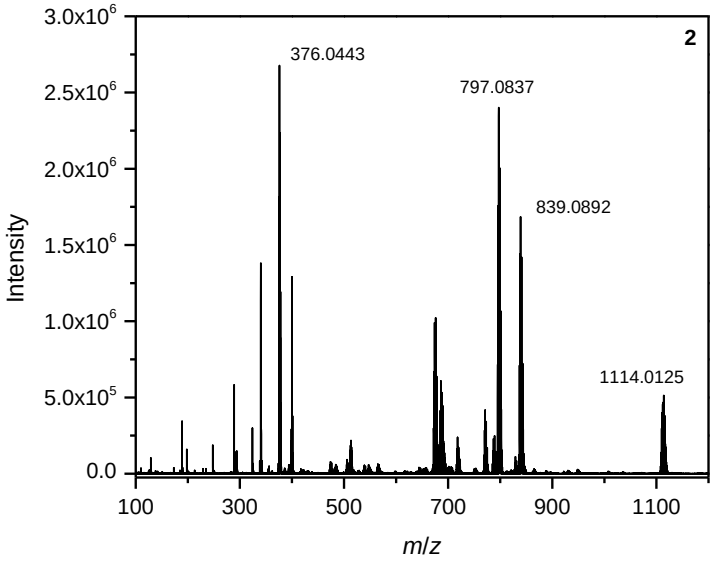

Figure 3.S28. HR-MS (ESI+) spectrum of 2.

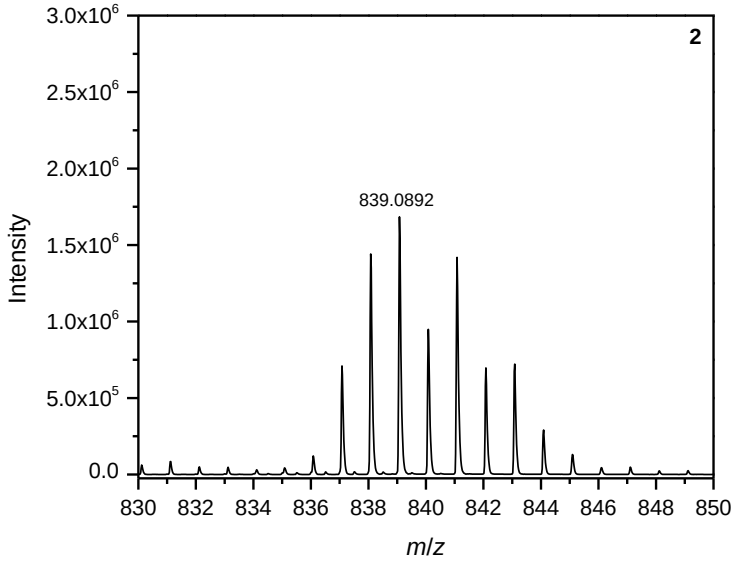

Figure 3.S29. HR-MS (ESI+) spectrum of **2** showing the isotopic distribution of the signal at 839.0892 *m*/*z*.

Chapter 4

Efforts towards Reversible Water-Soluble Weak-Link Approach Tweezers

The work presented in this chapter is based upon work that is currently underway.

The numbers, symbols, and other notations used to present chemical structures are self-contained in this chapter.

4.1 Introduction

Nature's ability to control complex chemical reactions and processes through structural transformations has long been a source of inspiration to supramolecular chemists as they build more complex functional materials. Of the multiple supramolecular platforms that have been developed for the synthesis of biomimetic constructs, the WLA stands out due to its ability to impart dynamic and flexible structural regulation to architectures synthesized via its design principles.[58, 169] Indeed, recent reports, including one presented in this work (see Chapter 3), have shown that the stimuli-responsive and dynamic features of WLA molecular tweezers and supramolecular macrocycles can be imparted even to infinite materials, such as coordination polymers, when incorporating WLA subunits within the extended structures.[90, 170] One can imagine that a similar dynamic structural regulation of biomacromolecules and polymers (e.g. nucleic acids and proteins) could be achieved by grafting WLA subunits to their structures. However, careful review of WLA literature shows that most investigations of WLA architectures are conducted in organic solvents such as dichloromethane (DCM), methanol (CH_3OH), and acetonitrile (CH_3CN), limiting an understanding of how WLA complexes perform within an aqueous environment. In order to expand the type of WLA materials that can be constructed to include WLA-biopolymer conjugates, the development of the WLA in aqueous media is paramount.

Only two previous reports have focused on the performance of WLA constructs in water and were limited to irreversible opening of the metal node, commonly achieved via the introduction of CN^- anions to solution.[171, 172] Retaining the stimuli-responsive properties of the WLA in aqueous media has remained a significant challenge, limiting the dynamic systems typified in the WLA to organic systems. To further understand that capabilities of the WLA to synthesize dynamic, effector-mediated architecturs in water, two new WLA complexes featuring

anionic sulfonate functional groups that serve to provide water-solubility to the tweezer complexes have been synthesized. We hypothesized that synthesizing hemilabile ligands with the more weakly-donating ether moiety instead of the typical thioether moiety would enable reversible structural transformation of the metal node upon exposure to Cl^- anions. Reaction of a phosphino-thioether(P,S)- or a phosphino-ether(P,O)-based hemilabile ligand with a Pt^{II} precursor results in the formation of two novel, water-soluble WLA complexes. While the Pt^{II}-(P,S) complex performed similarly to the previously reported complexes, attempts to understand the coordination structure of the metal node in (P,O)-based system was complicated by the unique features of its $^{31}P\{^1H\}$ NMR spectrum. Nevertheless, the efforts contained herein represent the first steps towards design criterion for reversible transformations of WLA complexes in water.

4.2 Results and Discussion

4.2.1 Synthesis and reactivity of 2 and 4-Closed/4-Open

The previous investigations into water-soluble WLA complexes focused on systems in which a phosphino-thioether hemilabile ligand served to form the chelate upon coordination to the metal center. Therefore, we hypothesized that the donor strength of the hemilabile ligand chelate must be weakened in comparison to the previously reported compounds in order to permit reversible structural regulation with classical WLA small-molecule and anionic effectors (e.g. Cl^- anions). Previous work has shown that the strength of the hemilabile ligand chelate can be effectively tuned via the identity of the "weak-link" binding moiety (i.e. thioether vs. ether) and judicious choice of the pendent substituents (e.g. alkyl, aryl, and perfluoroaryl). With this in mind, we hypothesized that the use of the more weakly-donating ether moiety as the "weak-link" would permit reversible, effector-mediated opening and closing of WLA complexes in aqueous media. To test this hypothesis, a (P,S)- (**1**) and a (P,O)-based (**3**) hemilabile ligand and their corresponding

homoligated Pt^{II} metal complexes were synthesized (**Scheme 4.1**). Pt^{II} was chosen as the transition metal node as the $^{31}P\{^{1}H\}$ NMR chemical shift and the observed platinum–phosphorous coupling constant, $J_{Pt–P}$, has been shown to be highly diagnostic of the metal coordination environment.[173-175]

Reaction of hemilabile ligand **1** with dichloro(1,5-cyclooctadiene)platinum(II) ($PdCl_2cod$) in DCM yields WLA complex **2**. As observed in a related sulfonate-based structure,[172] **2** is synthesized as the fully-closed homologue, confirmed via its SCXRD structure (*vide infra*). Surprisingly, the $^{31}P\{^{1}H\}$ NMR spectrum of **2** has several distinguishing characteristics in comparison to previously reported closed, Pt^{II}-based WLA complexes, namely the observed chemical shift and the $J_{Pt–P}$ coupling constant (**Figure 4.1a**). The $^{31}P\{^{1}H\}$ chemical shift of **2** appears at −8.82 ppm, much farther up field from ~5–15 ppm range observed for closed WLA complexes with Pt^{II}.[149, 172, 176] Of note, **2** features a propyl chain linking the phosphine "strong-link" to the thioether "weak-link", forming a six-membered ring when fully-closed, whereas the majority of previously reported phosphine-based WLA structures featured two carbons bridging the "strong" and "weak" links. Indeed, careful inspection of literature phosphine-based chelates that form six-membered rings upon coordination with Pt^{II} and Pd^{II} show a wide range of chemical shifts observed in their $^{31}P\{^{1}H\}$ NMR spectra, complicating structural assignment based on the chemical shift alone.[177-179] This is further compounded when observing the platinum-phosphorous coupling. Typical WLA complexes feature coupling constants in the range $J_{Pt–P}$ = 3000–3600 Hz, with the fully closed homologues displaying the smaller constants; **2** displays a coupling constant of $J_{Pt–P}$ = 3565.3 Hz. Currently, the origin of the higher constant is unclear. With the fully-closed structure in hand, we sought to understand its response to Cl^- anions in aqueous solutions. As with previous examples of (P,S)-based, water-soluble WLA complexes, there was no observable

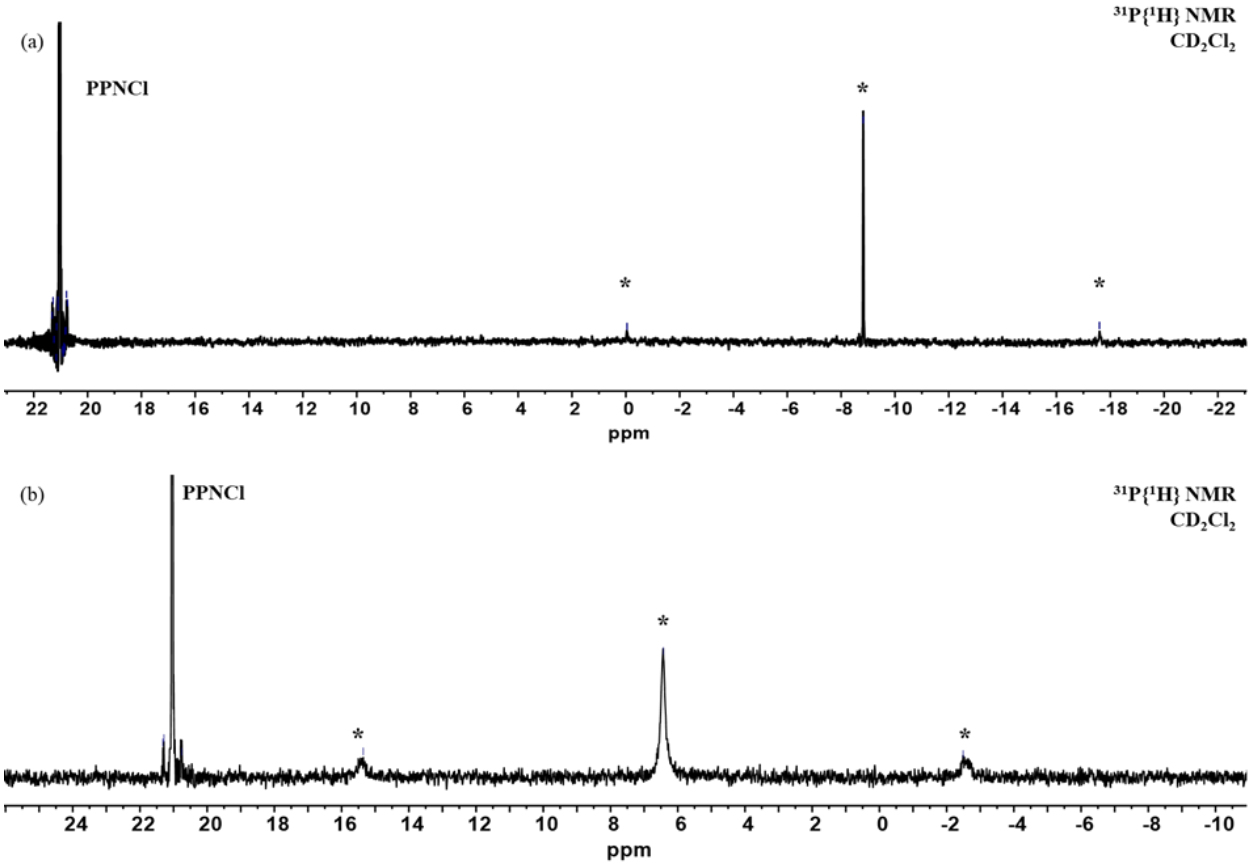

Figure 4.1. $^{31}P\{^1H\}$ NMR spectra of the (a) **2** and (b) the metal complex formed from the reaction of hemilabile ligand **3** with Pt^{II}. Asterisks denoted assigned metal complex signals. The signal arising from outer-sphere PPN counterions within solution are labeled. All spectra were obtained in CD_2Cl_2.

reaction with Cl^- anions, even with the presence of an extreme excess of the halide in solution and from various sources (e.g. NaCl and HCl).

WLA complex **4-Closed/4-Open** is synthesized in analogous method to the synthesis of **2** (**Scheme 4.1**). Reaction of hemilabile ligand **3** with $PdCl_2$cod yields **4-Closed/4-Open**. The $^{31}P\{^1H\}$ NMR spectrum of **4-Closed/4-Open** resembles that of a fully-open WLA construct in solution upon initial inspection. Its $^{31}P\{^1H\}$ chemical shift appears at 6.43 ppm ($J_{Pt–P}$ = 3605.7). However, due to the unusual characteristics of $^{31}P\{^1H\}$ NMR spectra of six-membered phosphine-based chelates, definitive assignment of the structural state of the WLA coordination node through simple inspection of the NMR spectra remains challenging,[177-179] and attempts to grow single

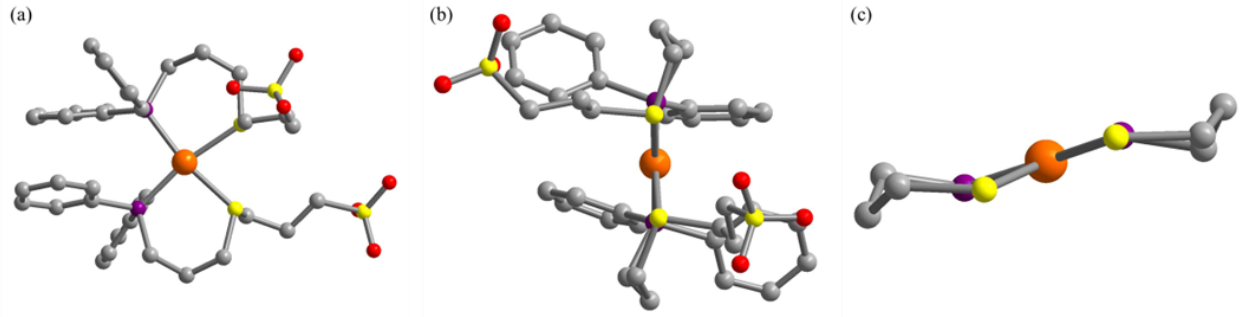

Figure 4.2. X-ray crystal structure of **2** highlighting the fully closed Pt^{II} coordination node from (a) the front, (b) side, and (c) a simplification to show the distorted boat confirmation of the bridging propyl carbon chain formed upon coordination to the Pt^{II} metal center. Orange, purple, yellow, red, and grey spheres represent Pt, P, S, O, and C atoms, respectively. H atoms have been omitted for clarity.

crystals suitable for structure determination with SCXRD were unsuccessful. Under the assumption the **4-**Open is the predominant species in solution, we attempted to close the complex with the halide abstraction agent $AgBF_4$, and this led to a complex mixture of products. As such, we have not assigned the exact structural state of **4** and note that it can be either in its fully-open or fully-closed state. Given the uncertainty in the coordination state and spectral features for **2** and **4-Closed/4-Open**, conclusions drawn from their investigation as model complexes towards reversible, water-soluble WLA complexes would be inherently ambiguous. As such, future investigations should be focused toward water-soluble (P,S) and (P,O) ligands that feature the traditional five membered chelate upon coordination to Pt^{II} (i.e. two carbon bridging the phosphine and "weak link" moieties).

4.2.2 Solid State Structure of 2

SCXRD revealed that **2** crystallizes in the monoclinic centrosymmetric space group $P2_1/c$. WLA complex **2** is in its fully closed form with both the phosphine and thioether moieties from both hemilabile ligands coordinated to the Pt^{II} core, forming a strained square planer geometry (**Figure 4.2, Table S4.1**). The P1–Pt1–S1, P2–Pt1–S2, P1–Pt1–P2, and S1–Pt1–S2 bond angles are 92.63(3), 93.55(3), 97.43(3) and 76.45(3)°, respectively. The six membered rings formed upon

chelation to the metal centers are in a distorted boat conformation to accommodate the nearly flat coordination plane around Pt^{II}. The negatively charged sulfonate extended to either side of the coordination plane, presumably to minimize electrostatic repulsions between the two groups.

4.3 Conclusions

We have reported two novel water-soluble WLA complexes featuring pendant sulfonate functional groups and three carbon bridging units between the phosphine and thioether binding moieties of the hemilabile ligands. The complexes were investigated through SCXRD and NMR spectroscopy. Notably, the three carbon bridging unit leads to unique characteristics in the NMR spectra in comparison to previously reported WLA complexes featuring two carbon units between the ”strong-” and “weak-binding” functional groups. As such, it was determined that this system was not suitable for investigation of the design criteria necessary to afford reversible, effector-mediated structural regulation of the WLA coordination node in aqueous media. Future work should be dedicated to the design of thioether and ether water-soluble, hemilabile ligands featuring two carbon bridging units.

4.4 Experimental Methods and Supplementary Materials

4.4.1 General Methods

All reactions and procedures were performed under a dinitrogen atmosphere in a Vacuum Atmospheres Nexus II glovebox or using standard Schlenk techniques unless otherwise noted. All commercially available chemicals and reagents were purchased and used without further purification unless otherwise noted. 3-Chloro-1-propanol was purchased from Oakwood Chemical. 1,3-Propanesultone and sodium 3-mercapto-1-propanesulfonate were purchased from TCI America. Anhydrous *N*,*N*-dimethylformamide (DMF), anhydrous acetonitrile (MeCN), and

0.5 M potassium diphenylphosphide solution in tetrahydrofuran (THF) was purchased from Millipore-Sigma. 1,3-Dichloropropane was purchased from Millipore-Sigma; it was dried over 4 Å mol sieves and deoxygenated under a stream of dinitrogen prior to use. Potassium *tert*-butoxide was purchased from Thermo-Fisher Scientific. Dichloro(1,5-cyclooctadiene)platinum(II) and bis(triphenylphosphine)iminium chloride were purchased from Strem Chemical. Dichloromethane (DCM) and THF were dried using a commercial solvent purification system purchased from JC Meyer Solvent Systems and deoxygenated under a stream of argon prior to use. Filtrations were performed by gravity through a Whatman medium to fine mesh filter paper using a Büchner funnel. Flash chromatography was performed on a Teledyne Combi*Flash* Rf+ equipped with RediSep Rf Gold Silica Gel Flash columns (20–40 microns). ^{1}H and ^{31}P{^{1}H} NMR spectra were collected on a Bruker Avance III HD 500 MHz spectrometer at 298 K under ambient conditions. Chemical shifts (δ) are given in parts per million (ppm). ^{1}H NMR spectra were referenced to residual solvent proton resonances (CD_2Cl_2 = δ 5.32; D_2O = δ 4.80), and ^{31}P{^{1}H} NMR spectra were indirectly referenced via ^{31}P gyromagnetic ratio. Deuterated solvents (CD_2Cl_2 and D_2O) were purchased from Cambridge Isotope Laboratories.

4.4.2 Syntheses

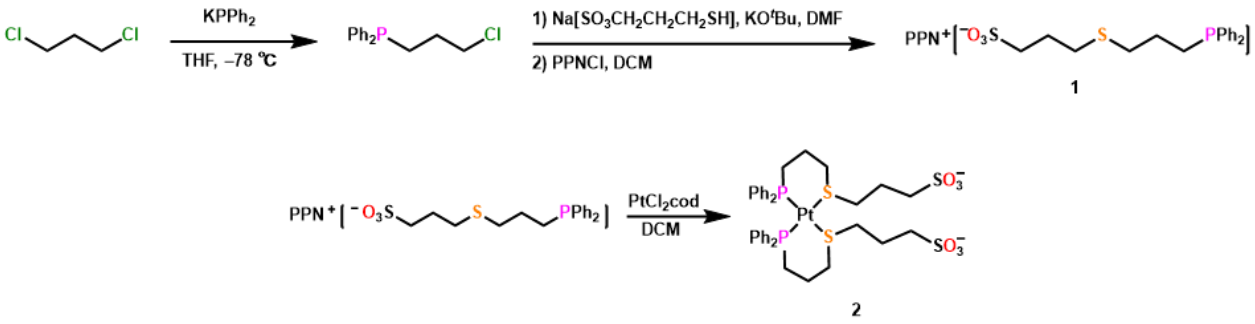

Scheme 4.S1. Full synthesis of water-soluble hemilabile ligand **1** and WLA complex **2**.

4.4.2.1 (3-Chloropropyl)diphenylphosphine

(3-Chloropropyl)diphenylphosphine was synthesized via modification of literature procedures for a previously synthesized analogous compound. [58, 88, 166-168] To a stirring solution of 1,3-dichloropropane (12 mL, 14.28 g, 126.31 mmol) in 160 mL THF, a solution of 40 mL of 0.5 M potassium diphenylphosphide (20 mmol) in THF was added dropwise at −78 °C overnight. Following addition, the reaction solution was a faint orange color. It was left to stir and warm slowly to room temperature overnight in the dark. After 18 hr, the reaction had turned milky white and opalescent. Workup was then performed under aerobic conditions. The organics were removed under reduced pressure to afford an opaque glass; the glass was dissolved in 150 mL distilled water and extracted 3 x 100 mL DCM. The organics were then combined, dried over anhydrous $MgSO_4$, and removed to afford a faint yellow oil. The oil was purified by column chromatography on silica gel using 100% DCM to afford the desired product as a waxy white solid ^{1}H NMR (400 MHz, CD_2Cl_2) δ 7.62 – 7.24 (m, 10H), 3.75 (t, *J* = 6.2 Hz, 2H), 3.66 (t, *J* = 6.5 Hz, 2H), 1.93 (ddt, *J* = 15.6, 8.2, 6.5 Hz, 2H). ^{31}P NMR (162 MHz, CD_2Cl_2) δ -17.10.

4.4.2.2 Hemilabile ligand 1

In a 20 mL scintillation vial in a glovebox, potassium tert-butoxide (157 mg, 1.40 mmol) was added in portions to a stirring slurry of sodium 3-mercapto-1-propanesulfonate (178 mg, 1.00 mmol) in 30 mL DMF. After complete addition, the reaction mixture was stirred for 20 min. Then, (3-chloropropyl)diphenylphosphine (256 mg; 0.990 mmol) was added to afford a pale-yellow mixture. The vial was sealed with a cap and electrical tape, removed from the glovebox, and heated to 90 °C overnight. Workup was then conducted under aerobic conditions. The reaction was cooled to room temperature, filtered, and the organics removed under reduced pressure to afford a pale-yellow oil. The oil was purified by column chromatography to yield the potassium salt of **1** as an off-white solid (241.9 mg; 58.1%). ^{1}H NMR (500 MHz, D_2O) δ 7.57 – 7.14 (m, 10H), 2.91 – 2.78

(m, 2H), 2.57 (dd, *J* = 8.1, 6.1 Hz, 2H), 2.47 (dd, *J* = 8.1, 6.5 Hz, 2H), 2.18 (t, *J* = 7.9 Hz, 2H), 1.95 – 1.72 (m, 2H), 1.74 – 1.49 (m, 2H). ^{31}P NMR (202 MHz, D_2O) δ -17.84. The bis(triphenylphosphine)iminium salt **1** was obtained by stirring a slurry of the potassium salt (106.6 mg; 0.254 mmol) and bis(triphenylphosphine)iminium chloride (145.5 mg; 0.2535 mmol) in 2 mL DCM overnight at room temperature under an inert atmosphere. The reaction mixture was then filtered, and the organics removed under reduced pressure to afford **1** as a white waxy solid (183.0 mg; 81.4%). ^{1}H NMR (500 MHz, $CDCl_3$) δ 7.82 – 6.99 (m, 40H), 2.92 – 2.79 (m, 2H), 2.51 (dt, *J* = 18.0, 7.4 Hz, 4H), 2.13 – 2.02 (m, 4H), 1.64 – 1.52 (m, 2H).

4.4.2.3 Water-soluble WLA Complex 2

Hemilabile ligand **1** (388.3mg; 0.922 mmol) and dichloro(1,5-cyclooctadiene)platinum(II) were stirred in 3 mL DCM overnight. Workup was then performed under aerobic conditions. The reaction was filtered and concentrated under reduced pressure; then, diethyl ether was added to precipitate **3** as an off-white solid. ^{1}H NMR (500 MHz, CD_2Cl_2) δ 7.65 – 7.03 (m, 80H), 2.86 (t, *J* = 7.0 Hz, 4H), 2.73 – 2.59 (m, 0H), 2.38 (q, *J* = 8.4 Hz, 3H), 2.13 (s, 5H), 1.89 (s, 21H). ^{31}P{^{1}H} NMR (202 MHz, CD_2Cl_2) δ 42.43, 21.04, -8.82 ($^1J_{P-Pt}$ = 3565.3 Hz) .

4.4.2.4 Potassium 3-chloroethyl 3-sulfonatopropyl ether

In a 20 mL scintillation vial inside the glovebox, potassium tert-butoxide (500.4 mg; 4.459 mmol) was added in portions to stirring neat 3-chloro-1-propanol (487.9 mg; 3.995 mmol). The reaction was stirred for 20 min before 1,3-propanesultone (487.9 mg; 3.995 mmol) was added. Upon addition, the reaction mixture began to gel. The vial was sealed with a cap and electrical tape, removed from the glovebox, and heated to 60 °C overnight. After stirring overnight, the reaction was transferred warm to a falcon tube, and the desired product was precipitated via

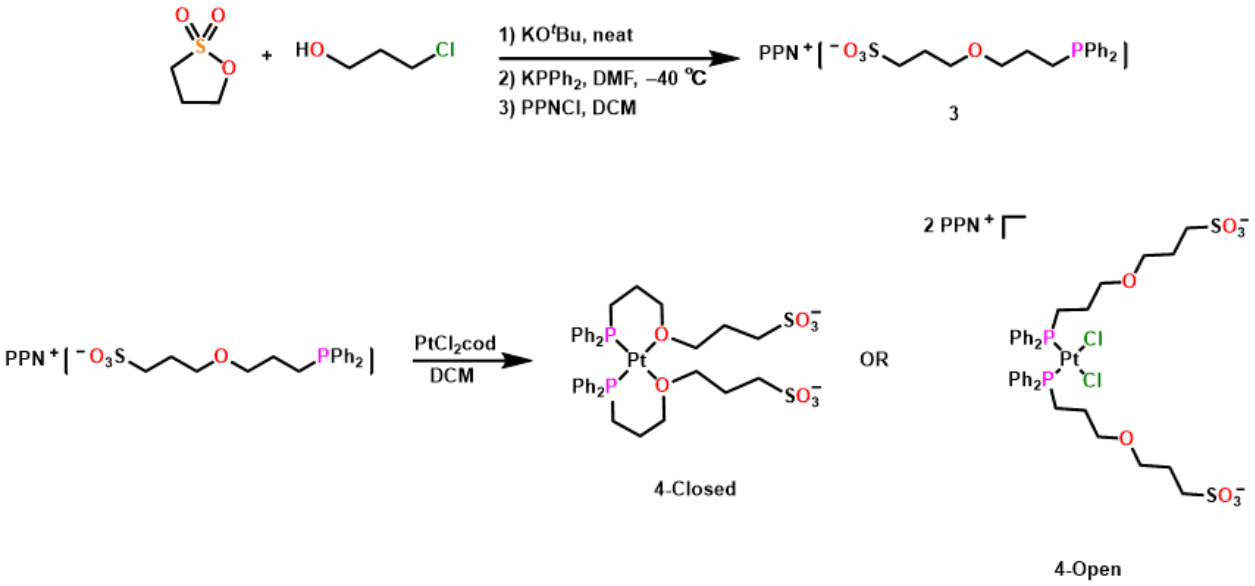

Scheme 4.S4.1. Full synthesis of water-soluble hemilabile ligand **3** and WLA complexes **4-Closed** or **4-Open**.

addition of acetone and used without further purification (909.5 mg; 89.4 %). ^{1}H NMR (500 MHz, D_2O) δ 3.67 – 3.53 (m, 6H), 2.95 – 2.85 (m, 2H), 2.03 – 1.89 (m, 4H). ^{13}C{^{1}H} NMR (126 MHz, D_2O) δ 68.75, 67.22, 67.12, 60.17, 47.94, 47.91, 43.53, 42.00, 31.48, 27.44, 24.25.

4.4.2.5 Hemilabile ligand 3

To a stirring solution of potassium 3-chloroethyl 3-sulfonatopropyl ether (475.7 mg; 1.867 mmol) in 25 mL, a potassium diphenylphosphide solution (4 mL; 0.5 M in THF) was added dropwise by syringe at −40 °C. The reaction was left to warm slowly to room temperature overnight in the dark. After stirring overnight, the reaction was red-orange. Workup was performed under aerobic conditions. The reaction was concentrated under reduced pressure and diethyl ether added to precipitate a crude brown solid. The solid was purified by column chromatography on silicia using a 5–100% DCM-Methanol gradient to afford the potassium salt of **3** as an off-white solid with a minor phosphine containing contaminant. ^{1}H NMR (500 MHz, D_2O) δ 7.30 – 7.01 (m, 10H), 3.23 (td, J = 6.5, 3.2 Hz, 4H), 2.78 – 2.68 (m, 2H), 1.92 – 1.74 (m, 4H), 1.45 (tt, J = 9.5, 4.9 Hz, 2H). ^{31}P{^{1}H} NMR (202 MHz, D_2O) δ 41.80, -17.18. The bis(triphenylphosphine)iminium

salt **3** was obtained by stirring a slurry of the potassium salt (355.4 mg; 0.8786 mmol) and bis(triphenylphosphine)iminium chloride (509.5 mg; 0.8876 mmol) in 5 mL DCM overnight at room temperature under an inert atmosphere. The reaction mixture was then filtered, and the organics removed under reduced pressure to afford **3** as a white waxy solid (727.0 mg; 91.5%). ^{1}H NMR (500 MHz, CD_2Cl_2) δ 7.63 – 7.12 (m, 37H), 3.34 (td, *J* = 6.5, 3.4 Hz, 4H), 2.68 – 2.58 (m, 2H), 2.05 – 1.94 (m, 2H), 1.87 (dq, *J* = 9.7, 6.7 Hz, 2H), 1.54 (qt, *J* = 8.4, 6.3 Hz, 2H). ^{31}P{^{1}H} NMR (202 MHz, CD_2Cl_2) δ 21.04, -15.90.

4.4.2.6 Water-soluble WLA Complex 4-Open or 4-Closed

Hemilabile ligand **3** (99.0 mg; 0.110 mmol) and dichloro(1,5-cyclooctadiene)platinum(II) (19.1 mg; 0.0510 mmol) was stirred in 2 mL DCM overnight. Workup was then performed under aerobic conditions. The reaction concentrated under reduced pressure; then, diethyl ether was added to precipitate **3** as an off-white waxy solid. ^{1}H NMR (500 MHz, CD_2Cl_2) δ 7.78 – 7.23 (m, 41H), 3.39 (s, 2H), 3.28 (s, 2H), 2.73 (s, 2H), 2.25 (s, 2H), 1.85 (d, *J* = 67.4 Hz, 9H). ^{31}P{^{1}H} NMR (202 MHz, CD_2Cl_2) δ 31.54, 21.04, 6.43 ($^{1}J_{P-Pt}$ = 3605.7 Hz).

4.4.3 X-ray Structure Determination

Single crystals of **2** suitable for structural determination were grown via slow diffusion of pentane into a DCM solution of **2.** A crystal was then selected and mounted on a MiTeGen loop with paratone oil on a XtaLAB Synergy diffractometer equipped with a micro-focus sealed X-ray tube PhotonJet (Mo) X-ray source and a Hybrid Pixel Array Detector (HyPix) detector. The temperature of the crystals was controlled with an Oxford Cryosystems low-temperature device at 100 K. Data reduction was performed with the CrysAlisPro Software using a numerical adsorption correction. The structures were solved with the ShelXT[118] structure solution program using the

Intrinsic Phasing solution method and Olex2[119] as the graphical interface. The model was refined with ShelXL[120] using least squares minimization. Due to the quality of the crystals, the solvent mask procedure in OLEX2 was implemented. This does not affect the description of molecular connectivity of the closed complex as the Pt^{II} node is charge-balanced by the imbedded sulfonate groups in hemilabile ligand **1**, leading to an overall neutral compound.

Table 4.S1. Crystallographic Data for **2.**

	2
Empirical Formula	$C_{72}H_{88}O_{12}P_4Pt_2S_8$
Formula Weight	1915.96
Temperature / K	100.0
Crystal System	monoclinic
Space Group	$P2_1/c$
a / Å	14.0317(2)
b / Å	10.45610(10)
c / Å	29.5896(5)
α / °	90
β / °	90.5870(10)
γ / °	90
Volume / Å^3	4341.07(10)
Z	2
ρ_{calc} / g cm^{-3}	1.466
μ / mm^{-1}	3.537
F(000)	1920.0
Crystal size / mm^3	0.07 × 0.03 × 0.01
Radiation	Mo Kα (λ = 0.71073)
2θ Range for Data Collection / °	4.022 to 67.78
Index Ranges	$-20 \leq h \leq 22$ $-15 \leq k \leq 16$ $-42 \leq l \leq 45$
Reflections Collected	139081
Independent Reflections	16082 [R_{int} = 0.0735, R_{sigma} = 0.0568]
Data/Restraints/Parameters	16082/0/442

Goodness-of-fit on F^2	1.039
Final R indexes [I>=2σ (I)]	R_1 = 0.0373, wR_2 = 0.0753
Final R indexes [all data]	R_1 = 0.0687, wR_2 = 0.0840
Largest diff. peak/hole / e Å^{-3}	2.70/−1.76

4.4.4 NMR Spectra

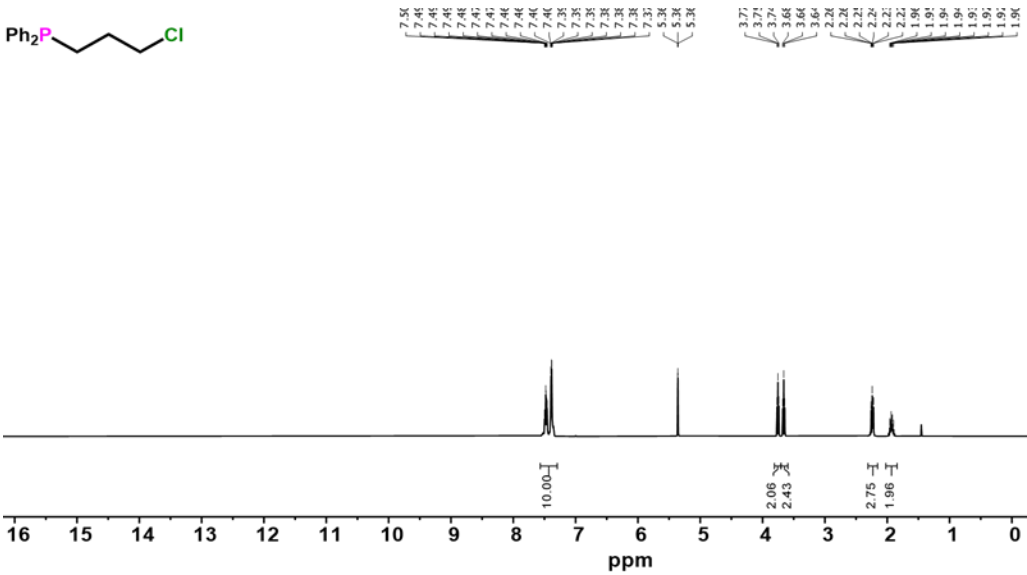

Figure 4.S1. ^{1}H NMR spectrum of (3-chloropropyl)diphenylphosphine in CD_2Cl_2.

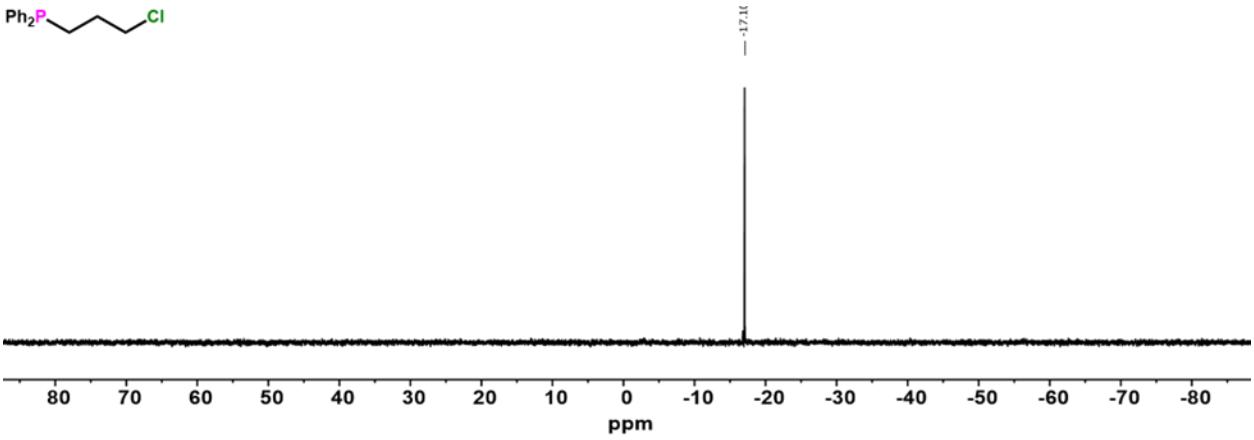

Figure 4.S2. $^{31}P\{^{1}H\}$ NMR spectrum of (3-chloropropyl)diphenylphosphine in CD_2Cl_2.

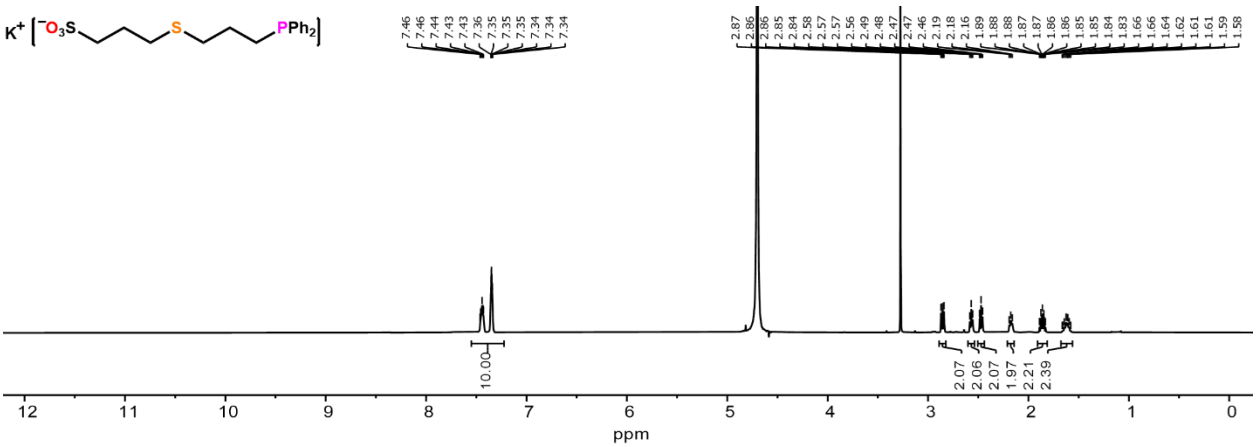

Figure 4.S3. ^{1}H NMR spectrum of the potassium salt of **1** in D_2O.

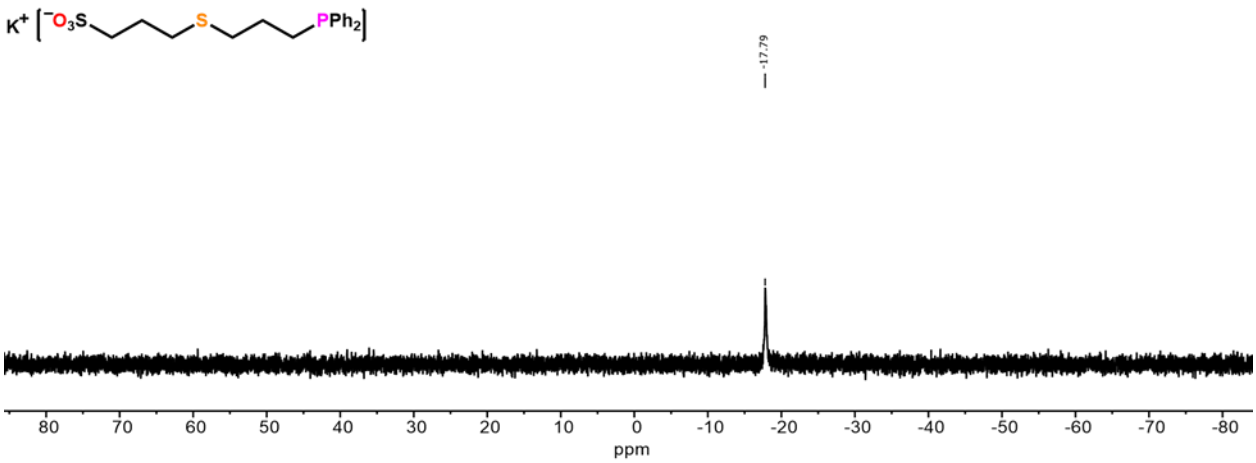

Figure 4.S4. $^{31}P\{^{1}H\}$ NMR spectrum of the potassium salt of **1** in D_2O.

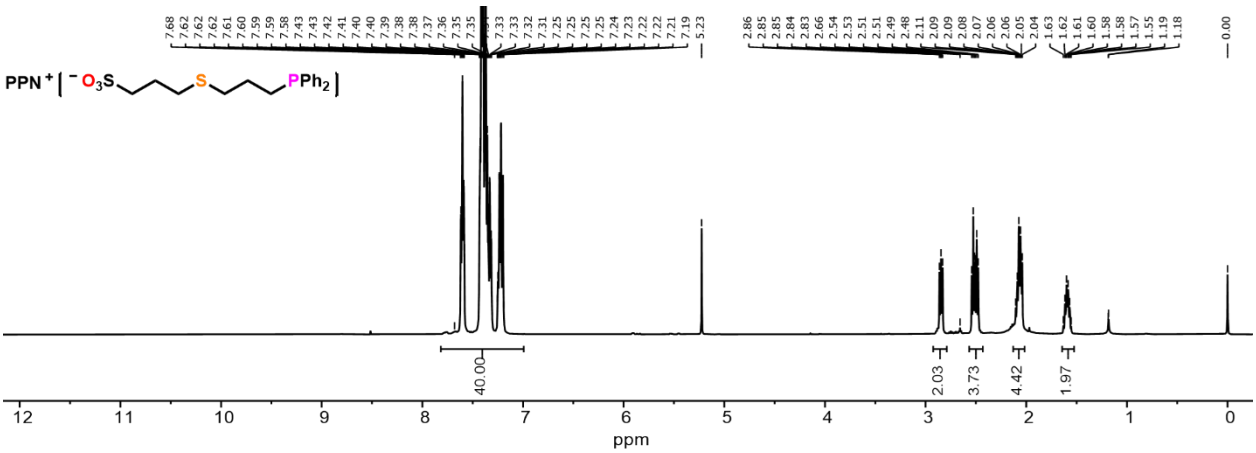

Figure 4.S5. ^{1}H NMR spectrum of **1** in CD_2Cl_2.

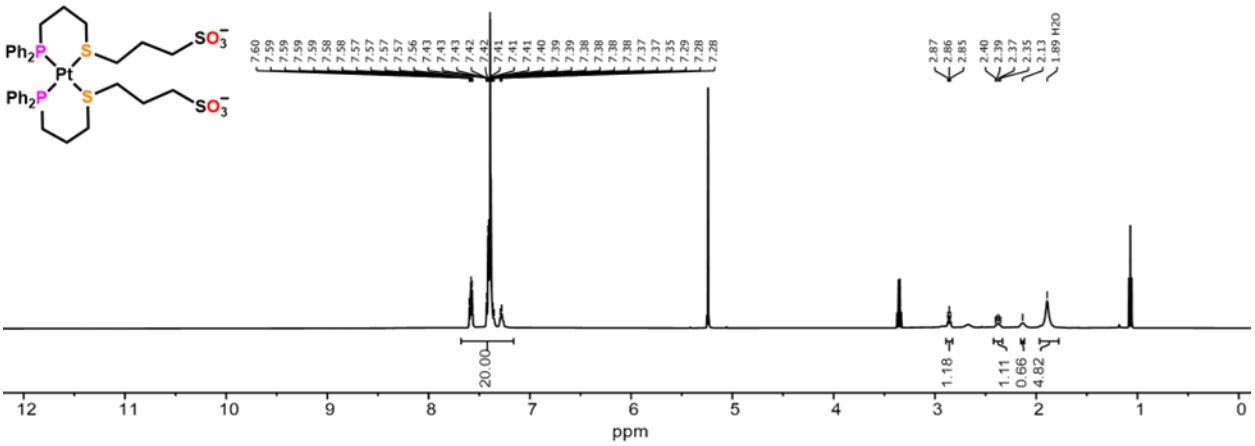

Figure 4.S6. ^{1}H NMR spectrum of **2** in CD_2Cl_2

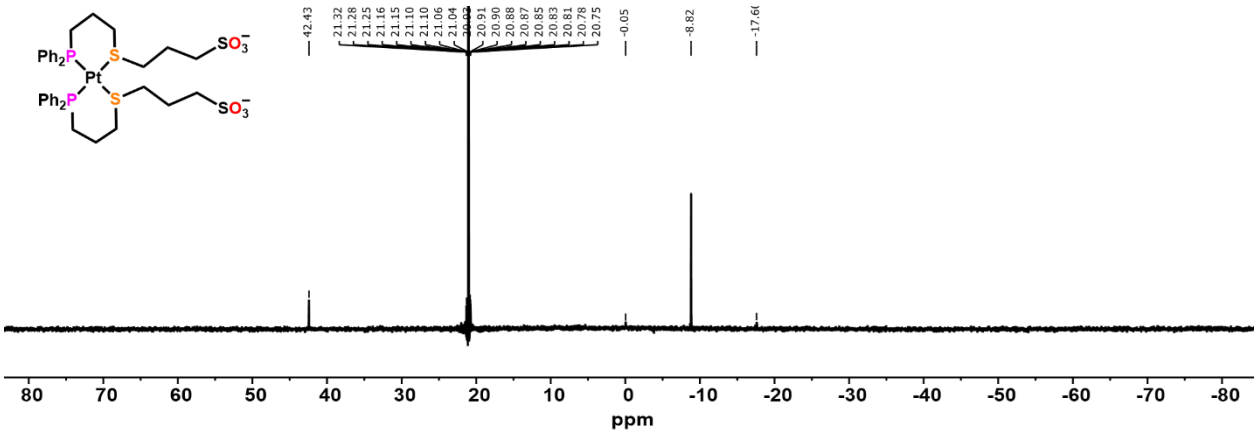

Figure 4.S7. $^{31}P\{^{1}H\}$ NMR spectrum of **2** in CD_2Cl_2.

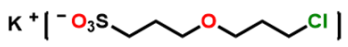

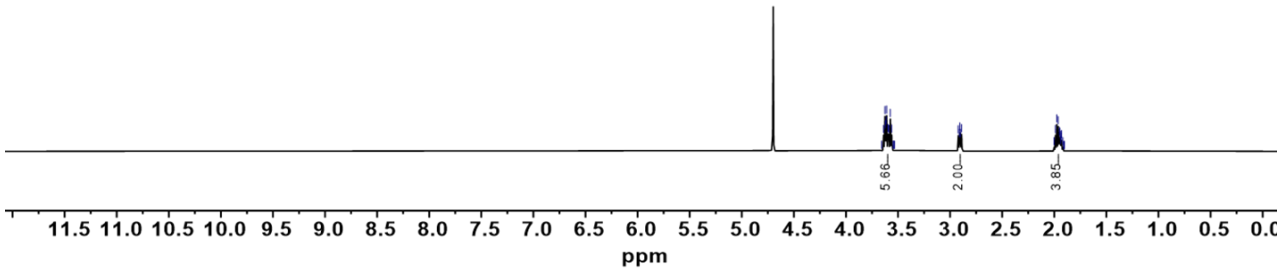

Figure 4.S8. ^{1}H NMR spectrum of potassium 3-chloropropyl 3-sulfonatopropyl ether in D_2O.

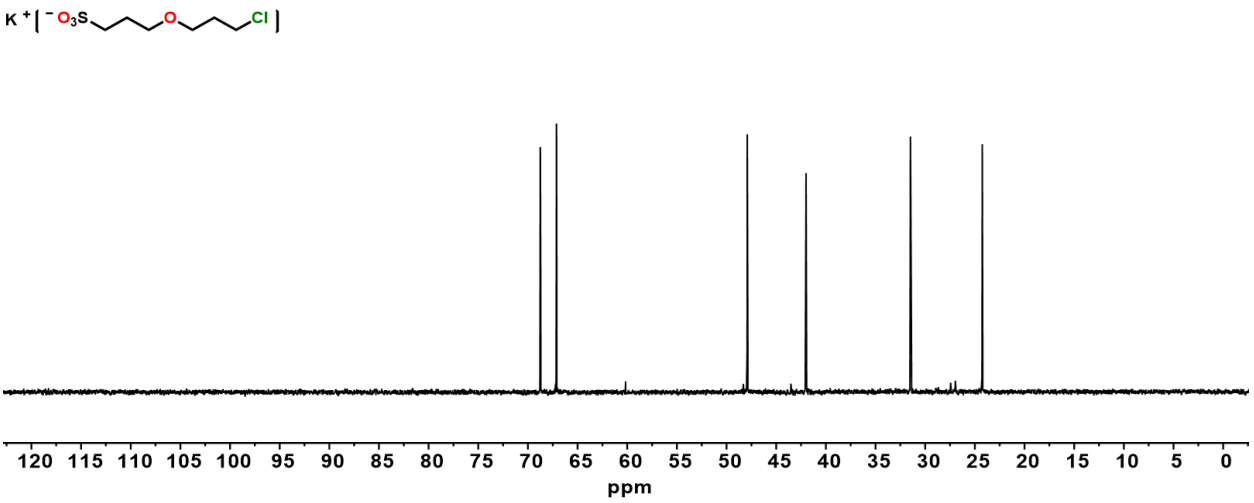

Figure 4.S9. $^{13}C\{^{1}H\}$ NMR spectrum of potassium 3-chloropropyl 3-sulfonatopropyl ether in D_2O.

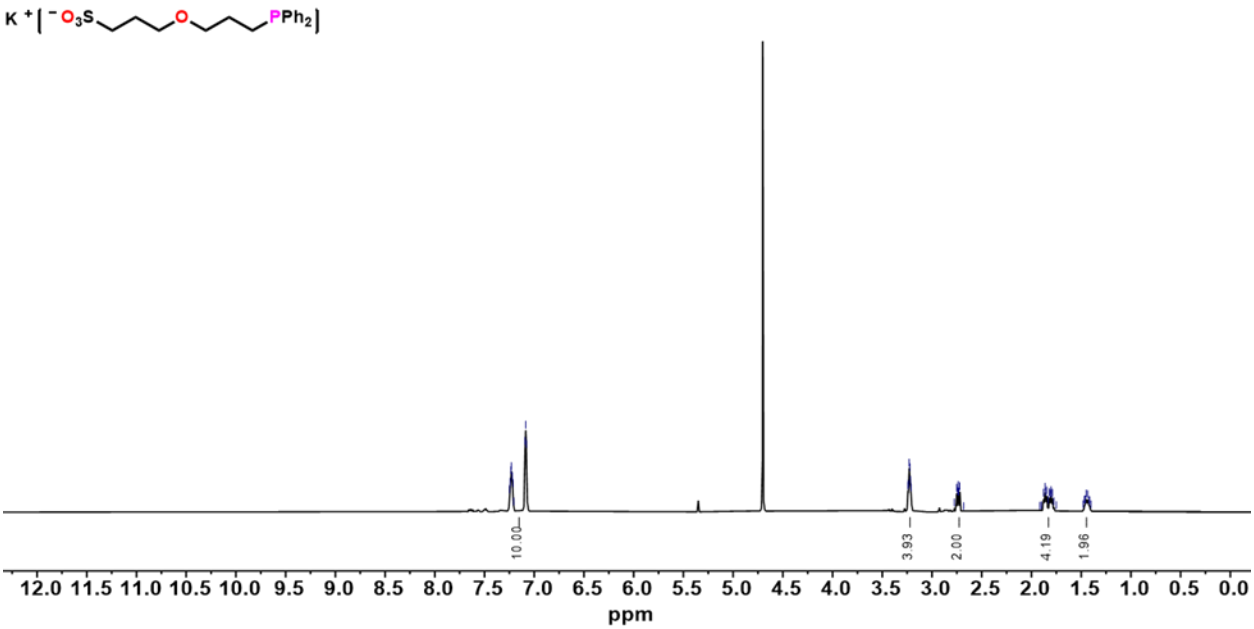

Figure 4.S10. ^{1}H NMR spectrum of the potassium salt of **3** in D_2O.

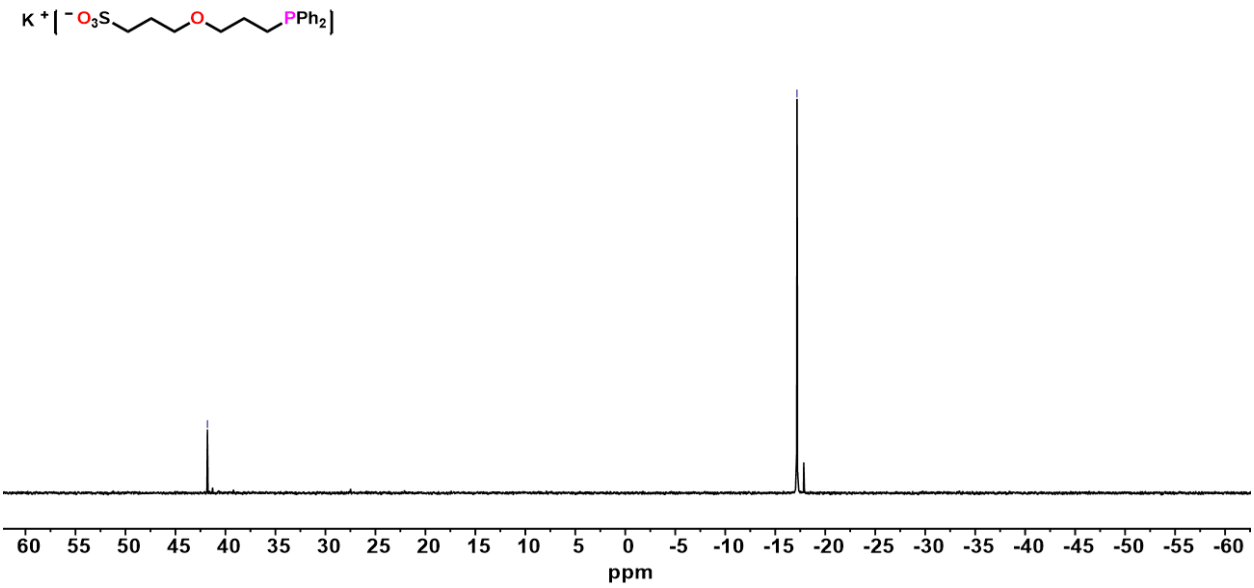

Figure 4.S11. $^{31}P\{^{1}H\}$ NMR spectrum of the potassium salt of **3** in D_2O.

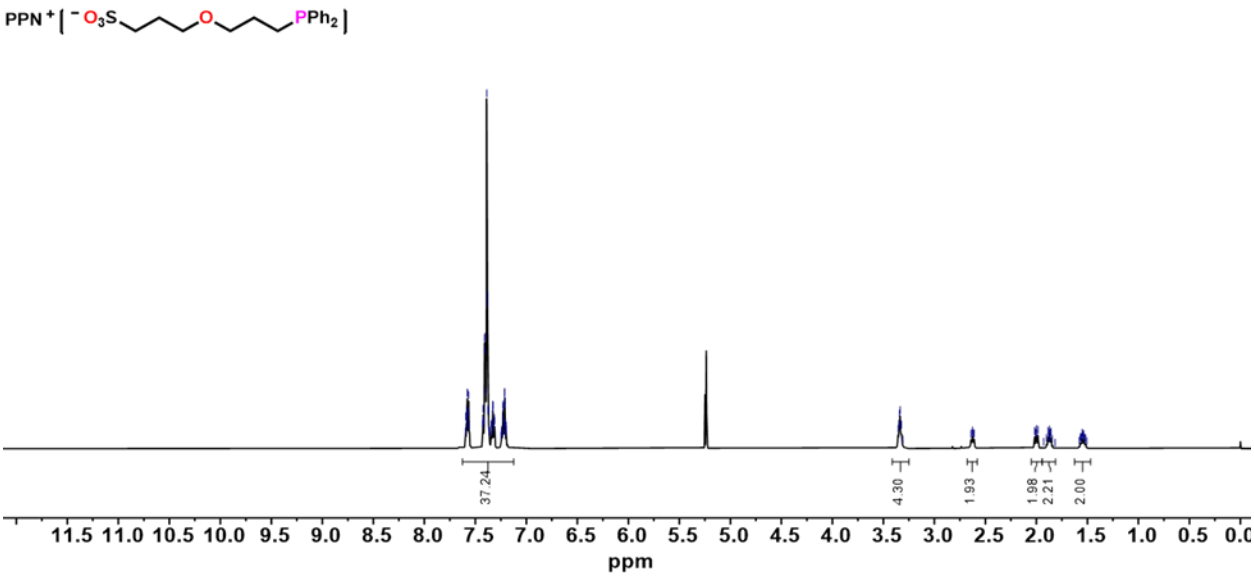

Figure 4.S12. ^{1}H NMR spectrum of **3** in CD_2Cl_2.

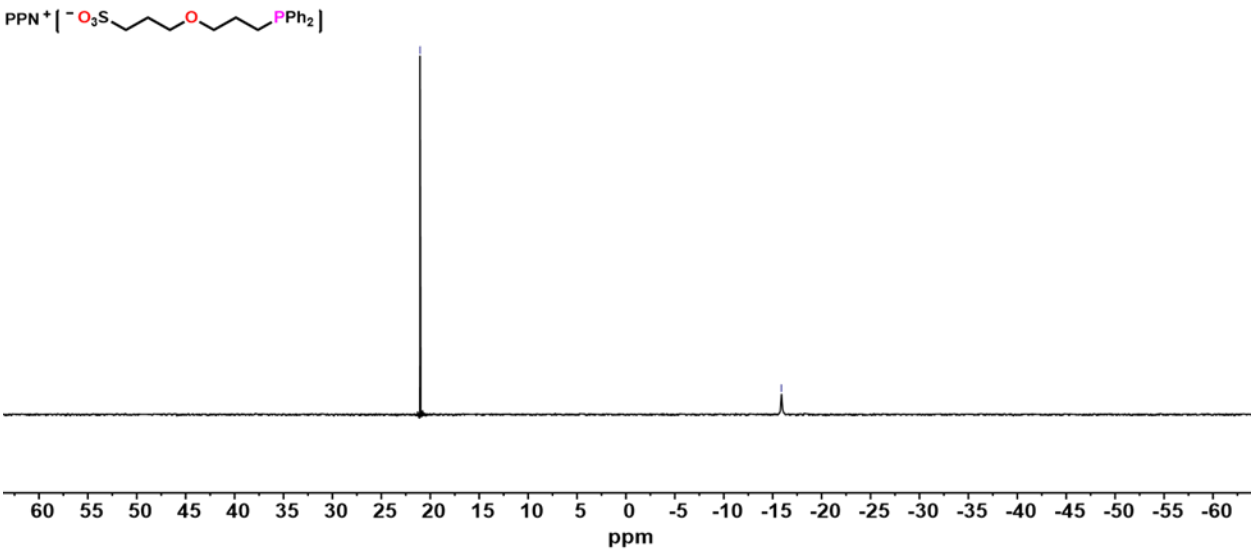

Figure 4.S13. $^{31}P\{^{1}H\}$ NMR spectrum of **3** in CD_2Cl_2.

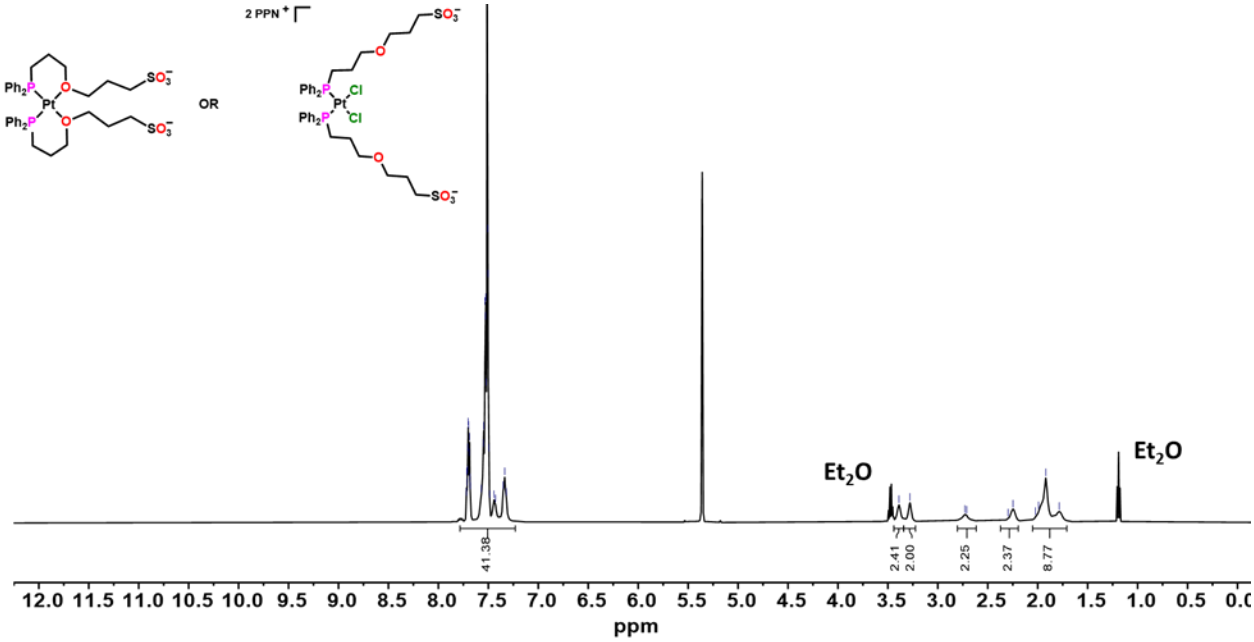

Figure 4.S14. ^{1}H NMR spectrum of **4-Open** or **4-Closed** in CD_2Cl_2. Note the presence of trace Et_2O that does not affect assignment.

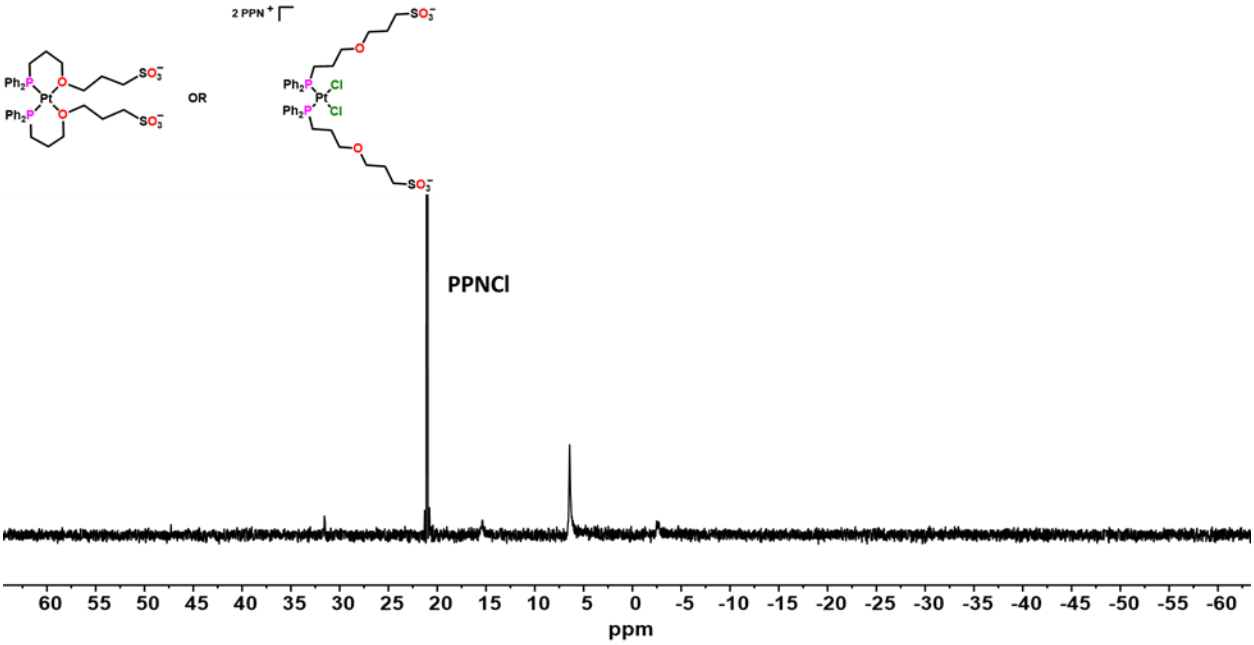

Figure 4.S15. $^{31}P\{^{1}H\}$ NMR spectrum of **4-Ope**n or **4-Closed** in CD_2Cl_2. Note the presence of excess PPNCl that does not affect assignments.

Chapter 5

Summary and Future Work

5.1 Summary

As societies' need to address emerging challenges in catalysis, data storage, healthcare, and environmental remediation continues to grow, nano- and supramolecular chemists have been called to action to synthesize novel materials with emergent properties. A bottom-up approach, in which molecular subunits are chosen based on their chemical and physical properties, has remained a powerful stratagy for the design of next-generation functional materials. Coordination chemistry and coordination compounds are well-suited for material design due to the large varieties of electronic and structural states that can be accessed through simple chemical modification (e.g. metal ion identity, oxidation state, ligand field and donor strength, etc.). Indeed, a coordination chemistry approach has led to the realization of new classes of sensors, actuators, stimuli-responsive catalysts, magnets, and photonic materials. This dissertation has focused on using coordination chemistry for the design of metal-organic magnets and stimuli-responsive materials, namely magnetic and stimuli-responsive coordination polymers and steps toward developing stimuli-responsive molecular tweezers that function in water.

Chapters 2 and 3 focused on the design of coordination polymers. In Chapter 2, we used coordination chemistry to assemble a new series of 2D iron-quinoid magnets with the general formula $(Me_4N)_2Fe_2{}^{R}L_3$ (R = OMe, Cl, Br, or NO_2). The frameworks were characterized by X-ray crystallography, Mössbauer spectroscopy, and Raman spectroscopy. All the frameworks undergo a spontaneous electron transfer from Fe^{II} to the bridging benzoquinoid ligands during synthesis such that the final materials contain a ratio of the dianionic ${}^{R}L^{2-}$ and the radical trianionic ${}^{R}L^{3\bullet-}$, determined by the identity of the benzoquinoid functional group. Importantly, SQUID magnetometry revealed that the magnetic ordering temperatures of the framework are greatly impacted by the nature of the ligand substituent with the NO_2-functionalized $(Me_4N)_2Fe_2{}^{NO_2}L_3$

displaying an ordering temperature above that of liquid nitrogen, T_c = 90 K. These results are attributed to differences in the relative oxidation states of each framework.

In Chapter 3, we used the WLA to supramolecular chemistry to design a new series of crystalline, stimuli-responsive coordination polymers. The coordination polymers were assembled via the reaction of a closed, pyridine-functionalized WLA monomer complex with a Cu^{II}-source to obtain three isostructural 1D zig-zag chains. All chains were analyzed by SCXRD, and as a model material for the series, one of the coordination polymer's response to traditional WLA chemical effectors (e.g. Cl^- anions) was investigated. Upon exposure, it disassembled into its molecular components, namely the fully-open congener of the WLA monomer complex. This work illustrates that the assembly and disassembly of a crystalline coordination polymer can be controlled via the structural state of the WLA molecular subunit. Importantly, it further demonstrates that the WLA is a viable and promising method for the design and synthesis of stimuli-responsive, dynamic crystalline coordination polymers, a material that had been hitherto challenging to access for the WLA platform.

Finally, in Chapter 4, we continued our focus on the WLA platform by summarizing efforts toward expanding its reversible structural regulation to also function within aqueous environments. We see this work as a first step towards developing WLA-biopolymer conjugates, specifically WLA-DNA conjugates (*infra vide*), for the construction of stimuli-responsive and reconfigurable DNA architectures that can function in a site-specific, targeted manner. However, to realize such a system, the WLA must operate within the aqueous environment necessary for development of DNA-based systems and materials. This has remained an immense challenge as previous water-soluble WLA complexes could only be toggled irreversibly. The work discussed within Chapter 4 details the synthesis of two new water-soluble WLA complexes synthesized to overcome this

challenge. However, the complexes displayed unique spectral characterization features due to their structure (e.g. three carbons bridging the “strong” and “weak” link) that made the assessment of their properties challenging in comparison to previously synthesized WLA complexes. Therefore, it was determined that future work should focus on complexes with thioether and ether water-soluble, hemilabile ligands featuring two carbon bridging units, the more traditional WLA design.

Taken together, the work presented within this dissertation illustrates only a small portion of the materials and structures that are accessible with a coordination chemistry approach. From magnetic materials to designer catalysts and stimuli-responsive polymers, coordination chemistry provides a vast toolbox to the discerning nano- and supramolecular chemist to build novel and increasingly complex materials with desirable and emergent properties.

5.2 Future Work

Building upon the advances in the WLA detailed within Chapters 3 and 4, we envision two major avenues for future work: 1) the design of stimuli-responsive 3D MOFs enabled via the WLA and 2) the regulation of DNA conformation in solution through WLA-DNA conjugates.

5.2.1 Stimuli-Responsive 3D Metal-Organic Frameworks Constructed from Addressable WLA Building Blocks

While we have reported the first crystalline WLA-ICP, two challenges remained in the design of future dynamic WLA extended solids. Firstly, upon effector binding to WLA subunits, the material completely disassembled. This disassembly limits the utility of the WLA-ICP system, but one can envision a WLA-ICP that can be switched between two crystalline phases. To achieve such materials, stronger metal-ligand interactions between the WLA monomer complexes and an SBU is necessary. We hypothesize that such a material may be synthesized via the inclusion of

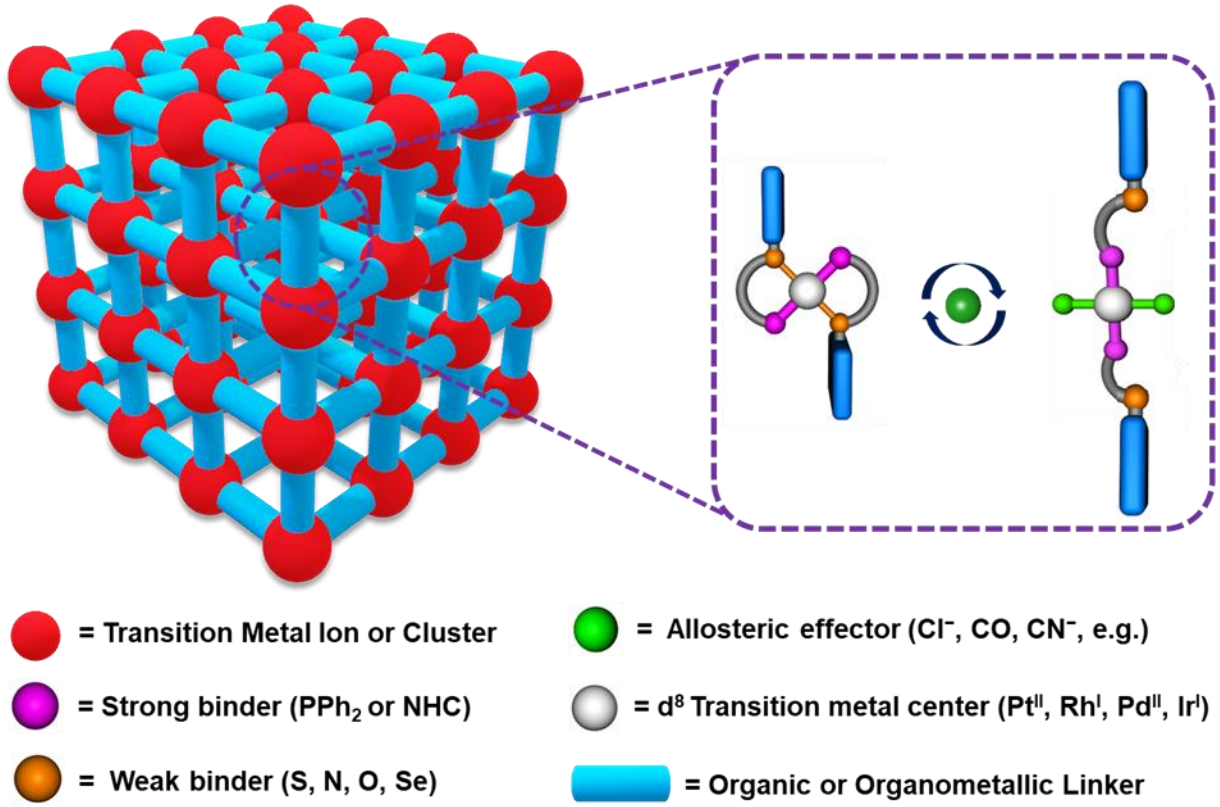

Figure 5.1. The proposed WLA-MOF material. Transition metal ions or clusters are linked together by WLA complexes that can be systematically opened and closed upon effector binding and abstraction. The inherent porosity of the 3D material is expected to aid in effector diffusion and enable post-synthetic modifications and functionality.

carboxylate moieties as the SBUs in WLA complexes. Carboxylate groups have comparable affinities to transition metal ions as pyridine moieties but benefit from their anionic and bidentate nature. The increase in stability afforded by the chelate effect can potentially allow the coordination bonds formed to survive the structural transformation. Secondly, the 1D nature of the synthesized series severely limits diffusion and mass transport of other chemical species throughout the material. Future work should be targeted towards the construction of 3D MOF architectures. The highly porous nature of MOFs makes them ideal candidates for a vast number of potential applications as their large pores and high surface areas permit facial diffusion of chemical species throughout their structures. We hypothesize utilizing the recently reported *trans*-WLA complexes will enable the assembly of the 3D architectures with WLA subunits (**Figure**

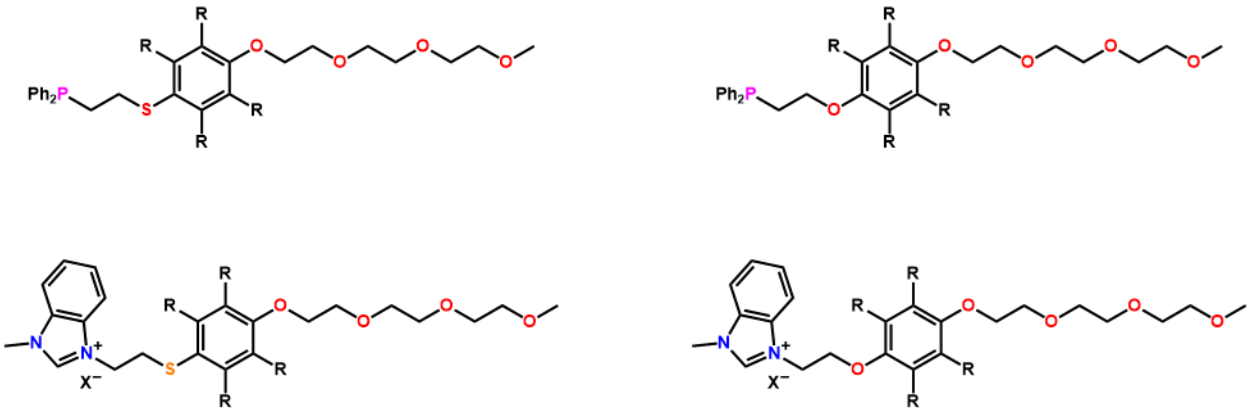

Scheme 5.1. The proposed hemilabile ligand series. This series retains the more traditional hemilabile ligand design utilized within the WLA with two methylene carbons bridging the "strong-" and "weak-" links. The short poly(ethylene glycol) chain appended to the end of the ligands is expected to grant amphiphilicity for the corresponding WLA complexes, permitting their characterization in both water and organic solvents.

5.1).[180] We expect that a WLA-MOF would have potential applications in stimuli-responsive guest uptake and release, catalysis, and chemical sensing.

5.2.2 Regulating DNA Conformation in Solution through WLA-DNA Conjugates

As noted in Chapter 4, work currently underway seeks to graft WLA complexes onto biopolymers and proteins to afford new forms of stimuli-responsive biomaterials, and two new hemilabile ligands and their corresponding WLA complexes were synthesized to discern the structural design elements necessary to enable reversible, structural regulation of WLA complexes in water. However, it was determined that unique features of the hemilabile ligands in comparison to ones previously employed in the WLA led to difficulty in the structural characterization in water, rendering the current system unsuitable to continue the investigation. Therefore, future work should turn towards hemilabile ligand systems that are more reminiscent of traditional NHC and phosphine-based hemilabile ligands of previous WLA complexes (**Scheme 5.1**). The four proposed hemilabile ligands feature two methylene units bridging the "strong-" and "weak-" links and a short poly(ethylene glycol) chain to provide amphiphilicity to their corresponding WLA complexes, allowing for characterization within both aqueous and organic environments. Finally,

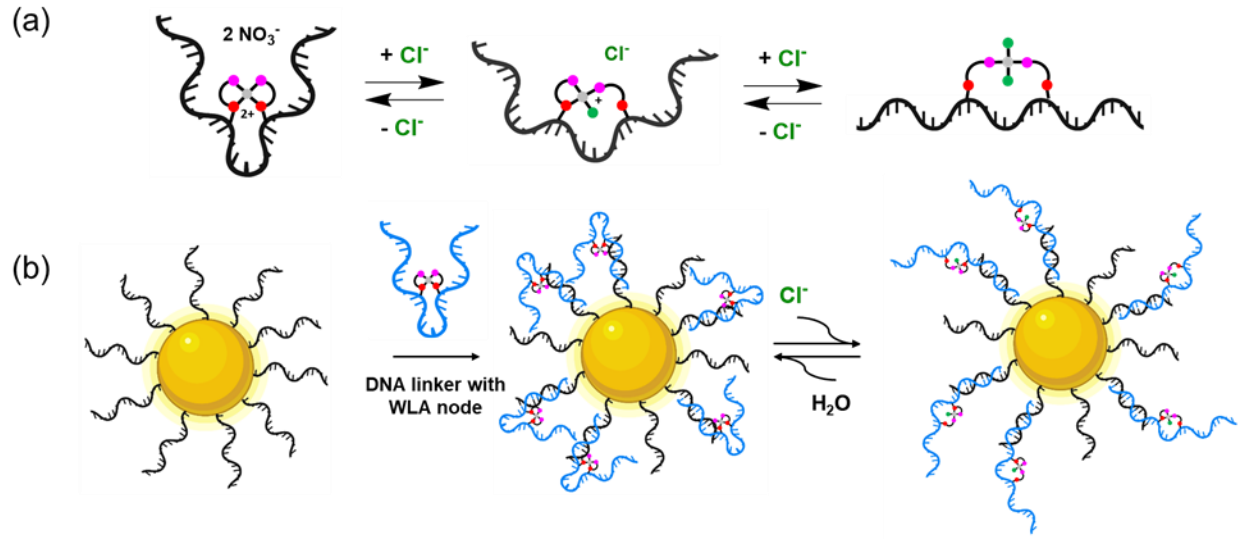

Figure 5.2. By controlling DNA conformation in solution, WLA-DNA conjugates are expected to enable stimuli-responsive reconfiguration of colloidal crystal assembly. (a) The solution conformation will be controlled via appended WLA complexes. When closed, the single stranded DNA will be forced into a compact, kinked macrocycle structure that can be open to the more flexible, conformationally free form open effector binding. (b) By blocking hybridization interactions between neighboring programmable atom equivalents (PAEs), the closed WLA-DNA macrocycles will prevent crystallization pathways. Upon systematic opening the structures, interactions between PAEs will be permitted, allowing one to control crystallization outcomes in solution.

the inclusion of an aryl-thioether and -ether groups will permit further tuning of the "weak" link donor strength by modification of the aromatic rings (e.g. addition of fluoro- and perfluoro groups).[141]

Our work in understanding the aqueous coordination chemistry of WLA complexes builds towards our ultimate goal of designing a new types of stimuli-responsive biomacromolecular materials, and future work will be focused on the synthesis and application of WLA-DNA conjugates (**Figure 5.2**). DNA is an attractive target due to its ubiquitous use and nearly unparalleled tunability as a bonding agent in programmable materials. Current strategies to achieve stimuli-responsiveness in these materials leverage the innate stimuli-responsiveness of certain DNA sequences through processes such as strand displacement, i-motif transformation, or triplet-duplex switching. However, these techniques require the use of predetermined nucleobase sequences. We hypothesize that by appending WLA complexes to single-stranded DNA, the local

conformation of any arbitrary DNA sequence, and therefore the assembly outcomes, can be controlled through the WLA structural node. By blocking hybridization interactions between neighboring programmable atom equivalents (PAEs), closed WLA-DNA macrocycles will prevent crystallization pathways, and by systematically opening the structures by exposing nanoparticles to effector ions in solution, interactions between PAEs will be permitted. Through this work, we will gain insights into how molecular level transformations can be translated into nanoscale changes in colloidal crystal bonding.

REFERENCES

1. Yaghi, O. M.; O'Keeffe, M.; Ockwig, N. W.; Chae, H. K.; Eddaoudi, M.; Kim, J. Reticular synthesis and the design of new materials. *Nature* **2003,** *423* (6941), 705-714. 10.1038/nature01650.
2. Long, J. R.; Yaghi, O. M. The pervasive chemistry of metal-organic frameworks. *Chem. Soc. Rev.* **2009,** *38* (5), 1213-1214. 10.1039/b903811f.
3. Zhou, H. C.; Long, J. R.; Yaghi, O. M. Introduction to metal-organic frameworks. *Chem. Rev.* **2012,** *112* (2), 673-674. 10.1021/cr300014x.
4. Kitagawa, S.; Kitaura, R.; Noro, S. Functional porous coordination polymers. *Angew. Chem. Int. Ed. Engl.* **2004,** *43* (18), 2334-2375. 10.1002/anie.200300610.
5. Yin, Z.; Wan, S.; Yang, J.; Kurmoo, M.; Zeng, M. H. Recent advances in post-synthetic modification of metal-organic frameworks: New types and tandem reactions. *Coord. Chem. Rev.* **2019,** *378*, 500-512. 10.1016/j.ccr.2017.11.015.
6. Dechambenoit, P.; Long, J. R. Microporous magnets. *Chem. Soc. Rev.* **2011,** *40* (6), 3249-3265. 10.1039/c0cs00167h.
7. Thorarinsdottir, A. E.; Harris, T. D. Metal-Organic Framework Magnets. *Chem. Rev.* **2020,** *120* (16), 8716-8789. 10.1021/acs.chemrev.9b00666.
8. Lee, J.; Farha, O. K.; Roberts, J.; Scheidt, K. A.; Nguyen, S. T.; Hupp, J. T. Metal-organic framework materials as catalysts. *Chem. Soc. Rev.* **2009,** *38* (5), 1450-1459. 10.1039/b807080f.
9. Kreno, L. E.; Leong, K.; Farha, O. K.; Allendorf, M.; Van Duyne, R. P.; Hupp, J. T. Metal-organic Framework Materials as Chemical Sensors. *Chem. Rev.* **2012,** *112* (2), 1105-1125. 10.1021/cr200324t.
10. Karmakar, A.; Samanta, P.; Desai, A. V.; Ghosh, S. K. Guest-Responsive Metal-Organic Frameworks as Scaffolds for Separation and Sensing Applications. *Acc. Chem. Res.* **2017,** *50* (10), 2457-2469. 10.1021/acs.accounts.7b00151.
11. Miller, J. S.; Epstein, A. J. Organic and Organometallic Molecular Magnetic-Materials - Designer Magnets. *Angew. Chem., Int. Ed.* **1994,** *33* (4), 385-415. DOI 10.1002/anie.199403851.
12. Miller, J. S. Magnetically ordered molecule-based materials. *Chem. Soc. Rev.* **2011,** *40* (6), 3266-3296. 10.1039/c0cs00166j.
13. Miller, J. S. Organic- and molecule-based magnets. *Mater. Today* **2014,** *17* (5), 224-235. 10.1016/j.mattod.2014.04.023.
14. Meihaus, K. R.; Long, J. R. Actinide-based single-molecule magnets. *Dalton Trans.* **2015,** *44* (6), 2517-2528. 10.1039/c4dt02391a.
15. Layfield, R. A. Organometallic Single-Molecule Magnets. *Organometallics* **2014,** *33* (5), 1084-1099. 10.1021/om401107f.
16. Woodruff, D. N.; Winpenny, R. E.; Layfield, R. A. Lanthanide Single-Molecule Magnets. *Chem. Rev.* **2013,** *113* (7), 5110-5148. 10.1021/cr400018q.
17. Guo, F. S.; Day, B. M.; Chen, Y. C.; Tong, M. L.; Mansikkamaki, A.; Layfield, R. A. A Dysprosium Metallocene Single-Molecule Magnet Functioning at the Axial Limit. *Angew. Chem. Int. Ed. Engl.* **2017,** *56* (38), 11445-11449. 10.1002/anie.201705426.

18. Guo, F. S.; He, M.; Huang, G. Z.; Giblin, S. R.; Billington, D.; Heinemann, F. W.; Tong, M. L.; Mansikkamaki, A.; Layfield, R. A. Discovery of a Dysprosium Metallocene Single-Molecule Magnet with Two High-Temperature Orbach Processes. *Inorg. Chem.* **2022,** *61* (16), 6017-6025. 10.1021/acs.inorgchem.1c03980.
19. Gould, C. A.; McClain, K. R.; Reta, D.; Kragskow, J. G. C.; Marchiori, D. A.; Lachman, E.; Choi, E. S.; Analytis, J. G.; Britt, R. D.; Chilton, N. F.; Harvey, B. G.; Long, J. R. Ultrahard magnetism from mixed-valence dilanthanide complexes with metal-metal bonding. *Science* **2022,** *375* (6577), 198-202. 10.1126/science.abl5470.
20. Sagawa, M.; Fujimura, S.; Togawa, N.; Yamamoto, H.; Matsuura, Y. New material for permanent magnets on a base of Nd and Fe. *J. Appl. Phys.* **1984,** *55* (6), 2083-2087. 10.1063/1.333572.
21. Herzer, G. Nanocrystalline Soft Magnetic-Materials. *J. Magn. Magn. Mater.* **1992,** *112* (1-3), 258-262. Doi 10.1016/0304-8853(92)91168-S.
22. Dionne, G. F. *Magnetic oxides*. Springer: 2009; Vol. 14.
23. Kramers, H. A. L'interaction Entre les Atomes Magnétogènes dans un Cristal Paramagnétique. *Physica* **1934,** *1* (1-6), 182-192. 10.1016/s0031-8914(34)90023-9.
24. Anderson, P. W. Antiferromagnetism - Theory of Superexchange Interaction. *Phys. Rev.* **1950,** *79* (2), 350-356. DOI 10.1103/PhysRev.79.350.
25. Kurmoo, M. Magnetic metal-organic frameworks. *Chem. Soc. Rev.* **2009,** *38* (5), 1353-1379. 10.1039/b804757j.
26. Demir, S.; Jeon, I. R.; Long, J. R.; Harris, T. D. Radical ligand-containing single-molecule magnets. *Coord. Chem. Rev.* **2015,** *289*, 149-176. 10.1016/j.ccr.2014.10.012.
27. Freeman, A. J.; Watson, R. E. Theory of Direct Exchange in Ferromagnetism. *Phys. Rev.* **1961,** *124* (5), 1439-&. DOI 10.1103/PhysRev.124.1439.
28. Coronado, E.; Tsukerblat, B. S.; Georges, R. Exchange Interactions I: Mechanisms. In *Molecular Magnetism: From Molecular Assemblies to the Devices*, Springer Netherlands: 1996; pp 65-84.
29. Perlepe, P.; Oyarzabal, I.; Mailman, A.; Yquel, M.; Platunov, M.; Dovgaliuk, I.; Rouzières, M.; Négrier, P.; Mondieig, D.; Suturina, E. A.; Dourges, M.-A.; Bonhommeau, S.; Musgrave, R. A.; Pedersen, K. S.; Chernyshov, D.; Wilhelm, F.; Rogalev, A.; Mathonière, C.; Clérac, R. Metal-organic magnets with large coercivity and ordering temperatures up to 242 °C. *Science* **2020,** *370* (6516), 587-592. doi:10.1126/science.abb3861.
30. Pedersen, K. S.; Perlepe, P.; Aubrey, M. L.; Woodruff, D. N.; Reyes-Lillo, S. E.; Reinholdt, A.; Voigt, L.; Li, Z.; Borup, K.; Rouzieres, M.; Samohvalov, D.; Wilhelm, F.; Rogalev, A.; Neaton, J. B.; Long, J. R.; Clerac, R. Formation of the layered conductive magnet $CrCl_2(pyrazine)_2$ through redox-active coordination chemistry. *Nat. Chem.* **2018,** *10* (10), 1056-1061. 10.1038/s41557-018-0107-7.
31. Min, K. S.; DiPasqual, A. G.; Golen, J. A.; Rheingold, A. L.; Arif, A. M.; Miller, J. S. Synthesis, structure, and magnetic properties of valence ambiguous dinuclear antiferromagnetically coupled cobalt and ferromagnetically coupled iron complexes containing the chloranilate^{2-} and the significantly stronger coupling chloranilate$^{\bullet 3-}$ radical trianion. *J. Am. Chem. Soc.* **2007,** *129* (18), 6056-6056. 10.1021/ja0716958.
32. Thorarinsdottir, A. E.; Bjornsson, R.; Harris, T. D. Insensitivity of Magnetic Coupling to Ligand Substitution in a Series of Tetraoxolene Radical-Bridged Fe_2 Complexes. *Inorg. Chem.* **2020,** *59* (7), 4634-4649. 10.1021/acs.inorgchem.9b03736.

33. Jeon Ie, R.; Park, J. G.; Xiao, D. J.; Harris, T. D. An Azophenine Radical-Bridged Fe_2 Single-Molecule Magnet with Record Magnetic Exchange Coupling. *J. Am. Chem. Soc.* **2013,** *135* (45), 16845-16848. 10.1021/ja409927v.
34. Guo, D.; McCusker, J. K. Spin Exchange Effects on the Physicochemical Properties of Tetraoxolene-Bridged Bimetallic Complexes. *Inorg. Chem.* **2007,** *46* (8), 3257-3274. 10.1021/ic070005y.
35. Clérac, R.; O'Kane, S.; Cowen, J.; Ouyang, X.; Heintz, R.; Zhao, H.; Bazile, M. J.; Dunbar, K. R. Glassy Magnets Composed of Metals Coordinated to 7,7,8,8-tetracyanoquinodimethane: M(TCNQ)2 (M = Mn, Fe, Co, Ni). *Chem. Mater.* **2003,** *15* (9), 1840-1850. 10.1021/cm021053d.
36. Manriquez, J. M.; Yee, G. T.; McLean, R. S.; Epstein, A. J.; Miller, J. S. A room-temperature molecular/organic-based magnet. *Science* **1991,** *252* (5011), 1415-1417. 10.1126/science.252.5011.1415.
37. Jain, R.; Kabir, K.; Gilroy, J. B.; Mitchell, K. A.; Wong, K. C.; Hicks, R. G. High-temperature metal-organic magnets. *Nature* **2007,** *445* (7125), 291-294. 10.1038/nature05439.
38. Rinehart, J. D.; Fang, M.; Evans, W. J.; Long, J. R. A N_2^{3-} radical-bridged terbium complex exhibiting magnetic hysteresis at 14 K. *J. Am. Chem. Soc.* **2011,** *133* (36), 14236-14239. 10.1021/ja206286h.
39. Rinehart, J. D.; Fang, M.; Evans, W. J.; Long, J. R. Strong exchange and magnetic blocking in N_2^{3-}-radical-bridged lanthanide complexes. *Nat. Chem.* **2011,** *3* (7), 538-542. 10.1038/nchem.1063.
40. Taliaferro, M. L.; Thorum, M. S.; Miller, J. S. Room-temperature organic-based magnet (T_c~50 °C) containing tetracyanobenzene and hexacarbonylvanadate(–I). *Angew. Chem. Int. Ed. Engl.* **2006,** *45* (32), 5326-5331. 10.1002/anie.200600988.
41. Lodish, H.; Berk, A.; Kaiser, C. A.; Kaiser, C.; Krieger, M.; Scott, M. P.; Bretscher, A.; Ploegh, H.; Matsudaira, P. *Molecular cell biology*. Macmillan: 2008.
42. Frieden, E. Non-covalent interactions. Key to biological flexibility and specificity. *J. Chem. Educ.* **1975,** *52* (12), 754-756. 10.1021/ed052p754.
43. Monod, J.; Changeux, J. P.; Jacob, F. Allosteric proteins and cellular control systems. *J. Mol. Biol.* **1963,** *6* (4), 306-329. 10.1016/s0022-2836(63)80091-1.
44. Cui, Q.; Karplus, M. Allostery and cooperativity revisited. *Protein Sci.* **2008,** *17* (8), 1295-1307. 10.1110/ps.03259908.
45. Laskowski, R. A.; Gerick, F.; Thornton, J. M. The structural basis of allosteric regulation in proteins. *FEBS Lett.* **2009,** *583* (11), 1692-1698. 10.1016/j.febslet.2009.03.019.
46. Hsia, C. C. Respiratory function of hemoglobin. *N. Engl. J. Med.* **1998,** *338* (4), 239-247. 10.1056/NEJM199801223380407.
47. Perutz, M. F. Stereochemistry of cooperative effects in haemoglobin. *Nature* **1970,** *228* (5273), 726-739. 10.1038/228726a0.
48. Eaton, W. A.; Henry, E. R.; Hofrichter, J.; Mozzarelli, A. Is cooperative oxygen binding by hemoglobin really understood? *Nat. Struct. Biol.* **1999,** *6* (4), 351-358. 10.1038/7586.
49. Schormann, N.; Hayden, K. L.; Lee, P.; Banerjee, S.; Chattopadhyay, D. An overview of structure, function, and regulation of pyruvate kinases. *Protein Sci.* **2019,** *28* (10), 1771-1784. 10.1002/pro.3691.
50. Mattevi, A.; Bolognesi, M.; Valentini, G. The allosteric regulation of pyruvate kinase. *FEBS Lett.* **1996,** *389* (1), 15-19. 10.1016/0014-5793(96)00462-0.

51. Carbonell, J.; Feliu, J. E.; Marco, R.; Sols, A. Pyruvate kinase. Classes of regulatory isoenzymes in mammalian tissues. *Eur. J. Biochem.* **1973,** *37* (1), 148-156. 10.1111/j.1432-1033.1973.tb02969.x.
52. Pedersen, C. J. Cyclic polyethers and their complexes with metal salts. *J. Am. Chem. Soc.* **1967,** *89* (26), 7017-7036. 10.1021/ja01002a035.
53. Seidel, S. R.; Stang, P. J. High-Symmetry Coordination Cages via Self-Assembly. *Acc. Chem. Res.* **2002,** *35* (11), 972-983. 10.1021/ar010142d.
54. Leininger, S.; Olenyuk, B.; Stang, P. J. Self-Assembly of Discrete Cyclic Nanostructures Mediated by Transition Metals. *Chem. Rev.* **2000,** *100* (3), 853-908. 10.1021/cr9601324.
55. Chakrabarty, R.; Mukherjee, P. S.; Stang, P. J. Supramolecular Coordination: Self-Assembly of finite Two- and Three-Dimensional Ensembles. *Chem. Rev.* **2011,** *111* (11), 6810-6918. 10.1021/cr200077m.
56. Caulder, D. L.; Raymond, K. N. Supermolecules by Design. *Acc. Chem. Res.* **1999,** *32* (11), 975-982. DOI 10.1021/ar970224v.
57. Gianneschi, N. C.; Masar, M. S., 3rd; Mirkin, C. A. Development of a Coordination Chemistry-Based Approach for Functional Supramolecular Structures. *Acc. Chem. Res.* **2005,** *38* (11), 825-837. 10.1021/ar980101q.
58. Lifschitz, A. M.; Rosen, M. S.; McGuirk, C. M.; Mirkin, C. A. Allosteric Supramolecular Coordination Constructs. *J. Am. Chem. Soc.* **2015,** *137* (23), 7252-7261. 10.1021/jacs.5b01054.
59. Fujita, M.; Yazaki, J.; Ogura, K. Preparation of a macrocyclic polynuclear complex, $[(en)Pd(4,4'\text{-bpy})]_4(NO_3)_8$ (en = ethylenediamine, bpy = bipyridine), which recognizes an organic molecule in aqueous media. *J. Am. Chem. Soc.* **1990,** *112* (14), 5645-5647. 10.1021/ja00170a042.
60. Makoto, F.; Jun, Y.; Katsuyuki, O. Spectroscopic Observation of Self-Assembly of a Macrocyclic Tetranuclear Complex Composed of Pt^{2+} and 4,4′-Bipyridine. *Chem. Lett.* **1991,** *20* (6), 1031-1032. 10.1246/cl.1991.1031.
61. Stang, P. J.; Cao, D. H. Transition-Metal Based Cationic Molecular Boxes - Self-Assembly of Macrocyclic Platinum(II) and Palladium(II) Tetranuclear Complexes. *J. Am. Chem. Soc.* **1994,** *116* (11), 4981-4982. DOI 10.1021/ja00090a051.
62. Caulder, D. L.; Bruckner, C.; Powers, R. E.; Konig, S.; Parac, T. N.; Leary, J. A.; Raymond, K. N. Design, formation and properties of tetrahedral M_4L_4 and M_4L_6 supramolecular clusters. *J. Am. Chem. Soc.* **2001,** *123* (37), 8923-8938. 10.1021/ja0104507.
63. Cook, T. R.; Stang, P. J. Recent Developments in the Preparation and Chemistry of Metallacycles and Metallacages via Coordination. *Chem. Rev.* **2015,** *115* (15), 7001-7045. 10.1021/cr5005666.
64. Sepehrpour, H.; Fu, W.; Sun, Y.; Stang, P. J. Biomedically Relevant Self-Assembled Metallacycles and Metallacages. *J. Am. Chem. Soc.* **2019,** *141* (36), 14005-14020. 10.1021/jacs.9b06222.
65. Farrell, J. R.; Mirkin, C. A.; Guzei, I. A.; Liable-Sands, L. M.; Rheingold, A. L. The Weak-Link Approach to the Synthesis of Inorganic Macrocycles. *Angew. Chem. Int. Ed. Engl.* **1998,** *37* (4), 465-467. 10.1002/(SICI)1521-3773(19980302)37:4<465::AID-ANIE465>3.0.CO;2-A.

66. Oliveri, C. G.; Ulmann, P. A.; Wiester, M. J.; Mirkin, C. A. Heteroligated supramolecular coordination complexes formed via the halide-induced ligand rearrangement reaction. *Acc. Chem. Res.* **2008,** *41* (12), 1618-1629. 10.1021/ar800025w.
67. Holliday, B. J.; Farrell, J. R.; Mirkin, C. A.; Lam, K. C.; Rheingold, A. L. Metal-directed assembly of triple-layered fluorescent metallocyclophanes. *J. Am. Chem. Soc.* **1999,** *121* (26), 6316-6317. DOI 10.1021/ja991140f.
68. Kourkine, I. V.; Slone, C. S.; Mirkin, C. A.; Liable-Sands, L. M.; Rheingold, A. L. Small Molecule-Induced Intramolecular Electron "Pitch and Catch" in a Rhodium(I) Complex with Substitutionally Inert Redox-Active Ligands. *Inorg. Chem.* **1999,** *38* (12), 2758-2759. 10.1021/ic990193v.
69. Dixon, F. M.; Eisenberg, A. H.; Farrell, J. R.; Mirkin, C. A.; Liable-Sands, L. M.; Rheingold, A. L. Neutral macrocycles via halide-induced ring opening of binuclear condensed intermediates. *Inorg. Chem.* **2000,** *39* (16), 3432-3433. 10.1021/ic000062q.
70. Holliday, B. J.; Jeon, Y. M.; Mirkin, C. A.; Stern, C. L.; Incarvito, C. D.; Zakharov, L. N.; Sommer, R. D.; Rheingold, A. L. Probing the mechanistic and energetic basis for the weak-link approach to supramolecular coordination complexes. *Organometallics* **2002,** *21* (26), 5713-5725. 10.1021/om020739c.
71. Holliday, B. J.; Ulmann, P. A.; Mirkin, C. A.; Stern, C. L.; Zakharov, L. N.; Rheingold, A. L. Systematic Study of the Role of Ligand Structure in the Formation of Homobinuclear Rhodium Macrocycles Formed via the Weak-Link Approach. *Organometallics* **2004,** *23* (8), 1671-1679. 10.1021/om030611a.
72. Khoshbin, M. S.; Ovchinnikov, M. V.; Mirkin, C. A.; Zakharov, L. N.; Rheingold, A. L. Binuclear ruthenium macrocycles formed via the weak-link approach. *Inorg. Chem.* **2005,** *44* (3), 496-501. 10.1021/ic048975y.
73. Ovchinnikov, M. V.; Holliday, B. J.; Mirkin, C. A.; Zakharov, L. N.; Rheingold, A. L. Threefold symmetric trimetallic macrocycles formed via the Weak-Link Approach. *Proc. Natl. Acad. Sci. U. S. A.* **2002,** *99* (8), 4927-4931. 10.1073/pnas.072690599.
74. Machan, C. W.; Spokoyny, A. M.; Jones, M. R.; Sarjeant, A. A.; Stern, C. L.; Mirkin, C. A. Plasticity of the nickel(II) coordination environment in complexes with hemilabile phosphino thioether ligands. *J. Am. Chem. Soc.* **2011,** *133* (9), 3023-3033. 10.1021/ja109624m.
75. Eisenberg, A. H.; Dixon, F. M.; Mirkin, C. A.; Stern, C. L.; Incarvito, C. D.; Rheingold, A. L. Binuclear palladium macrocycles synthesized via the weak-link approach. *Organometallics* **2001,** *20* (10), 2052-2058. 10.1021/om001042z.
76. Ulmann, P. A.; Brown, A. M.; Ovchinnikov, M. V.; Mirkin, C. A.; DiPasquale, A. G.; Rheingold, A. L. Spontaneous formation of heteroligated Pt^{II} complexes with chelating hemilabile ligands. *Chem. - Eur. J.* **2007,** *13* (16), 4529-4534. 10.1002/chem.200601837.
77. Ulmann, P. A.; Mirkin, C. A.; DiPasquale, A. G.; Liable-Sands, L. M.; Rheingold, A. L. Reversible Ligand Pairing and Sorting Processes Leading to Heteroligated Palladium(II) Complexes with Hemilabile Ligands. *Organometallics* **2009,** *28* (4), 1068-1074. 10.1021/om801060m.
78. Lifschitz, A. M.; Shade, C. M.; Spokoyny, A. M.; Mendez-Arroyo, J.; Stern, C. L.; Sarjeant, A. A.; Mirkin, C. A. Boron-dipyrromethene-functionalized hemilabile ligands as "turn-on" fluorescent probes for coordination changes in weak-link approach complexes. *Inorg. Chem.* **2013,** *52* (9), 5484-5492. 10.1021/ic400383t.

79. Liu, Y.; Zhou, J.; Wasielewski, M. R.; Xing, H.; Mirkin, C. A. A four-state fluorescent molecular switch. *Chem. Commun. (Cambridge, U. K.)* **2018,** *54* (85), 12041-12044. 10.1039/c8cc05159c.
80. Gianneschi, N. C.; Nguyen, S. T.; Mirkin, C. A. Signal amplification and detection via a supramolecular allosteric catalyst. *J. Am. Chem. Soc.* **2005,** *127* (6), 1644-1645. 10.1021/ja0437306.
81. Yoon, H. J.; Mirkin, C. A. PCR-like cascade reactions in the context of an allosteric enzyme mimic. *J. Am. Chem. Soc.* **2008,** *130* (35), 11590-11591. 10.1021/ja804076q.
82. Holliday, B. J.; Farrell, J. R.; Mirkin, C. A.; Lam, K. C.; Rheingold, A. L. Metal-directed assembly of triple-layered fluorescent metallocyclophanes. *J. Am. Chem. Soc.* **1999,** *121* (26), 6316-6317. DOI 10.1021/ja991140f.
83. Farrell, J. R.; Eisenberg, A. H.; Mirkin, C. A.; Guzei, I. A.; Liable-Sands, L. M.; Incarvito, C. D.; Rheingold, A. L.; Stern, C. L. Templated formation of binuclear macrocycles via hemilabile ligands. *Organometallics* **1999,** *18* (23), 4856-4868. DOI 10.1021/om990585+.
84. Dixon, F. M.; Eisenberg, A. H.; Farrell, J. R.; Mirkin, C. A.; Liable-Sands, L. M.; Rheingold, A. L. Neutral macrocycles via halide-induced ring opening of binuclear condensed intermediates. *Inorg. Chem.* **2000,** *39* (16), 3432-3433. 10.1021/ic000062q.
85. Masar, M. S.; Ovchinnikov, M. V.; Mirkin, C. A.; Zakharov, L. N.; Rheingold, A. L. Fine-Tuning the Weak-Link Approach: Effect of Ligand Electron Density on the Formation of Rhodium(I) and Iridium(I) Metallomacrocycles. *Inorg. Chem.* **2003,** *42* (21), 6851-6858. 10.1021/ic034393p.
86. Yoon, H. J.; Kuwabara, J.; Kim, J. H.; Mirkin, C. A. Allosteric supramolecular triple-layer catalysts. *Science* **2010,** *330* (6000), 66-69. 10.1126/science.1193928.
87. McGuirk, C. M.; Mendez-Arroyo, J.; Lifschitz, A. M.; Mirkin, C. A. Allosteric regulation of supramolecular oligomerization and catalytic activity via coordination-based control of competitive hydrogen-bonding events. *J. Am. Chem. Soc.* **2014,** *136* (47), 16594-16601. 10.1021/ja508804n.
88. Lifschitz, A. M.; Young, R. M.; Mendez-Arroyo, J.; Stern, C. L.; McGuirk, C. M.; Wasielewski, M. R.; Mirkin, C. A. An allosteric photoredox catalyst inspired by photosynthetic machinery. *Nat. Commun.* **2015,** *6* (1), 6541. 10.1038/ncomms7541.
89. Lifschitz, A. M.; Young, R. M.; Mendez-Arroyo, J.; McGuirk, C. M.; Wasielewski, M. R.; Mirkin, C. A. Cooperative Electronic and Structural Regulation in a Bioinspired Allosteric Photoredox Catalyst. *Inorg. Chem.* **2016,** *55* (17), 8301-8308. 10.1021/acs.inorgchem.6b00095.
90. d'Aquino, A. I.; Kean, Z. S.; Mirkin, C. A. Infinite Coordination Polymer Particles Composed of Stimuli Responsive Coordination Complex Subunits. *Chem. Mater.* **2017,** *29* (24), 10284-10288. 10.1021/acs.chemmater.7b03638.
91. Bogani, L.; Wernsdorfer, W. Molecular spintronics using single-molecule magnets. *Nat. Mater.* **2008,** *7* (3), 179-186. 10.1038/nmat2133.
92. Spaldin, N. A. *Magnetic materials : fundamentals and applications*. 2nd ed.; Cambridge University Press: Cambridge ; New York, 2011; p xiii, 274 p.
93. Gutfleisch, O.; Willard, M. A.; Bruck, E.; Chen, C. H.; Sankar, S. G.; Liu, J. P. Magnetic Materials and Devices for the 21st Century: Stronger, Lighter, and More Energy Efficient. *Adv. Mater.* **2011,** *23* (7), 821-842. 10.1002/adma.201002180.

94. DeGayner, J. A.; Jeon, I. R.; Sun, L.; Dinca, M.; Harris, T. D. 2D Conductive Iron-Quinoid Magnets Ordering up to T_c = 105 K via Heterogenous Redox Chemistry. *J. Am. Chem. Soc.* **2017,** *139* (11), 4175-4184. 10.1021/jacs.7b00705.
95. Maspoch, D.; Ruiz-Molina, D.; Veciana, J. Magnetic nanoporous coordination polymers. *J. Mater. Chem.* **2004,** *14* (18), 2713-2723. 10.1039/b407169g.
96. Motokawa, N.; Miyasaka, H.; Yamashita, M.; Dunbar, K. R. An electron-transfer ferromagnet with T_c = 107 K based on a three-dimensional $[Ru_2]_2TCNQ$ system. *Angew. Chem. Int. Ed. Engl.* **2008,** *47* (40), 7760-7763. 10.1002/anie.200802574.
97. Stone, K. H.; Stephens, P. W.; McConnell, A. C.; Shurdha, E.; Pokhodnya, K. I.; Miller, J. S. $Mn^{II}(TCNE)_{3/2}(I_3)_{1/2}$-A 3D Network-Structured Organic-Based Magnet and Comparison to a 2D Analog. *Adv. Mater.* **2010,** *22* (23), 2514-2519. 10.1002/adma.200904238.
98. Lapidus, S. H.; McConnell, A. C.; Stephens, P. W.; Miller, J. S. Structure and magnetic ordering of a 2-D $Mn^{II}(TCNE)I(OH_2)$ (TCNE = tetracyanoethylene) organic-based magnet (T_c = 171 K). *Chem. Commun. (Cambridge, U.K.)* **2011,** *47* (27), 7602-7604. 10.1039/c1cc10478k.
99. Neel, L. *Proprietes Magnetiques Des Ferrites - Ferrimagnetisme Et Antiferromagnetisme. *Ann Phys-Paris* **1948,** *3* (2), 137-198.
100. Caneschi, A.; Gatteschi, D.; Laugier, J.; Rey, P. Ferromagnetic Alternating Spin Chains. *J. Am. Chem. Soc.* **2002,** *109* (7), 2191-2192. 10.1021/ja00241a053.
101. Numata, Y.; Inoue, K.; Baranov, N.; Kurmoo, M.; Kikuchi, K. Field-induced ferrimagnetic state in a molecule-based magnet consisting of a Co(II) ion and a chiral triplet Bis(nitroxide) radical. *J. Am. Chem. Soc.* **2007,** *129* (32), 9902-9909. 10.1021/ja064828i.
102. Ma, X.; Suturina, E. A.; De, S.; Negrier, P.; Rouzieres, M.; Clerac, R.; Dechambenoit, P. A Redox-Active Bridging Ligand to Promote Spin Delocalization, High-Spin Complexes, and Magnetic Multi-Switchability. *Angew. Chem. Int. Ed. Engl.* **2018,** *57* (26), 7841-7845. 10.1002/anie.201803842.
103. Mondal, D.; Majee, M. C.; Kundu, S.; Mortel, M.; Abbas, G.; Endo, A.; Khusniyarov, M. M.; Chaudhury, M. Dinuclear Iron(III) and Cobalt(III) Complexes Featuring a Biradical Bridge: Their Molecular Structures and Magnetic, Spectroscopic, and Redox Properties. *Inorg. Chem.* **2018,** *57* (3), 1004-1016. 10.1021/acs.inorgchem.7b02340.
104. Kitagawa, S.; Kawata, S. Coordination compounds of 1,4-dihydroxybenzoquinone and its homologues. Structures and properties. *Coord. Chem. Rev.* **2002,** *224* (1-2), 11-34. Doi 10.1016/S0010-8545(01)00369-1.
105. Dei, A.; Gatteschi, D.; Pardi, L.; Russo, U. Tetraoxolene Radical Stabilization by the Interaction with Transition-Metal Ions. *Inorg. Chem.* **1991,** *30* (12), 2589-2594. DOI 10.1021/ic00012a006.
106. Min, K. S.; Dipasquale, A. G.; Rheingold, A. L.; White, H. S.; Miller, J. S. Observation of redox-induced electron transfer and spin crossover for dinuclear cobalt and iron complexes with the 2,5-di-tert-butyl-3,6-dihydroxy-1,4-benzoquinonate bridging ligand. *J. Am. Chem. Soc.* **2009,** *131* (17), 6229-6236. 10.1021/ja900909u.
107. Shilov, G. V.; Nikitina, Z. K.; Ovanesyan, N. S.; Aldoshin, S. M.; Makhaev, V. D. Phenazineoxonium chloranilatomanganate and chloranilatoferrate: synthesis, structure, magnetic properties, and Mossbauer spectra. *Russ. Chem. Bull.* **2011,** *60* (6), 1209-1219. 10.1007/s11172-011-0190-z.

108. Jeon Ie, R.; Negru, B.; Van Duyne, R. P.; Harris, T. D. A 2D Semiquinone Radical-Containing Microporous Magnet with Solvent-Induced Switching from T_c = 26 to 80 K. *J. Am. Chem. Soc.* **2015,** *137* (50), 15699-15702. 10.1021/jacs.5b10382.
109. Heinze, K.; Huttner, G.; Zsolnai, L.; Jacobi, A.; Schober, P. Electron transfer in dinuclear cobalt complexes with "non-innocent" bridging ligands. *Chem.-Eur. J.* **1997,** *3* (5), 732-743. DOI 10.1002/chem.19970030513.
110. Atzori, M.; Artizzu, F.; Sessini, E.; Marchio, L.; Loche, D.; Serpe, A.; Deplano, P.; Concas, G.; Pop, F.; Avarvari, N.; Mercuri, M. L. Halogen-bonding in a new family of tris(haloanilato)metallate(III) magnetic molecular building blocks. *Dalton Trans.* **2014,** *43* (19), 7006-7019. 10.1039/c4dt00127c.
111. Atzori, M.; Benmansour, S.; Minguez Espallargas, G.; Clemente-Leon, M.; Abherve, A.; Gomez-Claramunt, P.; Coronado, E.; Artizzu, F.; Sessini, E.; Deplano, P.; Serpe, A.; Mercuri, M. L.; Gomez Garcia, C. J. A family of layered chiral porous magnets exhibiting tunable ordering temperatures. *Inorg. Chem.* **2013,** *52* (17), 10031-10040. 10.1021/ic4013284.
112. Nagayoshi, K.; Kabir, M. K.; Tobita, H.; Honda, K.; Kawahara, M.; Katada, M.; Adachi, K.; Nishikawa, H.; Ikemoto, I.; Kumagai, H.; Hosokoshi, Y.; Inoue, K.; Kitagawa, S.; Kawata, S. Design of novel inorganic-organic hybrid materials based on iron-chloranilate mononuclear complexes: characteristics of hydrogen-bond-supported layers toward the intercalation of guests. *J. Am. Chem. Soc.* **2003,** *125* (1), 221-232. 10.1021/ja027895v.
113. Halis, S.; Inge, A. K.; Dehning, N.; Weyrich, T.; Reinsch, H.; Stock, N. Dihydroxybenzoquinone as Linker for the Synthesis of Permanently Porous Aluminum Metal-Organic Frameworks. *Inorg. Chem.* **2016,** *55* (15), 7425-7431. 10.1021/acs.inorgchem.6b00661.
114. DeGayner, J. A.; Wang, K.; Harris, T. D. A Ferric Semiquinoid Single-Chain Magnet via Thermally-Switchable Metal-Ligand Electron Transfer. *J. Am. Chem. Soc.* **2018,** *140* (21), 6550-6553. 10.1021/jacs.8b03949.
115. Chen, J.; Sekine, Y.; Komatsumaru, Y.; Hayami, S.; Miyasaka, H. Thermally Induced Valence Tautomeric Transition in a Two-Dimensional Fe-Tetraoxolene Honeycomb Network. *Angew. Chem. Int. Ed. Engl.* **2018,** *57* (37), 12043-12047. 10.1002/anie.201807556.
116. Mydosh, J. A. *Spin glasses : an experimental introduction*. Taylor & Francis: London ; Washington, DC, 1993; p xi, 256 p.
117. Huang, Y.; Gao, H.; Twamley, B.; Shreeve, J. M. Highly Dense Nitranilates-Containing Nitrogen-Rich Cations. *Chem. - Eur. J.* **2009,** *15* (4), 917-923. 10.1002/chem.200801976.
118. Sheldrick, G. SHELXT: Integrating space group determination and structure solution. *Acta Crystallogr., Sect. A: Cryst. Phys., Diffr., Theor. Gen. Crystallogr.* **2014,** *70*, C1437-C1437. Doi 10.1107/S2053273314085623.
119. Dolomanov, O. V.; Bourhis, L. J.; Gildea, R. J.; Howard, J. A. K.; Puschmann, H. OLEX2: a complete structure solution, refinement and analysis program. *J. Appl. Crystallogr.* **2009,** *42*, 339-341. 10.1107/S0021889808042726.
120. Sheldrick, G. M. Crystal structure refinement with SHELXL. *Acta Crystallogr., Sect. C: Struct. Chem.* **2015,** *71* (Pt 1), 3-8. 10.1107/S2053229614024218.
121. Bain, G. A.; Berry, J. F. Diamagnetic corrections and Pascal's constants. *J. Chem. Educ.* **2008,** *85* (4), 532-536. DOI 10.1021/ed085p532.

122. Changeux, J.-P.; Edelstein, S. J. Allosteric Receptors after 30 Years. *Neuron* **1998,** *21* (5), 959-980. 10.1016/s0896-6273(00)80616-9.
123. Changeux, J. P.; Edelstein, S. J. Allosteric mechanisms of signal transduction. *Science* **2005,** *308* (5727), 1424-1428. 10.1126/science.1108595.
124. Goodey, N. M.; Benkovic, S. J. Allosteric regulation and catalysis emerge via a common route. *Nat. Chem. Bio.* **2008,** *4* (8), 474-482. 10.1038/nchembio.98.
125. Motlagh, H. N.; Wrabl, J. O.; Li, J.; Hilser, V. J. The ensemble nature of allostery. *Nature* **2014,** *508* (7496), 331-339. 10.1038/nature13001.
126. Cook, T. R.; Zheng, Y. R.; Stang, P. J. Metal-Organic Frameworks and Self-Assembled Supramolecular Coordination Complexes: Comparing and Contrasting the Design, Synthesis, and Functionality of Metal-Organic Materials. *Chem. Rev.* **2013,** *113* (1), 734-777. 10.1021/cr3002824.
127. Albrecht, M. Dicatechol ligands: novel building-blocks for metallo-supramolecular chemistry. *Chem. Soc. Rev.* **1998,** *27* (4), 281-287. DOI 10.1039/a827281z.
128. Caulder, D. L.; Raymond, K. N. The rational design of high symmetry coordination clusters. *Dalton T* **1999,** (8), 1185-1200. DOI 10.1039/a808370c.
129. Cook, T. R.; Stang, P. J. Coordination-Driven Supramolecular Macromolecules via the Directional Bonding Approach. Springer International Publishing: 2013; pp 229-248.
130. Faiz, J. A.; Heitz, V.; Sauvage, J. P. Design and synthesis of porphyrin-containing catenanes and rotaxanes. *Chem. Soc. Rev.* **2009,** *38* (2), 422-442. 10.1039/b710908n.
131. Lee, S. J.; Lin, W. Chiral metallocycles: rational synthesis and novel applications. *Acc. Chem. Res.* **2008,** *41* (4), 521-537. 10.1021/ar700216n.
132. Lehn, J. M. Perspectives in chemistry--steps towards complex matter. *Angew. Chem. Int. Ed Engl.* **2013,** *52* (10), 2836-2850. 10.1002/anie.201208397.
133. Ronson, T. K.; Zarra, S.; Black, S. P.; Nitschke, J. R. Metal-organic container molecules through subcomponent self-assembly. *Chem. Commun. (Cambridge, U. K.)* **2013,** *49* (25), 2476-2490. 10.1039/c2cc36363a.
134. Seidel, S. R.; Stang, P. J. High-symmetry coordination cages via self-assembly. *Acc. Chem. Res.* **2002,** *35* (11), 972-983. 10.1021/ar010142d.
135. Smulders, M. M.; Riddell, I. A.; Browne, C.; Nitschke, J. R. Building on architectural principles for three-dimensional metallosupramolecular construction. *Chem. Soc. Rev.* **2013,** *42* (4), 1728-1754. 10.1039/c2cs35254k.
136. Wang, Z. J.; Clary, K. N.; Bergman, R. G.; Raymond, K. N.; Toste, F. D. A supramolecular approach to combining enzymatic and transition metal catalysis. *Nat. Chem.* **2013,** *5* (2), 100-103. 10.1038/nchem.1531.
137. Wurthner, F.; You, C. C.; Saha-Moller, C. R. Metallosupramolecular squares: from structure to function. *Chem. Soc. Rev.* **2004,** *33* (3), 133-146. 10.1039/b300512g.
138. Yan, X.; Cook, T. R.; Pollock, J. B.; Wei, P.; Zhang, Y.; Yu, Y.; Huang, F.; Stang, P. J. Responsive supramolecular polymer metallogel constructed by orthogonal coordination-driven self-assembly and host/guest interactions. *J. Am. Chem. Soc.* **2014,** *136* (12), 4460-4463. 10.1021/ja412249k.
139. Yan, X.; Li, S.; Pollock, J. B.; Cook, T. R.; Chen, J.; Zhang, Y.; Ji, X.; Yu, Y.; Huang, F.; Stang, P. J. Supramolecular polymers with tunable topologies via hierarchical coordination-driven self-assembly and hydrogen bonding interfaces. *Proc. Natl. Acad. Sci. U.S.A.* **2013,** *110* (39), 15585-15590. 10.1073/pnas.1307472110.

140. Yoshizawa, M.; Klosterman, J. K.; Fujita, M. Functional molecular flasks: new properties and reactions within discrete, self-assembled hosts. *Angew. Chem. Int. Ed. Engl.* **2009,** *48* (19), 3418-3438. 10.1002/anie.200805340.
141. Kennedy, R. D.; Machan, C. W.; McGuirk, C. M.; Rosen, M. S.; Stern, C. L.; Sarjeant, A. A.; Mirkin, C. A. General strategy for the synthesis of rigid weak-link approach platinum(II) complexes: tweezers, triple-layer complexes, and macrocycles. *Inorg. Chem.* **2013,** *52* (10), 5876-5888. 10.1021/ic302855f.
142. Liu, Y.; Kean, Z. S.; d'Aquino, A. I.; Manraj, Y. D.; Mendez-Arroyo, J.; Mirkin, C. A. Palladium(II) Weak-Link Approach Complexes Bearing Hemilabile N-Heterocyclic Carbene-Thioether Ligands. *Inorg. Chem.* **2017,** *56* (10), 5902-5910. 10.1021/acs.inorgchem.7b00543.
143. Sassano, C. A.; Mirkin, C. A. Degenerate Exchange-Reactions - a Novel and General Way to Determine the Thermodynamic Perturbations on Transition-Metal Complexes That Result from Ligand Oxidation. *J. Am. Chem. Soc.* **1995,** *117* (45), 11379-11380. DOI 10.1021/ja00150a052.
144. Singewald, E. T.; Mirkin, C. A.; Stern, C. L. A Redox-Switchable Hemilabile Ligand: Electrochemical Control of the Coordination Environment of a RhI Complex. *Angew. Chem., Int. Ed.* **1995,** *34* (15), 1624-1627. 10.1002/anie.199516241.
145. Singewald, E. T.; Shi, X. B.; Mirkin, C. A.; Schofer, S. J.; Stern, C. L. Novel Hemilabile (Phosphinoalkyl)arene Ligands: Mechanistic Investigation of All Unusual Intramolecular, Arene-Arene Exchange Reaction. *Organometallics* **1996,** *15* (13), 3062-3069. DOI 10.1021/om960114c.
146. Allgeier, A. M.; Slone, C. S.; Mirkin, C. A.; LiableSands, L. M.; Yap, G. P. A.; Rheingold, A. L. Electrochemically controlling ligand binding affinity for transition metals via RHLs: The importance of electrostatic effects. *J. Am. Chem. Soc.* **1997,** *119* (3), 550-559. DOI 10.1021/ja963008a.
147. Slone, C. S.; Mirkin, C. A.; Yap, G. P. A.; Guzei, I. A.; Rheingold, A. L. Oxidation-State-Dependent Reactivity and Catalytic Properties of a Rh(I) Complex Formed from a Redox-Switchable Hemilabile Ligand. *J. Am. Chem. Soc.* **1997,** *119* (44), 10743-10753. DOI 10.1021/ja9723601.
148. Allgeier, A. M.; Singewald, E. T.; Mirkin, C. A.; Stern, C. L. [Rh(η^4-((η^5-C_5H_4)$OCH_2CH_2P(C_6H_5)_2)_2$Fe)]BF_4: An Olefin Hydrogenation Catalyst and the First Rhodium(I) cis-Phosphine-cis-Ether Complex Characterized by Single-Crystal X-ray Diffraction Methods. *Organometallics* **2002,** *13* (8), 2928-2930. 10.1021/om00020a005.
149. Cheng, H. F.; d'Aquino, A. I.; Barroso-Flores, J.; Mirkin, C. A. A Redox-Switchable, Allosteric Coordination Complex. *J. Am. Chem. Soc.* **2018,** *140* (44), 14590-14594. 10.1021/jacs.8b09321.
150. Bigdeli, F.; Lollar, C. T.; Morsali, A.; Zhou, H. C. Switching in Metal-Organic Frameworks. *Angew. Chem. Int. Ed. Engl.* **2020,** *59* (12), 4652-4669. 10.1002/anie.201900666.
151. Kitagawa, S.; Uemura, K. Dynamic porous properties of coordination polymers inspired by hydrogen bonds. *Chem. Soc. Rev.* **2005,** *34* (2), 109-119. 10.1039/b313997m.
152. McConnell, A. J.; Wood, C. S.; Neelakandan, P. P.; Nitschke, J. R. Stimuli-Responsive Metal-Ligand Assemblies. *Chem. Rev.* **2015,** *115* (15), 7729-7793. 10.1021/cr500632f.

153. Balogh-Hergovich, v.; Speier, G. Reaction of copper(I) chloride pyridine complexes with dioxygen. A kinetic study. *Transition Met. Chem.* **1982,** *7* (3), 177-180. 10.1007/bf01035837.
154. Rodgers, M. T.; Stanley, J. R.; Amunugama, R. Periodic trends in the binding of metal ions to pyridine studied by threshold collision-induced dissociation and density functional theory. *J. Am. Chem. Soc.* **2000,** *122* (44), 10969-10978. 10.1021/ja0027923.
155. Dobrawa, R.; Ballester, P.; Saha-Möller, C. R.; Würthner, F. Thermodynamics of 2,2′:6′,2″-Terpyridine-Metal Ion Complexation. In *Metal-Containing and Metallosupramolecular Polymers and Materials*, American Chemical Society: 2006; Vol. 928, pp 43-62.
156. Batten, S. R.; Jeffery, J. C.; Ward, M. D. Studies of the construction of coordination polymers using linear pyridyl-donor ligands. *Inorg. Chim. Acta* **1999,** *292* (2), 231-237. Doi 10.1016/S0020-1693(99)00203-0.
157. Du, M.; Bu, X. H.; Guo, Y. M.; Liu, H.; Batten, S. R.; Ribas, J.; Mak, T. C. First Cu(II) diamondoid net with 2-fold interpenetrating frameworks. The role of anions in the construction of the supramolecular arrays. *Inorg. Chem.* **2002,** *41* (19), 4904-4908. 10.1021/ic025559+.
158. Kitaura, R.; Fujimoto, K.; Noro, S.-i.; Kondo, M.; Kitagawa, S. A Pillared-Layer Coordination Polymer Network Displaying Hysteretic Sorption: $[Cu_2(pzdc)_2(dpyg)]_n$ (pzdc= Pyrazine-2,3-dicarboxylate; dpyg=1,2-Di(4-pyridyl)glycol). *Angew. Chem. Int. Ed.* **2002,** *41* (1), 133-135. 10.1002/1521-3773(20020104)41:1<133::Aid-anie133>3.0.Co;2-r.
159. Rather, B.; Zaworotko, M. J. A 3D metal-organic network, $[Cu_2(glutarate)_2(4,4'$-bipyridine)], that exhibits single-crystal to single-crystal dehydration and rehydration. *Chem. Commun. (Cambridge, U.K.)* **2003,** (7), 830-831. 10.1039/b301219k.
160. Tong, M. L.; Li, L. J.; Mochizuki, K.; Chang, H. C.; Chen, X. M.; Li, Y.; Kitagawa, S. A novel three-dimensional coordination polymer constructed with mixed-valence dimeric copper(I,II) units. *Chem. Commun. (Cambridge, U.K.)* **2003,** (3), 428-429. 10.1039/b210914j.
161. Mori, W.; Takamizawa, S.; Kato, C. N.; Ohmura, T.; Sato, T. Molecular-level design of efficient microporous materials containing metal carboxylates: inclusion complex formation with organic polymer, gas-occlusion properties, and catalytic activities for hydrogenation of olefins. *Microporous Mesoporous Mater.* **2004,** *73* (1-2), 31-46. 10.1016/j.micromeso.2004.02.019.
162. Park, J.; Li, J. R.; Chen, Y. P.; Yu, J.; Yakovenko, A. A.; Wang, Z. U.; Sun, L. B.; Balbuena, P. B.; Zhou, H. C. A versatile metal-organic framework for carbon dioxide capture and cooperative catalysis. *Chem. Commun. (Cambridge, U.K.)* **2012,** *48* (80), 9995-9997. 10.1039/c2cc34622b.
163. Yoon, M.; Srirambalaji, R.; Kim, K. Homochiral Metal-Organic Frameworks for Asymmetric Heterogeneous Catalysis. *Chem. Rev.* **2012,** *112* (2), 1196-1231. 10.1021/cr2003147.
164. del Zotto, A.; Mezzetti, A.; Rigo, P.; Bressan, M.; Morandini, F.; Morvillo, A. Synthesis and NMR studies of palladium(II) and platinum(II) complexes with hybrid bidentate ligands $Ph_2P(CH_2)_2SR$. *Inorg. Chim. Acta* **1989,** *158* (2), 151-158. 10.1016/s0020-1693(00)80828-2.

165. Tate, C. W.; Gee, A. D.; Vilar, R.; White, A. J. P.; Long, N. J. Reversible carbon monoxide binding at copper(I) P–S–X (X = N, O) coordination polymers. *J. Organomet. Chem.* **2012,** *715*, 39-42. 10.1016/j.jorganchem.2012.05.032.
166. Rosen, M. S.; Stern, C. L.; Mirkin, C. A. Heteroligated Pt^{II} Weak-Link Approach complexes using hemilabile *N*-heterocyclic carbene–thioether and phosphino–thioether ligands. *Chem. Sci.* **2013,** *4* (11), 4193. 10.1039/c3sc51557e.
167. Mendez-Arroyo, J.; Barroso-Flores, J.; Lifschitz, A. M.; Sarjeant, A. A.; Stern, C. L.; Mirkin, C. A. A multi-state, allosterically-regulated molecular receptor with switchable selectivity. *J. Am. Chem. Soc.* **2014,** *136* (29), 10340-10348. 10.1021/ja503506a.
168. Lifschitz, A. M.; Young, R. M.; Mendez-Arroyo, J.; Roznyatovskiy, V. V.; McGuirk, C. M.; Wasielewski, M. R.; Mirkin, C. A. Chemically regulating Rh(I)-Bodipy photoredox switches. *Chem. Commun. (Cambridge, U.K.)* **2014,** *50* (52), 6850-6852. 10.1039/c4cc01345j.
169. Gianneschi, N. C.; Bertin, P. A.; Nguyen, S. T.; Mirkin, C. A.; Zakharov, L. N.; Rheingold, A. L. A Supramolecular Approach to an Allosteric Catalyst. *J. Am. Chem. Soc.* **2003,** *125* (35), 10508-10509. 10.1021/ja035621h.
170. Coleman, B. D.; d'Aquino, A. I.; Kean, Z.; Wang, Y.; Hedlund Orbeck, J. K.; Stern, C. L.; Mirkin, C. A. Structurally dynamic crystalline 1D coordination polymers enabled via the Weak-Link Approach. *Polyhedron* **2022,** *227*, 116116. 10.1016/j.poly.2022.116116.
171. Wiester, M. J.; Mirkin, C. A. Water-Soluble Macrocycles Synthesized via the Weak-Link Approach. *Inorg. Chem.* **2009,** *48* (17), 8054-8056. 10.1021/ic900983v.
172. Cheng, H. F.; Paul, M. K.; d'Aquino, A. I.; Stern, C. L.; Mirkin, C. A. Multi-State Dynamic Coordination Complexes Interconverted through Counterion-Controlled Phase Transfer. *Inorg. Chem.* **2021**. 10.1021/acs.inorgchem.0c03708.
173. Krevor, J. V. Z.; Simonis, U.; Richter, J. A. Structural analysis of platinum phosphine complexes by two-dimensional phosphorus-31 NMR spectroscopy. *Inorg. Chem.* **2002,** *31* (12), 2409-2414. 10.1021/ic00038a021.
174. Garrou, P. E. Δ_R-ring contributions to phosphorus-31 NMR parameters of transition-metal-phosphorus chelate complexes. *Chem. Rev.* **1981,** *81* (3), 229-266.
175. Still, B. M.; Kumar, P. G. A.; Aldrich-Wright, J. R.; Price, W. S. ^{195}Pt NMR—theory and application. *Chem. Soc. Rev.* **2007,** *36* (4), 665-686. 10.1039/b606190g.
176. d'Aquino, A. I.; Cheng, H. F.; Barroso-Flores, J.; Kean, Z. S.; Mendez-Arroyo, J.; McGuirk, C. M.; Mirkin, C. A. An Allosterically Regulated, Four-State Macrocycle. *Inorg. Chem.* **2018,** *57* (7), 3568-3578. 10.1021/acs.inorgchem.7b02745.
177. Kyba, E. P.; Clubb, C. N.; Larson, S. B.; Schueler, V. J.; Davis, R. E. Synthesis of 14-membered phosphorus-sulfur P_2S_2 and P_3S macrocycles which contain the 1-thio-2-(phenylphosphino)benzene moiety. Determination of stereochemistries of the free ligands and of a platinum(II) complex. *J. Am. Chem. Soc.* **1985,** *107* (7), 2141-2148. 10.1021/ja00293a052.
178. Kyba, E. P.; Davis, R. E.; Fox, M. A.; Clubb, C. N.; Liu, S. T.; Reitz, G. A.; Scheuler, V. J.; Kashyap, R. P. Phosphinomacrocycles. 16. Complexation of the nickel(II) triad with 14-membered macrocyclic $P_{4-n}S_n$ (n = 2, 1, 0) ligands. Study of the effects on coordination of the relative configuration at the phosphines and the number and placement of thioether sites. *Inorg. Chem.* **1987,** *26* (11), 1647-1658. 10.1021/ic00258a005.
179. Toto, S. D.; Olmstead, M. M.; Arbuckle, B. W.; Bharadwaj, P. K.; Musker, W. K. Synthesis, characterization, and reactivity of platinum(II) complexes of a mesocyclic

ligand, 5-phenyl-1-thia-5-phosphacyclooctane. *Inorg. Chem.* **1990,** *29* (4), 691-699. 10.1021/ic00329a026.

180. Liu, Y.; Kean, Z. S.; d'Aquino, A. I.; Manraj, Y. D.; Mendez-Arroyo, J.; Mirkin, C. A. Palladium(II) Weak-Link Approach Complexes Bearing Hemilabile N-Heterocyclic Carbene-Thioether Ligands. *Inorg. Chem.* **2017,** *56* (10), 5902-5910. 10.1021/acs.inorgchem.7b00543.

VITA

EDUCATION

Northwestern University – The Graduate School, Evanston, IL
PhD in Chemistry
July 2023
Marshall University, Huntington, WV
BS in Chemistry (Suma Cum Laude)

June 2016

- Outstanding Graduating Chemist 2016, ACS Outstanding Undergraduate Chemist 2016, DOW-MU STEM Research Fellow 2015-2016

RELEVANT EXPERIENCE

Northwestern University, Evanston, IL
Mirkin Lab, Supramolecular Synthesis Subgroup Leader
Jan. 2022 – present

- Supervised organic and organometallic supramolecular chemistry-based projects of 12 graduate students, undergraduates, and post-docs
- Worked with a team of scientists to write and submit two national grants
- Recruited and onboarded new lab members; directly mentored one undergraduate and one graduate student
- Led weekly scientific discussions and meetings
- Safety officer and point of contact for the synthetic laboratory

Mirkin Lab, Graduate Student Researcher
Aug. 2019 – present

- Designed the first examples of a crystalline coordination polymer featuring Weak-Link Approach-based transition metal compounds; designed, synthesized, and characterized a multitude of organic hemilabile ligands featuring various functional groups
- Published in peer-reviewed chemistry journals; presented and presided at a top national chemistry conference
- Gained extensive experience in organic and organometallic synthesis and characterization techniques including NMR Spectroscopy, IR spectroscopy, and mass spectroscopy
- Managed and maintained multiple instruments including an air-free solvent system, 3 anhydrous gloveboxes, and an automatic chromatography column

Harris Lab, Graduate Student Researcher
July 2017 – Aug. 2019

- Synthesized a series of 11 novel transition metal-based, metal-organic framework magnet materials
- Gained extensive experience in air-free and Schlenk chemistry techniques and material characterization including X-ray crystallography, Mössbauer spectroscopy, thermal gravimetric analysis, UV-Vis-NIR spectroscopy, Raman spectroscopy, and magnetometry
- Maintained multiple specialty instrumentation including a Superconducting Quantum Interference Device (SQUID), Mössbauer spectrometer, and UV-Vis-NIR spectrometer
- Experienced in flame sealing glass and quartz materials

Castellani Lab, Marshall University, Huntington, WV
Undergraduate Student Researcher
Aug. 2012 – June 2016

- Worked towards developing a generalizable synthetic strategy for the production of novel

metallocenophanes
- Presented research at 3 university symposiums and 2 posters sessions

PROFESSIONAL DEVELOPMENT

Northwestern Center for Leadership Fellowship in Leadership, **Northwestern University**, Evanston, IL
Leadership Fellow Team Lead
Jan. 2023 – present
- Managed a team of 5 Fellows, facilitating group discussions on the nature of effective leadership

Leadership Fellow
Jan. 2022 – March 2022
- Developed Strength-Based Leadership skills and focused on contemporary leadership theory

Leadership Coachee
Jan. 2022 – March 2022
- Gained leadership skills in collaborative teamwork strategies, effective communication, and conflict resolution

Teaching Assistant Training Program, Northwestern University , Evanston, IL
Workshop Facilitator
Sept. 2021
- Demonstrated active learning techniques for the classroom to new graduate teaching assistants

Publications

1) **Benjamin D. Coleman,** Chad A. Mirkin, et al. Structurally dynamic crystalline 1D coordination polymers enabled via the Weak-Link Approach. *Polyhedron* **2022**, *227*, 116116.

2) Sarah Hurst Petrosko, **Benjamin D. Coleman**, Chad A. Mirkin et al. Spherical Nucleic Acids: Integrating Nanotechnology Concepts into General Chemistry Curricula. *J. Chem. Educ.* **2021**, *98(10)*, 3090.